Nonlinear thermal electric analysis of platinum microheaters

Sigurður Ægir Jónsson

Faculty of Physical Sciences
University of Iceland
2009

NONLINEAR THERMAL ELECTRIC ANALYSIS OF PLATINUM MICROHEATERS

Sigurður Ægir Jónsson

60 ECTS thesis submitted in partial fulfillment of a
Magister Scientiarum degree in Physics

Advisor
Prof. Snorri Ingvarsson

Faculty Representative
Dr. Kristján Leósson

M.Sc. committee
Prof. Viðar Guðmundsson
Dr. Hendrik F. Hamann

Faculty of Physical Sciences
School of Engineering and Natural Sciences
University of Iceland
Reykjavik, October 2009

Nonlinear thermal electric analysis of platinum microheaters
Thermal electric analysis of microheaters
60 ECTS thesis submitted in partial fulfillment of a M.Sc. degree in Physics

Copyright © 2009 Sigurður Ægir Jónsson
All rights reserved

Faculty of Physical Sciences
School of Engineering and Natural Sciences
University of Iceland
VRII, Hjardarhagi 2-6
107, Reykjavik
Iceland

Telephone: 525 4000

Bibliographic information:
Sigurður Ægir Jónsson, 2009, Nonlinear thermal electric analysis of platinum microheaters, M.Sc. thesis, Faculty of Physical Sciences, University of Iceland.

ISBN 978-9979-70-639-7

Printing: Háskólaprent, Fálkagata 2, 107 Reykjavík
Reykjavik, Iceland, October 2009

Abstract

A thermal electric finite element method (FEM) analysis was used to investigate the thermal properties of individual electrically driven platinum microheaters. The results suggest that the temperature regulation mechanism used is reliable despite changes in the structural properties of the platinum due to electromigration and annealing effects. The temperature distribution was found to be very localized around the heaters, especially for heaters of width under 2 μm, in agreement with experiments. The results suggest that by using thicker oxide layer the radiation efficiency and the heater lifetime can be increased substantially. Time dependent analysis gave a response of the order of tens of nanoseconds for submicron wire width, suggesting they could be useful where infrared pulses at frequency lower than 10 MHz are needed. Alternative substrates are suggested and their effect on the thermal properties are investigated. A bi-directional current power regulation system able to run at 20 kHz was designed to decrease the effect of electromigration and extend the heater lifetime.

Útdráttur

Raf- og varmaeiginleikar stakra rafhitaðra örvíra úr platínu voru greindir með einingaraðferðinni. Niðurstöðurnar benda til þess að þrátt fyrir breytingar í efniseiginleikum vegna bökunar og rafflutnings þá sé aðferðin sem notuð er til hitastigsreglunar áreiðanleg. Varmadreifingin reynist vera mjög staðbundin umhverfis hitaranna, sérstaklega umhverfis hitara af breidd undir 2 μm, í samræmi við tilraunir. Sýnt var fram á að með því að nota þykkara oxíð-lag má auka nýtni og líftíma örhitarana verulega. Greining á tímaháðum eiginleikum þeirra sem fall af breidd leiddi í ljós viðbragðstíma í stærðarþrepinu tugir nanósekúndna. Þessi stutti viðbragðstími bendir til þess að hitararnir gætu hentað sem púlsaðir innrauðir ljósgjafar sem nýta má á tíðnum upp að $\sim$ 10 MHz. Lagðar eru fram tillögur um önnur undirlög og áhrif þeirra á varmaeiginleika hitaranna rannsakaðir. Nýr riðstraumsaflreglari sem getur keyrt á allt að 20 kHz var hannaður. Með því að nota riðstraum má minnka áhrif rafflutnings og þar með hugsanlega lengja líftíma hitaranna verulega.

Contents

List of Figures ix

List of Tables xiii

Acknowledgments xv

1 Introduction 1

2 Microheaters 3
- 2.1 Temperature regulation . . . 4
- 2.2 Fabrication . . . 6
  - 2.2.1 Lithography . . . 6
  - 2.2.2 Microheater fabrication . . . 9
- 2.3 Blackbody radiation . . . 11
- 2.4 Enhanced thermal emission . . . 14
- 2.5 Thermal radiation spectra . . . 18
- 2.6 Coherence properties . . . 24
- 2.7 Potential applications . . . 28
  - 2.7.1 Thermally excited near-field source . . . 28
  - 2.7.2 Phase-change storage . . . 30

3 FTIR spectrum measurements 33
- 3.1 Experimental setup . . . 33
- 3.2 Results . . . 35

4 Finite element analysis 39
- 4.1 The finite element method (FEM) . . . 39
- 4.2 PDE's of thermal electric coupling . . . 42
- 4.3 Structure and boundary conditions . . . 44
- 4.4 Material properties . . . 47
  - 4.4.1 Silicon . . . 47
  - 4.4.2 Silicon dioxide . . . 48
  - 4.4.3 Platinum . . . 49
- 4.5 Temperature-power relation . . . 51
- 4.6 Temperature distributions . . . 55
- 4.7 Effect of the metallic layer properties . . . 59

4.8 Effect of the silicon dioxide layer thickness 61
4.9 Thermal response time 66
4.10 Single layer cadmium selenide substrate 68

5 Power Regulator **73**

6 Summary and conclusion **77**

Bibliography **79**

List of Figures

2.1 Schematic of a typical metallic microheater 3

2.2 Heater of length $l = 6\ \mu$m and width $w = 250$ nm before and after break down due to electromigration and/or annealing effects 5

2.3 Photolithography using a negative resist and metal film deposition . . . 7

2.4 Blackbody spectra for different temperatures 12

2.5 Schematic of the IR microscope experimental setup 15

2.6 Thermal radiation intensity I as a function of polarization angle θ . . . 15

2.7 Extinction ratio E and radiation efficiencies R_{total} and R_{unpol} as a function of heater width w for fixed heater length $l = 6\ \mu$m 16

2.8 Angular thermal radiation pattern for microheaters of width $w = 300$ nm and $w = 500$ nm and fixed length $l = 6\ \mu$m 16

2.9 Schematics of the Fourier-transform infrared spectrometry setup 18

2.10 FTIR spectra obtained from heaters of $T = 750$ K for polarization directions parallel and perpendicular to the heater long axis 20

2.11 Integrated intensity as a function of heater width w 20

2.12 Reduced intensity ratio as a function of heater width w 22

2.13 Schematics of the coherence experimental setup 24

2.14 Interference fringes for a $w = 125$ nm heater at 300°C and 500°C and the fringe visibility as a function of the optical path difference 26

2.15 Interference fringes for heaters of different sizes at 500°C and comparison of the degree of coherence to the of blackbody radiation 27

2.16 Two conventional approaches to the near field-source and the thermally excited near-field source 29

2.17 Illustration of an all-thermal-phase-change storage concept 30

3.1 Schematic of the FTIR experimental setup 34

3.2 Microheater array with ten heaters if length $l = 50$ μm and width $w = 0.6$ μm 35

3.3 Thermal spectra from the heater array and the substrate for polarization directions both parallel and perpendicular the heaters 35

3.4 Transmittance through a 10 mm thick samples of silicon (Si), silicon dioxide (SiO_2), zinc selenide (ZnSe) and crystalline sodium chloride (NaCl) 37

3.5 The relation between the wavelength λ and the wavenumber $\tilde{\nu}$ 37

4.1 Discretization for an irregular boundary. 40

4.2 A simplified wire structure 44

4.3 An example of the meshing of a simple wire structure 46

4.4 Voltage V_h as a function of the current I_h for heaters of length $l = 8$ μm and width w from 200 nm to 8 μm 53

4.5 Temperature of the microheater center T as a function of power dissipated P_h for heaters of length $l = 8$ μm and varying width w from 200 nm to 8 μm 53

4.6 Inverse thermal impedance $1/Z_\mathrm{th}$ as a function of heater width w for heaters of fixed length $l = 8$ μm and width w from 200 nm to 8 μm. . . 54

4.7 Inverse thermal impedance $1/Z_\mathrm{th}$ as a function of heater length l for heaters of fixed width $w = 300$ nm and length l from 0.4 μm to 15 μm . 54

4.8 The temperature field of a heater of length $l = 8$ μm and width $w = 1$ μm 55

4.9 Temperature along the axis perpendicular to the long axis of heaters of fixed length $l = 8$ μm and varying width w held at fixed temperature . 56

4.10 Temperature through the center and into the substrate for heaters of fixed length $l = 8$ μm and varying width w held at fixed temperature . 58

4.11 Temperature along the long axis of heaters of fixed length $l = 8$ μm and varying width w held at fixed temperature $T = 700$ K. 58

4.12 Temperature of the microheater center T as a function of power dissipation P_h for normal platinum resistivity ϱ_Pt and increased by 50%, i.e. $1.5 \times \varrho_\mathrm{Pt}$ 59

4.13 Temperature of the microheater center T as a function of power dissipation P_h for normal platinum TCR α_Pt and increased by 50% $1.5 \times \alpha_\mathrm{Pt}$ 60

4.14 Temperature of the microheater center T as a function of power dissipation P_h for normal platinum thermal conductivity k_Pt and scaled by $\pm 50\%$ 60

4.15 The temperature of the microheater center T as a function of power dissipation P_h for varying silicon dioxide layer thickness d_O ($l = 8$ μm and $w = 8$ μm) 62

4.16 Inverse thermal impedance $1/Z_\mathrm{th}$ as a function of silicon dioxide thickness d_O 62

4.17 Current density j at temperature $T = 700$ K as a function of silicon dioxide thickness d_O 63

4.18 Temperature along the axis perpendicular to the long axis of heaters at $T = 700$ K on varying silicon dioxide thickness ($l = 8$ μm, $w = 1$ μm) . 65

4.19 Temperature through the center and into the substrate of heaters at $T = 700$ K on varying silicon dioxide thickness ($l = 8$ μm, $w = 1$ μm) . 65

4.20 Temperature along the long axis of heaters at $T = 700$ K on varying silicon dioxide thickness d_O ($l = 8$ μm, $w = 1$ μm) 66

4.21 Temperature in the heater center as a function of time t for heaters of fixed length $l = 8$ μm and varying width w 67

4.22 Thermal response times $\tau_{600\ \mathrm{K}}$, $\tau_{650\ \mathrm{K}}$ and $\tau_{690\ \mathrm{K}}$ as a function of heater width w for $T_\infty = 700$ K 67

4.23 Thermal conductivity k_{CdSe} of cadmium selenide as a function of temperature T 68

4.24 The temperature of the microheater center T as a function of power dissipation P_{h} for two silicon dioxide layer thicknesses and a cadmium selenide substrate 69

4.25 Temperature along the axis perpendicular to the long axis of heaters at $T = 700$ K for two silicon dioxide layer thicknesses and a cadmium selenide substrate 69

4.26 Temperature through the center and into the substrate of heaters at $T = 700$ K for two silicon dioxide layer thicknesses and a cadmium selenide substrate 70

4.27 Temperature along the long axis of heaters at $T = 700$ K for two silicon dioxide layer thicknesses and a cadmium selenide substrate 70

5.1 An electronic circuit that controls the voltage V_{h} applied over a microheater of resistance R_{h} while measuring the current I_{h} 74

List of Tables

2.1 Emissivity of some common metals (Newport 2009). 11

4.1 Bulk silicon properties. 48

4.2 Amorphous bulk silicon dioxide properties. 49

4.3 The dependence of the silicon dioxide normal-to-plane thermal conductivity $k_{\mathrm{O}\perp}$ on film thickness (Kato & Hatta 2005). 50

4.4 Platinum bulk properties. 50

4.5 Platinum electrical resistivity and thermal conductivity. 51

4.6 The position of the first interference peak $\tilde{\nu}_{\mathrm{if}}$ for few oxide thicknesses d_{O}. 63

Acknowledgments

First and foremost I would like to thank my supervisor Prof. Snorri Ingvarsson for intensive guidance and support throughout the time we have worked together. Many thanks also go to my fellow group members for inspiring discussions, especially to Yat-Yin Au for his everlasting patience answering questions and speculations.

I would like to thank Prof. Fjóla Jónsdóttir for her assistance with ANSYS, and both Kristján Jónsson and Guðjón I. Guðjónsson for their technical support in the course of this study. My sincere thanks also goes to all the other people who helped me during this time.

I owe my loving thanks to my beloved Líney Halla Kristinsdóttir, for her encouragement, understanding and enthusiastic proofreading of this thesis. I also wish to express my utmost gratitude to my family and my friends for their love and support.

I would like to acknowledge that this project was a part of a Joint Study Agreement with the group of Dr. Hendrik Hamann at IBM's T. J. Watson Research Center in Yorktown Heights, New York. Lastly, I want to acknowledge the financial support by the The Icelandic Centre for Research, and the Research Fund of the University of Iceland.

1 Introduction

Recently the use of nanostructures to control the spectral and directional properties of thermal radiation has attracted a lot of interest because of a number of interesting applications (Ingvarsson et al. 2007). Theoretically it has been predicted that propagation of surface waves produces long-range correlation between charge fluctuations at a material surface (Carminati & Greffet 1999). Patterning the surface appropriately can therefore be used to enhance the coherence of the thermal radiation. This has been observed in periodic structures of both dielectric (Greffet et al. 2002) and metallic materials (Laroche et al. 2005, Tsai et al. 2006).

Nanoscale optical antennas exploiting this effect have been fabricated to provide a local-field enhancement under irradiation of an external light source in the visible and infrared range (Alda et al. 2005, Cubukcu et al. 2006, Hamann et al. 2000). The main concern of our research group at the University of Iceland and our collaborators at IBM's T.J. Watson Research center in New York however is using resistive electric current heating of metallic microwires to produce a localized near-field in the infrared regime without the need for an external driving field. Generally we refer to these wires as microheaters.

This thesis is centered around the thermal electric properties of the heaters and ways to extend their lifetime and suppress the radiation from the substrate they are grown on. The contents in the following chapters is organized as follows:

In chapter 2 the main objective is to introduce the reader to the microheaters. Their typical structure and the temperature regulation mechanism will be presented. Their most critical breakdown mechanisms, electromigration and annealing effects will be introduced and the fabrication process discussed in details. A short general discussion about thermal radiation will be given, followed by a survey of our group's work where their most important optical properties, enhanced emission, infrared spectra and coherence properties will be discussed. The chapter ends with a short discussion about potential applications.

In chapter 3 an attempt the measure the heater spectra in the $600 - 1800$ cm^{-1} range is discussed. A strong emission from the silicon/silicon dioxide substrate was observed, which made it impossible to isolate the heater spectra. Finally, the drawbacks of heater arrays and ways to suppress the radiation contribution of the substrate by using other materials or suspended heaters are addressed.

The concern of chapter 4 will be a finite element analysis on single microheater structures. The temperature-power relation and the effect of changes in the heater resistivity and thermal conductivity will be investigated, to examine the validity of the assumptions used for the temperature regulation mechanism covered in chapter 2. The temperature distribution will be explored for different heater widths and oxide thicknesses, in order to tell if a substrate radiation is expected to be significant. The emission efficiency and expected lifetime of the microheaters will be investigated as a function of oxide thickness and different methods to increase both discussed. A time dependent analysis is used to study the thermal response time of the structure, and with respect to the results its potential as a pulsed high frequency IR light source addressed. Finally the thermal electric properties of heaters deposited on top of two promising new substrate materials, cadmium selenide (CdSe) and crystalline sodium chloride (NaCl) are investigated.

In chapter 5 a new power regulation system designed to elongate the lifetime of the heaters is discussed. The fact that the heating of the microheaters is independent of the current direction is exploited by using a bidirectional current stress at a frequency of few kHz. Using such a high frequency current has been shown to increase the lifetime of various interconnects substantially, and the same is expected for the microheaters although it has not been tested extensively.

2 Microheaters

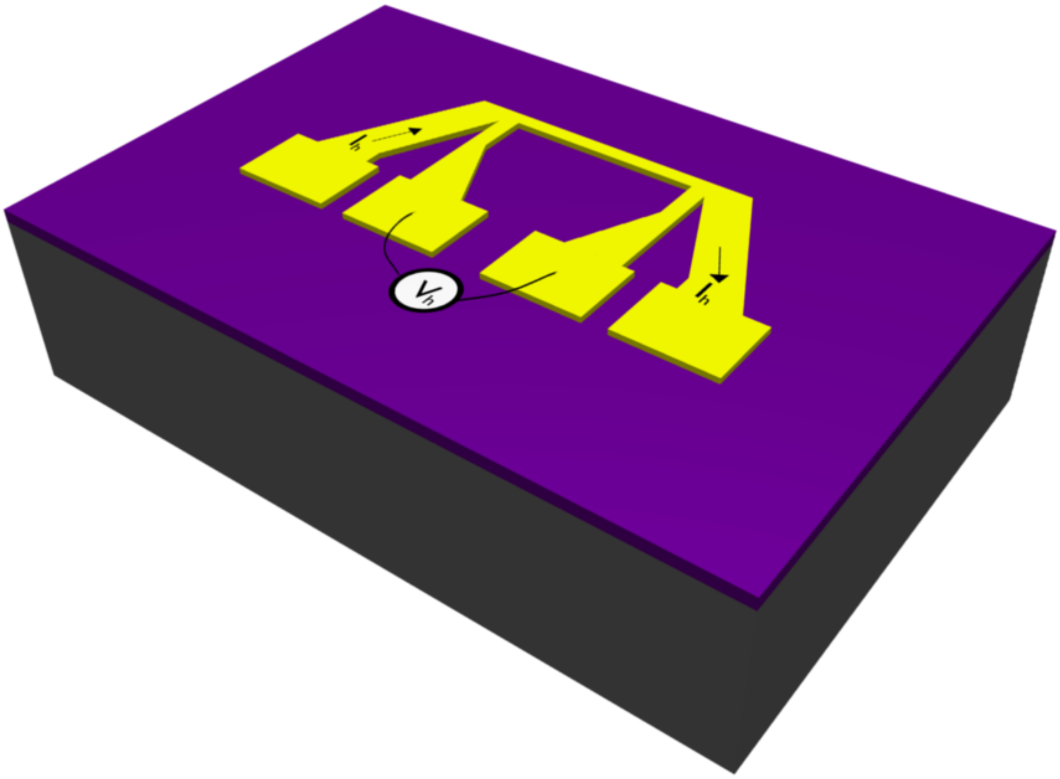

Figure 2.1: Schematic of a typical metallic microheater (yellow) grown on a silicon substrate (grey) with a thin electrically and thermally insulating SiO_2 layer (violet) on top.

What we refer to as a microheater is a thin film, rectangularly shaped metallic constriction of length l, width w and thickness d. The heaters are usually grown on top of a silicon substrate with a thin electrically and thermally insulating SiO_2 surface layer as shown in Figure 2.1. A four-wire configuration allows heating of the microheater by passing an electric current I_h through the two outer source wires while at the same time monitoring the voltage drop V_h over the heater through the two inner sensing wires, thus allowing us to maintain the power dissipation P_h in the heater at some desired value using

$$P_\mathrm{h} = V_\mathrm{h} \times I_\mathrm{h} \tag{2.1}$$

and a digital feedback loop while monitoring the heater resistance

$$R = V_\mathrm{h}/I_\mathrm{h} \tag{2.2}$$

continuously.

2.1 Temperature regulation

The resistance of metallic wires can be calculated by

$$R = \varrho \frac{l}{A} \tag{2.3}$$

where ϱ is the resistivity of the metal, l the length of the wire and A the cross-section area ($A = w \times d$). The resistivity has been shown to increase linearly with temperature T according to

$$\varrho = \varrho_0 (1 + \alpha \Delta T) \tag{2.4}$$

and hence we can write

$$R = R_0 (1 + \alpha \Delta T) \tag{2.5}$$

where R_0 (ϱ_0) is the resistance (resistivity) at room temperature T_0, α is the *thermal coefficient of resistance* (TCR) and $\Delta T = T - T_0$ (Young & Freedman 2007). If we further assume that ΔT is linearly related to the power dissipation we can define the *thermal impedance* τ as

$$\tau \equiv \frac{dT}{dP} = \frac{\Delta T}{\Delta P} = \frac{T - T_0}{P - P_0} = \frac{T - T_0}{P} \tag{2.6}$$

where we have assumed no power dissipation $P_0 = 0$ mW at room temperature T_0. By plugging Equation 2.6 into Equation 2.5 one obtains

$$R = R_0 (1 + \alpha \tau P) = R_0 + R_0 \alpha \tau P \, . \tag{2.7}$$

Hence by measuring the resistance R as a function of applied power P and fitting it with a linear function of the form

$$R = C_0 + C_1 P \tag{2.8}$$

one can get the thermal impedance τ from the fitting parameters

$$\tau = \frac{C_1}{C_0 \alpha} \tag{2.9}$$

From Equation 2.6 we then achieve the power-temperature relation

$$P = \frac{T - T_0}{\tau} \, . \tag{2.10}$$

To obtain the necessary data we

1. Measure the I_h-V_h characteristics of the heater.
2. Fit $V_\mathrm{h}(I_\mathrm{h})$ linearly in the low current section and extract R_0 from the slope.
3. Calculate dissipated power and heater resistance using Equation 2.1 and Equation 2.2 respectively for all the data points.
4. Plot R versus P, verify *linearity* and fit with Equation 2.8 to extract τ from the fit coefficients, using Equation 2.9.
5. Extrapolate to the necessary power for the desired temperature using Equation 2.10

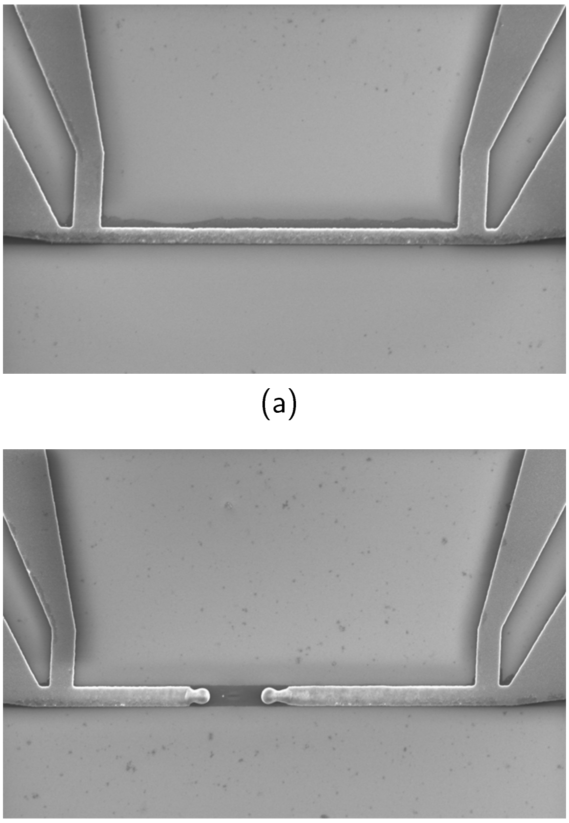

Figure 2.2: Heater of length $l = 6$ μm and width $w = 250$ nm (a) before and (b) after break down due to electromigration and/or annealing effects.

When the metallic heaters are heated up electrically their resistivity will be influenced by both *annealing effects* and *electromigration*. Annealing occurs by the diffusion of atoms so that the material progresses towards equilibrium. The high temperature increases the rate of diffusion by providing the energy needed to break bonds. The movement of atoms affects the grain size, grain distribution and density of dislocations in metals, hence altering their resistivity (Wikipedia 2009*a*, *Annealing*). Electromigration is caused by the gradual movements of the ions in a conductor due to the momentum transfer between conducting electrons and diffusing metal atoms, resulting in material transport (Wikipedia 2009*b*, *Electromigration*). As the structure size in electronics decreases, the practical significance of this effect increases due to higher current density. The typical current density at which electromigration occurs in metal interconnects is $10^5 - 10^7$ A/cm^2 (Ho & Kwok 1989).

An independent experimental study has shown that although the resistance-temperature relationship of these metallic heaters can be influenced at high temperatures and high currents, the relationship between applied power and temperature rise in the heater remains unaltered (Ingvarsson et al. 2007). Therefore by keeping the applied power constant, we are able to maintain the temperature of the heater quite accurately at a desired value (estimated to be within ±2%).

2.2 Fabrication

The microheaters have been fabricated both in the nanocenter at the University of Iceland and by our collaborators at IBM. In this section the microheater fabrication process at the University of Iceland will be illustrated, but it should be almost analogous to the process used by our collaborators at IBM.

2.2.1 Lithography

Lithography in general is a process used in micro-fabrication to selectively remove parts of a thin film or the bulk of a substrate. The technique has been primarily developed by the semiconductor industry. It uses light (*photolithography*) or a particle beam (e.g. electrons in *e-beam lithography*) to transfer a geometric pattern to a *resist* (a light- or a particle-sensitive polymer) on the sample's surface. An example of the lithography process is explained in steps in Figure 2.3. Further explanations and comments to each panel follow:

a. Keeping the sample clean is of central importance since the small structures can be easily contaminated by even small dust particles. If organic or inorganic contaminations are present on the wafer surface, they are usually removed by wet chemical treatments using organic acids such as TCE (trichloroethylene), followed by acetone and methanol. The cleaning process is carried out in a cleanroom to avoid dust particles.

b. When the sample surface is clean the resist can be applied. When choosing the

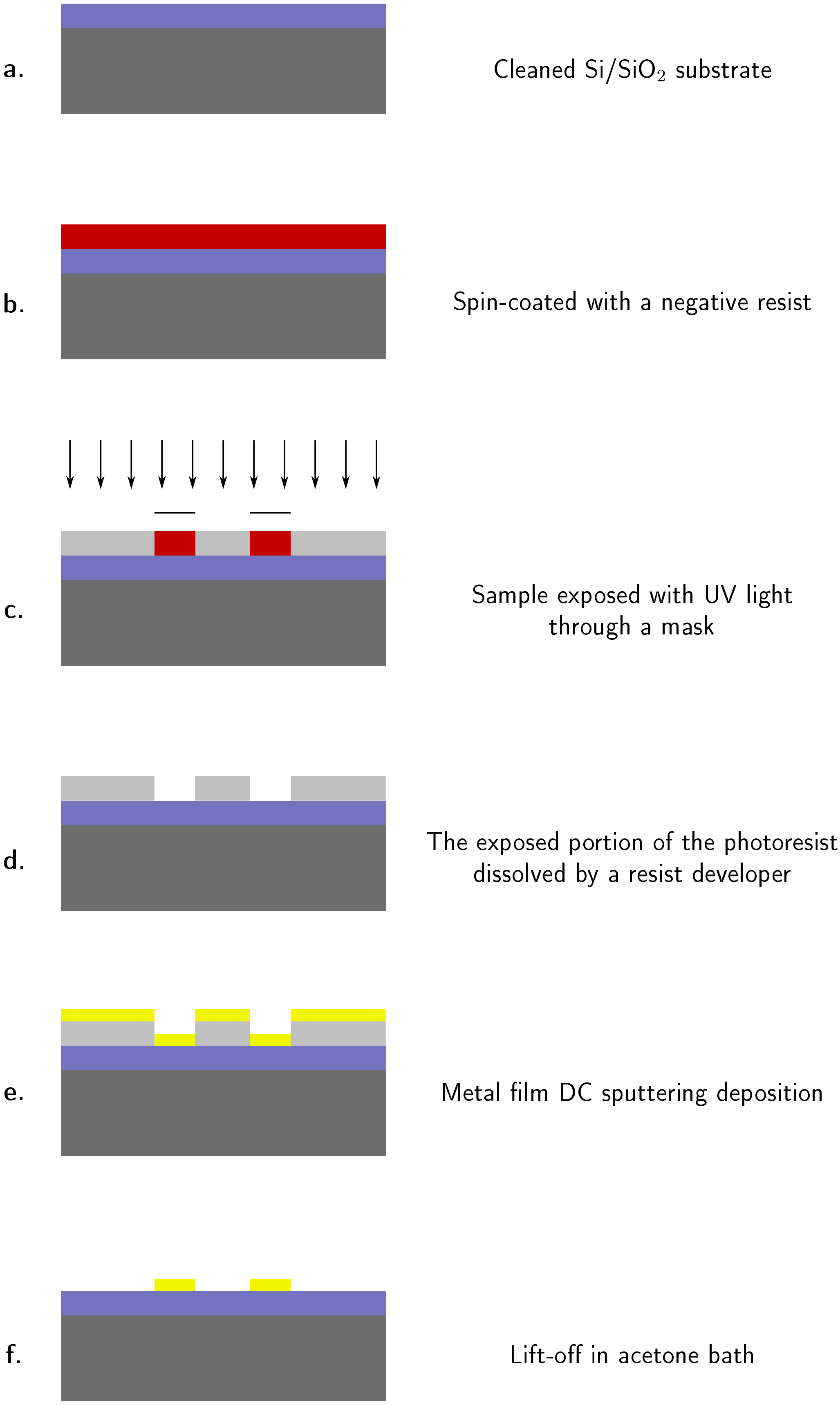
a.
Cleaned Si/SiO$_2$ substrate
b.
Spin-coated with a negative resist
c.
Sample exposed with UV light through a mask
d.
The exposed portion of the photoresist dissolved by a resist developer
e.
Metal film DC sputtering deposition
f.
Lift-off in acetone bath

Figure 2.3: Photolithography using a negative resist and metal film deposition. Further explanations in text.

resist type the desired resolution, the printing type (i.e. UV, e-beam, X-ray) and the characteristics of etching and deposition have to be considered. Resists are classified into two groups: *positive resists* and *negative resists* (Wikipedia 2009*f*, *Photoresist*):

- A positive resist is a type of resist in which the portion of the resist that is exposed becomes soluble to the *resist developer*. The portion of the resist that is unexposed remains insoluble to the resist developer.

- A negative resist is a type of resist in which the portion of the resist that is exposed becomes relatively insoluble to the resist developer. The unexposed portion of the resist is dissolved by the resist developer.

To uniformly coat the resist on the substrate, the substrate is usually spun by a spinner at a few thousand RPM for some seconds after pouring the resist over it. The sample is also occasionally pre- and postbaked in an oven or on a hot plate.

Unfortunately, the surface of many of the materials we want to put resist on oxidize very easily. The surface oxide forms long range hydrogen bonds with water adsorbed from the air. When the resist is spun onto such a surface, it adheres to the water vapor rather than to the surface, and poor adhesion results. To suppress this effect an HDMS (Hexamethyldisilazane) primer, which serves as an adhesion promoter for the photoresist, can be used. It can either be spun onto the wafer in a process called *Liquid priming* or by depositing a thin layer by maintaining the wafer in an HDMS vapor in a process called *Vapor priming.*

c. Two methods are primarily used to write the pattern on the resist.

- Using an opaque plate with holes or transparencies that allow light to shine through in a defined pattern. This technique is the most commonly used in photolithography, where the sample is exposed with UV light in an mask aligner, through a *photomask*. This is shown in Figure 2.3

- Scanning a beam of particles in a patterned fashion across the surface. In e-beam lithography this is the most commonly used technique (Wikipedia 2009*f*, *Electron beam lithography*).

d. A *resist developer* is used to remove the exposed (non-exposed) portion of the positive (negative) resist. Some resists should be baked after exposure, for hardening before etching.

e. Now the sample is ready for etching, deposition or other processes:

- *Etching*: A liquid or plasma chemical agent removes the uppermost layer of the substrate in the areas that are not protected by resist.

- *Deposition*: A material layer is deposed over the sample surface, usually by some vapor deposition method (e.g. physical vapor deposition)

f. The remainder of the resist is removed together with the material covering it with a solvent (e.g. acetone), and only the material that was deposited through openings in the pattern and in direct contact with the underlying layer stays. This process is referred to as "*lift-off*".

This process can be repeated numerous times to create complex integrated circuits. In a modern CMOS fabrication process the wafer will go through the photolithographic cycle up to 50 times (Wikipedia 2009*e*, *Photolithography*).

Due to the *diffraction limit* the resolution in photolithography is limited by the wavelength of the light. Hence exposure with UV light gives a resolution in the μm range. In electron beam (e-beam) lithography however the resolution limit does not come from the diffraction, but rather from other factors such as aberrations in the electron optics, mechanical vibrations, diffusive scattering of electrons and finite polymer size in the resist. For most resists it has turned out to be difficult to go below a limit of 20 nm resolution (Wikipedia 2009*c*). The most severe limitations of e-beam lithography are low throughput and high cost.

2.2.2 Microheater fabrication

The microheater fabrication takes two lithographic cycles:

1. First photolithography is used to grow several identical contact pads on top of a Si/SiO_2 wafer.
    a) The Si/SiO_2 substrate is cleaned in an ultrasound acetone bath for 2-3 minutes and then rinsed by methanol and isopropanol. This step might be unnecessary when a new wafer is being used.
    b) The sample is prebaked at 140°C for 5 minutes.
    c) An HDMS vapor priming is used for 12 minutes.
    d) A negative photoresist ma-N 1410 (micro resist technology) is spin-coated over the substrate at 4000 RPM for 30 seconds.
    e) The sample is postbaked at 100°C for 1.5 minute.

   f) The sample is exposed to UV light in an aligner, through a photomask for 6.2 seconds at 22.0 mW × cm^{-2} intensity.

   g) The resist is developed for 45 seconds by using ma-D 533/S (micro resist technology) developer.

   h) The sample is rinsed using purified water and then blown dry using N_2.

   i) Cleaned for 30 s in gentle Ar/O_2 plasma.

   j) Sample mounted on a sample holder in the sputtering chamber and the chamber evacuated down to 1×10^{-7} mbar

   k) A 5 nm thick Cr adhesion layer and 100 nm thick Cu layer are deposited at rates of 0.5 Å/s and 1.2 Å/s, respectively.

   l) The sample is immersed in acetone bath for approx. 30 minutes for lift-off. Then it is rinsed in methanol and blown dry using N_2 gas.

   m) The metallic pattern checked under a microscope.

2. The microheaters are patterned individually between the contact pads using e-beam lithography.

   a) The sample is prebaked at 170°C for 5 minutes.

   b) A positive PMMA (4% poly-methyl methacrylate in anisole) resist (micro resist technology) is spin-coated over the substrate at 4000 RPM for 30 seconds.

   c) The sample is postbaked at 170°C for 5 minutes.

   d) The pattern is transferred to the resist using e-beam writing. Each heater is rastered (pixel by pixel) onto the wafer individually using a focused electron beam.

   e) The pattern is developed for 30 seconds using MIBK (methyl isobutyl ketone):IPA (isopropanol)=1:3 developer.

   f) Rinsed by isopropanol (stops development) for 30 seconds and blown dry using N_2 and checked under microscope.

   g) Sample mounted on a sample holder in the sputtering chamber and the chamber evacuated down to 1×10^{-7} mbar

h) A 5 nm thick Cr adhesion layer and 50 nm thick Pt layer are deposited at rates of 0.5 Å/s and 1.0 Å/s, respectively.

i) The sample is immersed in acetone bath for approx. 30 minutes for lift-off. Then rinsed in methanol and blown dry using N_2 gas.

j) The metallic pattern checked under a microscope.

Table 2.1: Emissivity of some common metals (Newport 2009).

Material	Temperature [°C]	Emissivity ϵ
Platinum	538	0.10
Silver	538	0.03
Gold	538	0.03
Copper	538	0.05

The 5 nm Cr adhesion layer is to prevent peeling of the Cu and Pt layers from the silicon dioxide layer. Cu is used for the contacts because of high electric conductivity σ, ease of contact and low cost. Pt was chosen for the microheaters due to its resistance to corrosion and oxidation and high emissivity ϵ, as seen in comparison to some other *metals* in Table 2.1. Microheaters of gold (Au) and of a nickel-chrome alloy have also been fabricated.

2.3 Blackbody radiation

Blackbody radiation emitted by a heated object is generally considered incoherent and unpolarized with a spectrum described by Planck's law (Hecht 1998). Planck's law describes the emitted power per unit area of emitting surface, per unit solid angle, per unit frequency and is written in the *frequency form* as

$$I_p(\nu, T) = \frac{2h}{c^2} \frac{\nu^3}{e^{h\nu/k_B T} - 1} \tag{2.11}$$

where h is the Planck's constant, c is the speed of light, ν the radiation frequency and k_B the Boltzmann constant (Rybicki & Lightman 1979).

Each surface element on a *Lambertian surface* radiates with the same intensity regardless of the angle from which it is viewed. *Lambert's cosine law* states that the radiant intensity observed from a Lambertian surface is directly proportional to the cosine of the angle θ between the observer's line of sight and the surface normal (Hecht 1998, Wikipedia 2009*d*), which corresponds to the size of the observed area. By integrating $I_p(\nu, T)$ over all frequencies and over the half-sphere into which a flat surface element

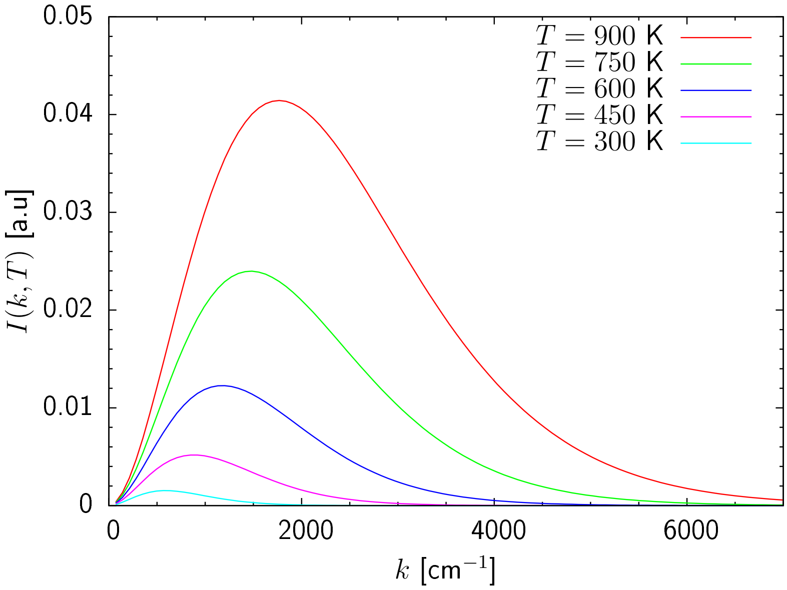

Figure 2.4: Blackbody spectra for different temperatures.

S emits according to Lambert's cosine law one obtains

$$P = \int_S d\Omega \int_0^\infty d\nu A I_p(\nu, T) cos(\theta) = A \frac{2\pi h}{c^2} \left(\frac{k_B T}{h} \right)^4 \frac{\pi^4}{15} . \tag{2.12}$$

The result is called the *Stefan–Boltzmann law* and is usually written as

$$H \equiv \frac{P}{A} = \frac{2\pi^5 k_B^4}{15 c^2 h^3} T^4 = \sigma_{SB} T^4 \tag{2.13}$$

where $H = P/A$ is the power per unit area and

$$\sigma_{SB} = \frac{2\pi^5 k_B^4}{15 c^2 h^3} \approx 5.670 \times 10^{-8} \text{ J s}^{-1}\text{m}^{-2}\text{K}^{-4} \tag{2.14}$$

is the *Stefan–Boltzmann constant* (Rybicki & Lightman 1979). Real objects are not perfect blackbodies. Nonetheless, most objects resemble a blackbody at certain temperatures and wavelengths (Hecht 1998). Hence it is useful to write similar expression for real objects

$$H = \epsilon \sigma_{SB} T^4 \tag{2.15}$$

where ϵ is called the *total emissivity*. For all materials $0 < \epsilon \leq 1$ and equals unity only for ideal blackbodies (Hecht 1998). Using the definition of a *wavenumber*

$$\tilde{\nu} = \frac{\nu}{c} = \frac{1}{\lambda} \tag{2.16}$$

one can as well write Planck's law, Equation 2.11, in *wavenumber form* $I_p(\tilde{\nu}, T)$ using that

$$I_p(\nu, T) d\nu = I_p(\tilde{\nu}, T) d\tilde{\nu} . \tag{2.17}$$

From Equation 2.16 we get

$$d\tilde{\nu} = \frac{d\nu}{c} \tag{2.18}$$

and from Equations 2.11, 2.16, 2.17 and 2.18 one obtains

$$I(\tilde{\nu}, T) = 2hc^2 \frac{\tilde{\nu}^3}{e^{hck/k_B T} - 1} \, . \tag{2.19}$$

The wavenumber form of Planck's law is plotted in Figure 2.4 for a few realistic temperatures for microheaters.

In the same way using that

$$\nu = c/\lambda \qquad \Rightarrow \qquad d\nu = -c/\lambda^2 d\lambda \tag{2.20}$$

and that

$$|I_p(\nu, T) d\nu| = |I_p(\lambda, T) d\lambda| \tag{2.21}$$

the *wavelength form* of Planck's law is obtained

$$I(\lambda, T) = \frac{2hc^2}{\lambda^5} \frac{1}{e^{hc/\lambda k_B T} - 1} \, . \tag{2.22}$$

By finding the maximum of Equation 2.11 by solving

$$\frac{\delta I_p(\nu, T)}{\delta \nu} = 0 \tag{2.23}$$

for ν_{max} one obtains the *frequency form of Wien's displacement law*

$$\nu_{\mathrm{max}} = \frac{\alpha}{h} k_{\mathrm{B}} T \tag{2.24}$$

where $\alpha = 2.821439$ is a constant resulting from numerical calculations. Wien's displacement law says that as the temperature is raised, the bulk of the radiation shifts to shorter wavelengths and higher frequencies (or wavenumbers). Due to the linear relationship between ν and $\tilde{\nu}$ from Equation 2.16 the maximum of Equation 2.19 is at

$$\tilde{\nu}_{\mathrm{max}} = \frac{\nu_{\mathrm{max}}}{c} = \frac{\alpha}{ch} k_{\mathrm{B}} T \, . \tag{2.25}$$

By finding the maximum of Equation 2.22, λ_{max}, one obtains the *wavelength form of Wien's displacement law*

$$\lambda_{\mathrm{max}} = \frac{hc}{k_{\mathrm{B}} \beta} \frac{1}{T} = \frac{b}{T} \tag{2.26}$$

where $\beta = 4.965114$ is a constant resulting from numerical calculations. $b = 2.8977685 \times 10^{-3}$ m×K is called *Wien's displacement constant.*

Note that the frequency and wavenumber solutions differ only by a constant, but the wavelength solution has different form, that is

$$\tilde{\nu}_{\mathrm{max}} = \frac{\nu_{\mathrm{max}}}{c} \neq \frac{1}{\lambda_{\mathrm{max}}} \tag{2.27}$$

since the relationship between ν and λ from Equation 2.20 is not linear as the relation between ν and $\tilde{\nu}$.

2.4 Enhanced thermal emission

In this section a fundamental experiment on microheaters will be illustrated along with its results. The experiment was the first research on the optical properties of such heaters done by our research group and our collaborators at IBM. The thermal emission was observed to show a high polarization and dipole-like angular radiation pattern. A simple analysis of the radiation intensities suggested a significant enhancement of the thermal radiation for very narrow heater structures. All figures in this section are from Ingvarsson et al. (2007) and are used with the author's permission. For a more detailed discussion, see Ingvarsson et al. (2007).

Platinum microheaters of fixed length $l = 6$ μm and thickness $d = 40$ nm, but varying width w from 125 nm to 4 μm were fabricated as described in subsection 2.2.2. Using the process explained in section 2.1 and the independently measured thermal coefficient of resistance for platinum $\alpha_{\mathrm{Pt}} = 0.002$ K^{-1} the thermal impedance τ was determined and used to find the $T(P)$ relation.

As the heater warms up it starts to radiate according to its temperature, and the optical signal is measured using the setup shown in Figure 2.5. The thermal emission is picked up with a high numerical aperture IR lens (NA = 0.7), analyzed by a linear rotatable polarizer and observed using liquid N_2 cooled InSb detector array. The InSb camera detector is sensitive in the $1-5$ μm spectral region but has a shortpass filter at 4.1 μm wavelength. During the experiment the temperatures of the microheaters were between 80°C and 800°C, which corresponds to emission peaks at wavelengths between $\lambda_{80^\circ\mathrm{C}} = 8.2$ μm and $\lambda_{800^\circ\mathrm{C}} = 2.7$ μm respectively for blackbodies, as predicted by Wien's displacement law in Equation 2.26. A simplified model of the spectral response of the system taking into account the responsivity of the InSb detector, the temperature dependent Planck function and the finite width wavelength window predicted that the measured intensity should scale with temperature as $I \propto T^{3.74}$.

In the experiment the radiation intensity signal I was recorded as a function of the angle of the wire grid polarizer θ, as shown in Figure 2.5. This was done both with and without the microheater turned on. The signal obtained when the heater was turned off was subtracted from the one obtained when the heater was turned on, in order to eliminate a residual background part of the signal. In Figure 2.6 typical thermal emission intensity data of a microheater are shown as a function of the linear polarizer angle θ. Both curves in the figure show $I(\theta)$ obtained from the same heater. The red curve shows $I(\theta)$ when the heater was rotated 90° with respect to its original position when the blue curve was obtained. We see that the polarization pattern shifts accordingly. This was done to make sure that the observes signal was real, not an artifact due to the setup. The same experiment using a thin platinum film was also performed and no polarization was observed.

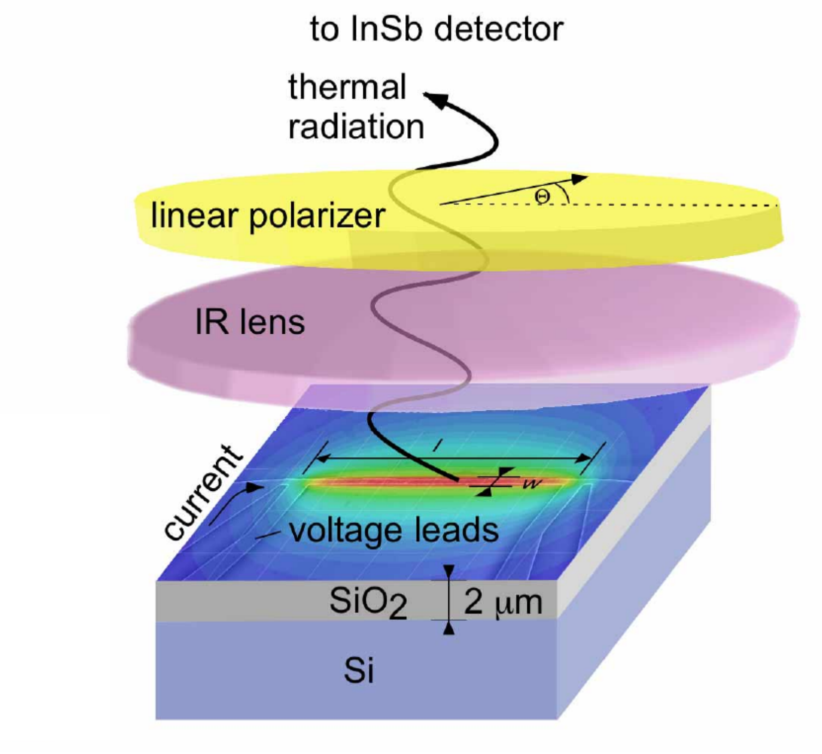
to InSb detector
thermal radiation
linear polarizer
Θ
IR lens
current
l
w
voltage leads
SiO2
2 μm
Si

Figure 2.5: Schematic of the IR microscope experimental setup (Ingvarsson et al. 2007).

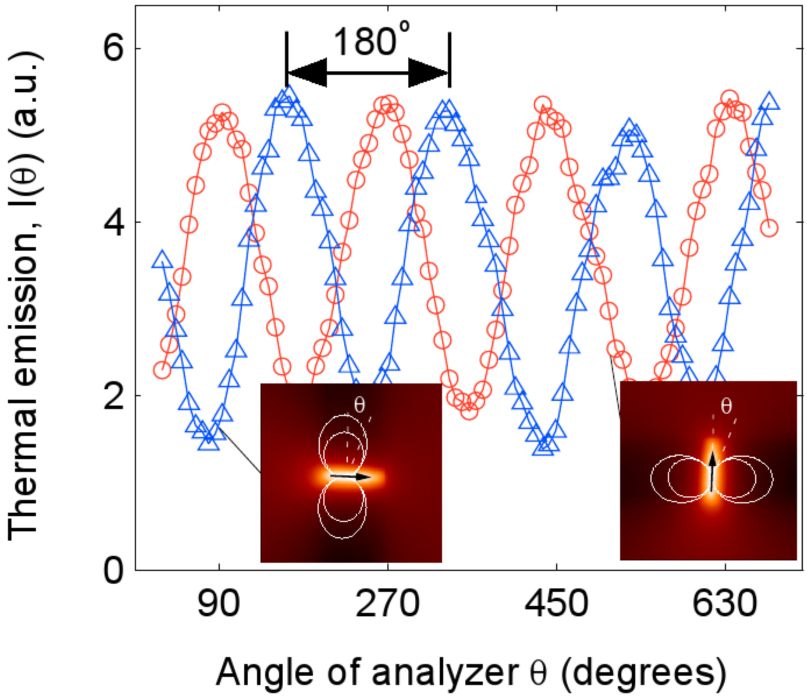

Figure 2.6: The thermal radiation intensity I as a function of the polarization angle θ. If the heater is rotated by 90° the thermal emission intensity signal is shifted accordingly (Ingvarsson et al. 2007).

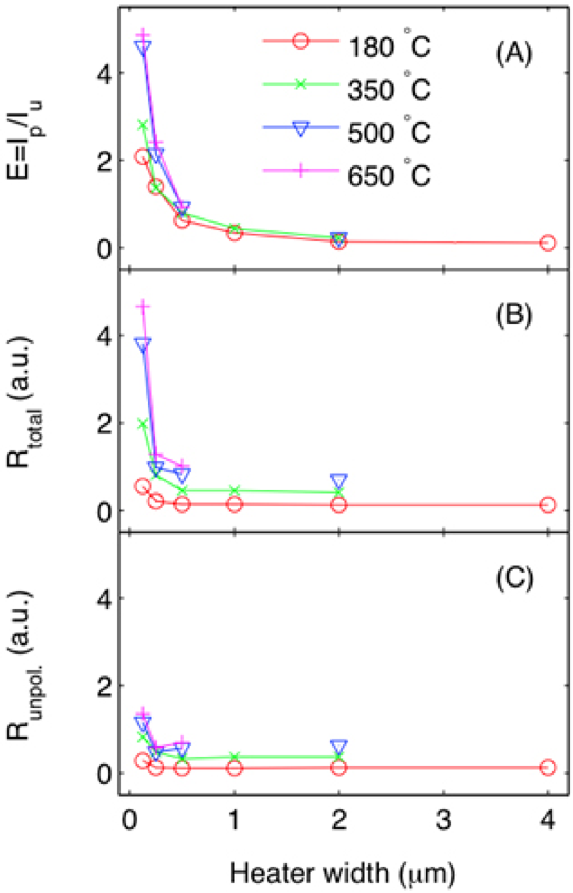

Figure 2.7: Extinction ratio E, total radiation efficiency R_{total} and unpolarized radiation efficiency R_{unpolar} as a function of heater width w for fixed heater length $l = 6$ μm (Ingvarsson et al. 2007).

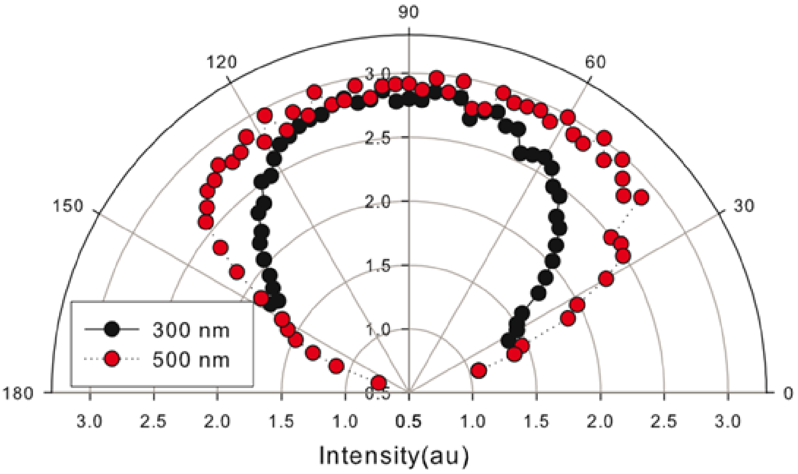

Figure 2.8: Angular thermal radiation patterns for two microheaters of different widths. The axis of rotation lies in the plane of the substrate and perpendicular to the heaters long axis. (Ingvarsson et al. 2007).

For analysis the polarization curves are fitted with the function

$$I(\theta) = I_\mathrm{p} \cos^2(\theta) + I_\mathrm{u} \tag{2.28}$$

where I_p and I_u are the polarized and unpolarized light intensity amplitudes respectively. The *extinction ratio* is then defined as

$$E = \frac{I_\mathrm{p}}{I_\mathrm{u}} \tag{2.29}$$

To quantify the polarized and unpolarized parts of the radiation for different geometries the *radiation efficiencies* are defined for both the total radiation

$$R_\mathrm{total} = \frac{\int_0^{2\pi} I(\theta) d\theta}{AT^{3.34}} \tag{2.30}$$

and the unpolarized part

$$R_\mathrm{unpol} = \frac{2\pi I_\mathrm{u}}{AT^{3.34}} \tag{2.31}$$

In both cases the intensity is normalized with respect to the microheaters surface area A $(w \times l)$ and the average temperature dependence of the heaters $T^{3.34}$.

Figure 2.7A shows the extinction ratio E as a function of heater width for various heater temperatures. It shows that as the width of the heater is narrowed, a strong increase in the extinction ratio is observed. This implies that the thermally-driven charge fluctuations are getting more confined. An almost constant total radiation efficiency R_total is observed for the wider heaters, as predicted by the Stefan–Boltzmann law Equation 2.15. However a large enhancement in R_total is found for narrow heaters. For comparison the unpolarized radiation efficiency R_unpol in Figure 2.7C changes much less with heater width. The relatively small dependence of R_unpol on heater width indicates that the actual hotspot dimensions scale directly with the heater size.

In this experiment it is unclear how much of the radiation enhancement in Figure 2.7B actually originates from the geometrical confinement, but not from things like surface roughnesses, interference effects with reflections from the Si/SiO$_2$ interface or by other means. Fluctuating electric fields are induced as predicted by fluctuation-dissipation theory (Rytov et al. 1987), giving random currents in every volume of the heater which can be thought of as a dipolar antenna that emits radiation. In bulk material the phase relation between these dipoles is random, but as the structure becomes smaller than the wavelength, an increased correlation is expected due to close proximity and geometrical alignment of the emitting dipoles.

Further support to this interpretation was observed when the angular radiation pattern from two different microwires of widths of w = 300 nm and w = 500 nm maintained at 500°C was measured. The sample was rotated in 2.5° steps around the axis in the plane of the substrate and perpendicular to the heater's long axis while measuring the emission intensity using liquid N_2 cooled InSb detector and a lens of NA $= 0.28$ (for higher angular resolution) as a function of the angle of rotation ϕ. In Figure 2.8 radiation pattern for the narrower wire $w = 300$ nm resembles almost perfectly the radiation pattern from a dipole, while the wider wire $w = 500$ nm deviates a little.

The antenna-like polarization pattern suggests a high degree of spatial and temporal coherence of charge fluctuations within the heaters. The strong resemblance between the (far-field) radiation patterns for narrow wires and of dipoles could suggests a dipole-like near-field as well. A dipole gives relatively strong near-fields which suggests that a strong near-field could be produced using thermally heated microwires (Jackson 1998).

2.5 Thermal radiation spectra

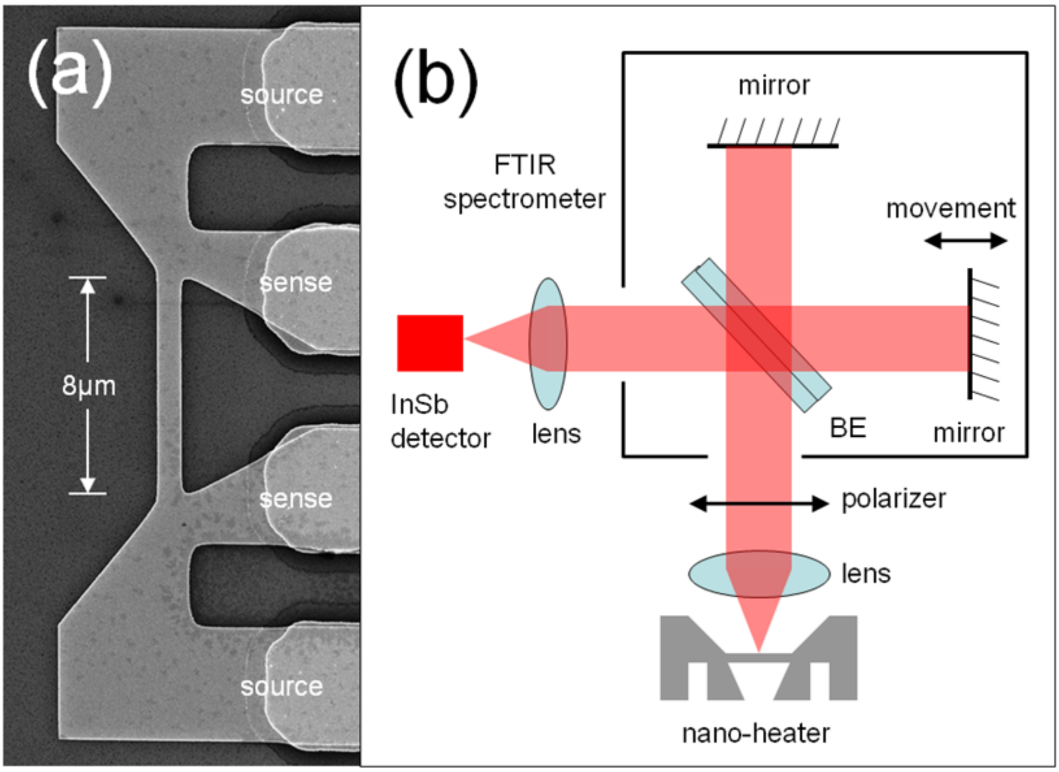

Figure 2.9: (a) Scanning electromicroscope image of an $8 \times 0.8\ \mu m^2$ heater. (b) Schematics for the experimental setup, where the radiation emitted by the microheater is analyzed with the FTIR system. (Yat-Yin Au et al. 2008).

In this section we will discuss the results from Yat-Yin Au et al. (2008). Infrared radiation from individual platinum microwires was measured using Fourier-transform infrared spectrometry. The spectra were measured as a function of heater width for polarization directions parallel and perpendicular the the heater's long axis. It was observed that when the heater width approaches zero the signal with polarization parallel to the heater converges to a finite value, while the perpendicular polarized part drops below the detection limit. As a result this leads to strongly polarized radiation for very narrow wires in accordance with the results from Ingvarsson et al. (2007) discussed in section 2.4. A $\lambda/2$ plasmon resonance was observed, attributed to charge oscillation correlations across the heater's width. All figures in this section are from Yat-Yin Au et al. (2008) and are used with the author's permission.

Platinum microheaters of fixed length $l = 8$ μm and thickness $d = 50$ nm, but varying width w from 200 nm to 8 μm were fabricated as described in section 2.2. The experimental setup is illustrated in Figure 2.9. A single heater is brought into focus with a reflective objective of NA $= 0.5$ and focal length $f = 5.41$ mm. The infrared light is analyzed using a rotatable wire-grid polarizer before entering a *Fourier-transform infrared (FTIR) spectrometer* (for more details see chapter 3). The resulting optical signal is then focused onto a liquid N_2 cooled InSb detector using a collective ZnSe lens. Performing a fast Fourier transform on this signal then gives the emission spectra from the radiating samples.

The heater was maintained at $T = 750$ K and the resulting thermal emission spectra measured as a function of heater width for polarization directions parallel and perpendicular to the heater's long axis. In Figure 2.10 the spectral data obtained as a function of the heater width for (a) the parallel and (b) perpendicular polarizations is shown after correction with respect to the FTIR system and the related optics. The parallel and perpendicular spectra from each heater have been normalized with the same number, chosen such that the parallel intensity peaks for all heater widths had equal height. This is done purely for visualization purposes. At 750 K thermal blackbody radiation peaks at an energy below the detector cut-off ($\sim$ 1800 cm^{-1}) as seen in Figure 2.4. Hence only the high energy tail of the spectrum is inside the detection window. For an ideal blackbody the Planck spectrum depends only on the temperature and is independent of the geometry of the source (with amplitude depending on surface area). In Figure 2.10a the shape of the spectra is mostly unchanged. On the other hand a substantial modification of the perpendicular spectra is observed, as shown in Figure 2.10b. At heaters widths $w \geq 2$ μm the spectra for the two polarization directions are almost identical. However as the heater width w is decreased below 1.0 μm the peak of the perpendicular spectrum is shifted into the detection range to roughly 2500 cm^{-1}. As the heater width decreases the peak shift is accompanied by an overall decrease in the intensity until it falls below the sensitivity limit once the heater width w reaches ~ 0.2 μm.

By integrating the spectra from 2000 cm^{-1} to 3500 cm^{-1}

$$I = \int_{2000\ \mathrm{cm}^{-1}}^{3500\ \mathrm{cm}^{-1}} I_{\mathrm{FTIR}} d\tilde{\nu} \tag{2.32}$$

for both polarization directions and plotting the result as a function of heater width

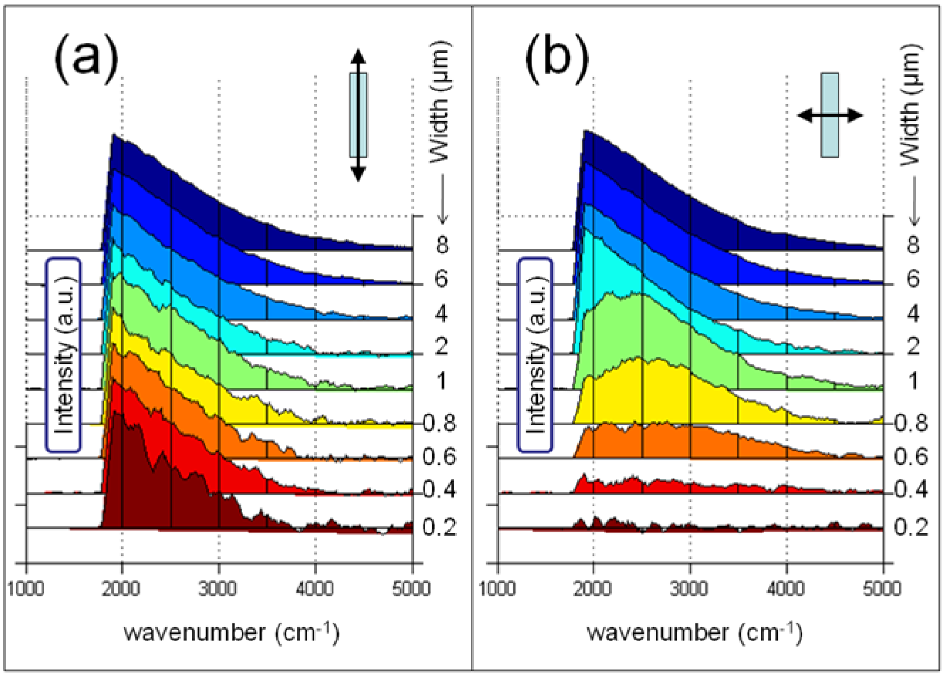

Figure 2.10: FTIR spectra obtained from heaters of $T = 750$ K for polarization directions (a) parallel and (b) perpendicular to the heater long axis (Yat-Yin Au et al. 2008).

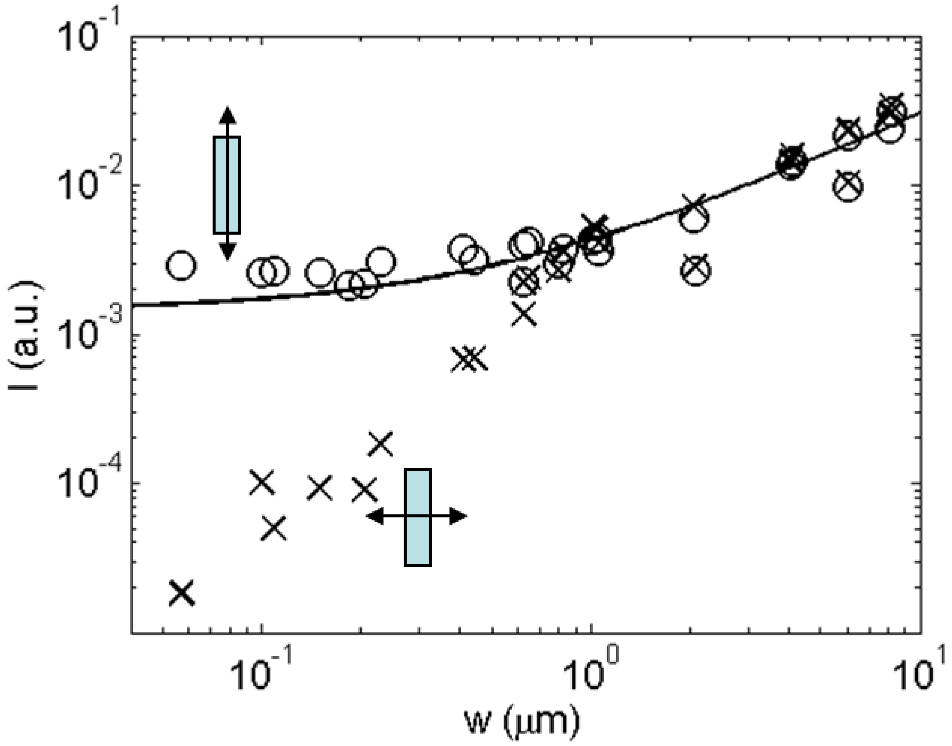

Figure 2.11: Integrated intensity as a function of heater width w for both parallel (circles) and perpendicular polarization (crosses) (Yat-Yin Au et al. 2008).

w Figure 2.11 is obtained. Circles and crosses represent parallel and perpendicular polarizations respectively. The intensity dropped from $I(w = 8.0\ \mu\text{m}) = 3 \times 10^{-2}$ to $I(w = 1.0\ \mu\text{m}) = 4 \times 10^{-3}$ for $w = 8.0\ \mu$m and $w = 1.0\ \mu$m heaters respectively, independent of polarization direction. The ratio between the observed intensities gives

$$\frac{I(w = 8.0\ \mu\text{m})}{I(w = 1.0\ \mu\text{m})} \approx 7.5 \tag{2.33}$$

compared to factor 8.0 between the heaters surface areas. This agrees with the classical theory of blackbodies, that the total radiation should scale with the heater surface area. However, as the heater's width decreases further below 1 μm, the integrated intensity for the parallel polarization consistently stabilize at a finite value around $I_{\text{Parallel}} = 3 \times 10^{-3}$. This indicates that at these length scales, the heater's surface area is no longer the dominating factor in determining the radiation intensity for the parallel polarization. On the other hand the intensity of the perpendicular polarization continues to decrease with heater width in the $w < 1\ \mu$m range. This results in strongly polarized emission from heaters with $w < 0.8\ \mu$m, in accordance with the results from Ingvarsson et al. (2007) discussed in section 2.4.

Let us define the intensity ratio

$$r(w) = \frac{I_{\text{perp}}(w)}{I_{\text{para}}(w)} \tag{2.34}$$

where $I_{\text{perp}}(w)$ and $I_{\text{para}}(w)$ represent the integrated intensities of a heater of width w for perpendicular and parallel polarization respectively. We also define the *reduced intensity ratio* at a given width w as

$$\hat{r}(w) = \frac{r(w)}{r(8\ \mu\text{m})} \tag{2.35}$$

Figure 2.12 shows experimental data of the reduced intensity ratio averaged over three different spectral windows: $2000 - 2500$ cm^{-1} (red), $2500 - 3000$ cm^{-1} (green) and $3000 - 3500$ cm^{-1} (blue). The reduced intensity ratio for all spectral windows start out at 1.0 in the wide heater limit ($w > 2.0\ \mu$m) and approach zero in the narrow width limit ($w < 0.4\ \mu$m). As w decreases we see that $\hat{r}(w)$ drops at larger heater widths w as lower energy windows are used ($E = hck$, so higher k means higher energy). This is another manifestation of the shift of the perpendicular polarization spectral peak to higher wavenumber shown in Figure 2.10b. Furthermore a resonance-like bump appears in Figure 2.12 before attenuation, with the data from the higher energy windows showing more prominent bumps.

A simple model can be used to explain the essential features of these spectra. Let us assume there are individual microscopic electric dipoles both parallel and perpendicular to the heater long axis evenly distributed across the heater's metallic surface. Further assume they are being continuously stimulated by the thermal environment resulting in radiation at their natural oscillation frequency ω with polarization in the parallel

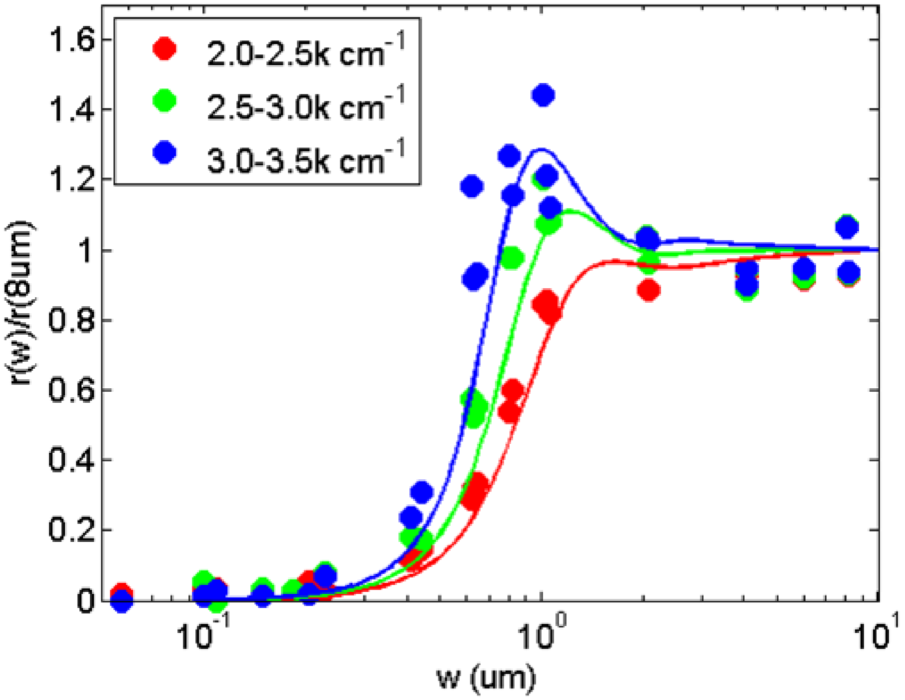

Figure 2.12: Reduced intensity ratio as a function of heater width w averaged over values in the ranges $2000-2500$ cm^{-1} (red), $2500-3000$ cm^{-1} (green) and $3000-3500$ cm^{-1} (blue) (Yat-Yin Au et al. 2008).

or perpendicular direction respectively. An observer located far away will virtually see all the oscillating dipoles at the same point, hence the optical contribution from each oscillator to the optical electric field E will be equivalent. By assuming that the i-th dipole is located at $\mathbf{r}_i$ on the heater surface and oscillating with an amplitude $P(\mathbf{r}_j)$ the intensity can simply be expressed by

$$I = \langle |E|^2 \rangle = \left\langle \left| \sum_i P(\mathbf{r}_i) \right|^2 \right\rangle = \sum_{i,j} \langle P^*(\mathbf{r}_i) P(\mathbf{r}_j) \rangle \tag{2.36}$$

where the angular brackets denote time averaging. $\langle P^*(\mathbf{r})P(\mathbf{r}')\rangle$ is recognized as the correlation function over all possible values of $\mathbf{r}$ and $\mathbf{r}'$ on the heater surface. The individual dipoles should in the absence of collective surface waves (i.e. surface plasmons) oscillate independently from each other [i.e. $\langle P^*(\mathbf{r})P(\mathbf{r}')\rangle \propto \delta(\mathbf{r}-\mathbf{r}')$]. The dependence of the intensity data on the heater width can be understood by the fact that surface plasmons travel mostly parallel to the direction of charge oscillations and are therefore affected in the region when $w < 1$ μm (Carminati & Greffet 1999). Across the width of the heater, dipole oscillations resulting in parallel polarized radiation do not interact through surface plasmons and therefore correlation between these dipoles is minimal, whereas dipole oscillations resulting in perpendicular polarization are communicated by surface plasmons and are therefore strongly correlated. Therefore we expect radiation with parallel and perpendicular polarization to respond differently when the heater width varies.

Since for the perpendicular polarized case correlation between dipoles across the heater width is likely to be mediated by surface plasmons the correlation function is assumed to take the form $\langle P^*(\mathbf{r})P(\mathbf{r}')\rangle = \Theta(\omega, T)g(x - x')$ where

$$g(x) = \exp\left(-\frac{|x|}{\delta}\right)\cos\left(\frac{2\pi x}{\lambda}\right) \tag{2.37}$$

where λ is the wavelength of the corresponding surface plasmon for a given wave number of radiation and δ represents the correlation decay length. λ is related to the electromagnetic wave in free space with wavelength λ_{free} by

$$\lambda = \lambda_{\text{free}}/n \tag{2.38}$$

where n is the effective refractive index for the surface wave. By assuming a penetration depth of $\lambda/2\pi$ and averaging between the free space above and the substrate below, an effective refractive index of $n = 1.665$ is determined. The function $g(x)$ describes a traveling plasmonic wave with attenuation. $\Theta(\omega, T)$ is assumed to describe the frequency ω and temperature T dependence in position x and x'. Its contribution does not enter the final result of the reduced intensity as upon division in Equation 2.35 it disappears. The correlation function is assumed to reflect with 180° phase shift at the two edges and to obey the principle of superposition (well know for plasmons). The overall correlation between x and x' after taking the existence of edges into account becomes

$$f(x, x') = \sum_{n=-\infty}^{\infty} (-1)^n g(x - \hat{M}_n(x')) \tag{2.39}$$

where $M_n(x')$ denotes the n-th image of x' on the two sides behind the edges i.e.

$$\hat{M}_n(x') = wn + (-1)^n x' \tag{2.40}$$

The heater is assumed to be located within $x \in [-0.5w, 0.5w]$. By inserting Eqs. 2.39 and 2.40 into Equation 2.36 the intensity I_{perp} can be calculated by solving the convolution problem. The parallel polarization intensity I_{para} is simply obtained by linearly fitting the parallel polarization data in Figure 2.11. Writing $I_{\text{para}} = \alpha w + \beta$ and fitting gives $\alpha = 0.00288$ and $\beta = 0.00143$. The fitted function is plotted in Figure 2.11. Using the fitted function for I_{para} and I_{perp} from Equation 2.36 the reduced intensity ratio $\hat{r}(w)$ can be produced, the result is shown as solid line in Figure 2.12.

Even though the above analysis is by no means rigorous representation of the physical system it succeeds reproducing the fact that $\hat{r}(w)$ drops at larger heater widths w and the height of the resonance bump increases at higher wavenumbers. The simple model provides certain physical insight into how surface plasmons play an important role in the observed variation of radiation intensity with heater width. From this analysis we conclude that the bump occurring around 1.0 μm in Figure 2.12 corresponds to a $\lambda/2$ resonance.

2.6 Coherence properties

As discussed in section 2.3 blackbody radiation is considered incoherent and unpolarized and the spectrum can be described by Planck's law in Equation 2.11. The coherence properties of light are important for most characterization methods that use light to probe the sample under investigation. IR thermal light sources are especially important due to their applications in nanoscale molecular characterizations, biological sample characterizations and in the development of efficient thermoelectric radiation sources.

In this section a short overview of the results from coherence measurements from our collaborators at IBM will be given (Levente J. Klein et al. 2008). All figures in this section are from Levente J. Klein et al. (2008) and are used with the author's permission.

We know from elementary physics that two waves can add together to create a larger wave (*constructive interference*) or subtract from each other to create a smaller wave (*destructive interference*), depending on their relative phase (Young & Freedman 2007). If the two waves have a constant relative phase they are said to be coherent and the *degree of coherence* is measured by the *interference visibility* (Hecht 1998).

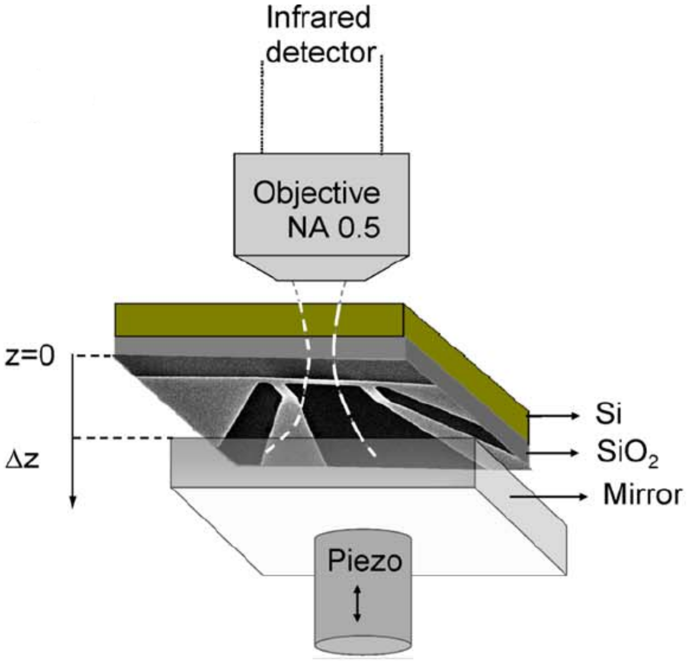

Figure 2.13: The experimental system used to interfere the thermal radiation from a microheater with its image in an Al coated mirror attached to a piezotube (Levente J. Klein et al. 2008).

Platinum microheaters of fixed aspect ratio ($l/w = 10.0$), widths w from 125 nm to

2 μm ($\Rightarrow$ lengths from 1.25 μm to 20 μm) and Pt thickness $d = 45$ nm were fabricated as described in section 2.2. The experimental setup is illustrated in Figure 2.13. An Al coated mirror attached to a piezotube (10 μm travel distance range) is positioned close to the microwire. Both the thermal radiation from the heater and from its mirror image is passed through the Si/SiO$_2$ substrate, which is transparent in the measured range. The radiation signal is then observed as a function of the optical path difference $2\Delta z$ using a liquid N$_2$ cooled InSb detector (sensitive in the $3.0 - 5.0$ μm wavelength range). Due to a finite depth of focus of the detection system, only the radiation from the heater is detected when the mirror is far away, but as the mirror approaches the microwire the radiation from the image starts to contribute. The radiation signal observed can then be described by

$$I = I_1 + I_2 + 2\sqrt{I_1 I_2} \mathrm{Re}\ \gamma_{12}(\tau) \tag{2.41}$$

where I_1 is the thermal emission intensity from the heater and I_2 the intensity from its image. The coupled term originates from the self-interference between the emission from the heater and its image; $\gamma_{12}(\tau)$ is the *complex degree of coherence function* and τ the time delay between the radiation coming from the heater and its image. The coherence function $\gamma_{12}(\tau)$ describes the time correlation between the heater's radiation and its image. Hence it determines the appearance of interference fringes (Hecht 1998). The degree of coherence is determined from the magnitude of the coherence function $|\gamma_{12}(\tau)|$. A perfectly coherent light source has degree of coherence $|\gamma_{12}(\tau)| = 1.0$ and a completely incoherent light source has $|\gamma_{12}(\tau)| = 0.0$. Since the radiation from the heaters originates from thermal fluctuations it was expected *a priori* to be only slightly coherent $|\gamma_{12}(\tau)| \ll 1.0$.

As discussed before, the fringe visibility is used to compare the interference for different wires and temperatures and is defined by

$$V = \frac{2I_{\mathrm{max}} - I_{\mathrm{min},1} - I_{\mathrm{min},2}}{2I_{\mathrm{max}} + I_{\mathrm{min},1} + I_{\mathrm{min},2}} \tag{2.42}$$

where I_{max} is the value of the maximum interference peak and $I_{1,\mathrm{min}}$ and $I_{2,\mathrm{min}}$ are the two neighboring minima. An example of such interference fringes is given in Figure 2.14(a). For thermal radiation signals with similar amplitude ($I_1 \approx I_2$) it can be shown (Hecht 1998) that the measured fringe visibility is equal to the degree of coherence

$$V = |\gamma_{12}|\ . \tag{2.43}$$

This relation allows estimating the degree of coherence using the fringe visibility results. The degree of coherence for a radiation source with a known spectral distribution $I(\nu, T)$ can also be theoretically calculated by

$$\gamma_{12}(\tau) = \int_0^\infty I(\nu, T) e^{-2\pi i \nu \tau} d\nu \tag{2.44}$$

where ν is the frequency and τ is the time delay between the interfering light sources. The time delay can be determined by the optical path difference $\tau = 2\Delta z/c$, and

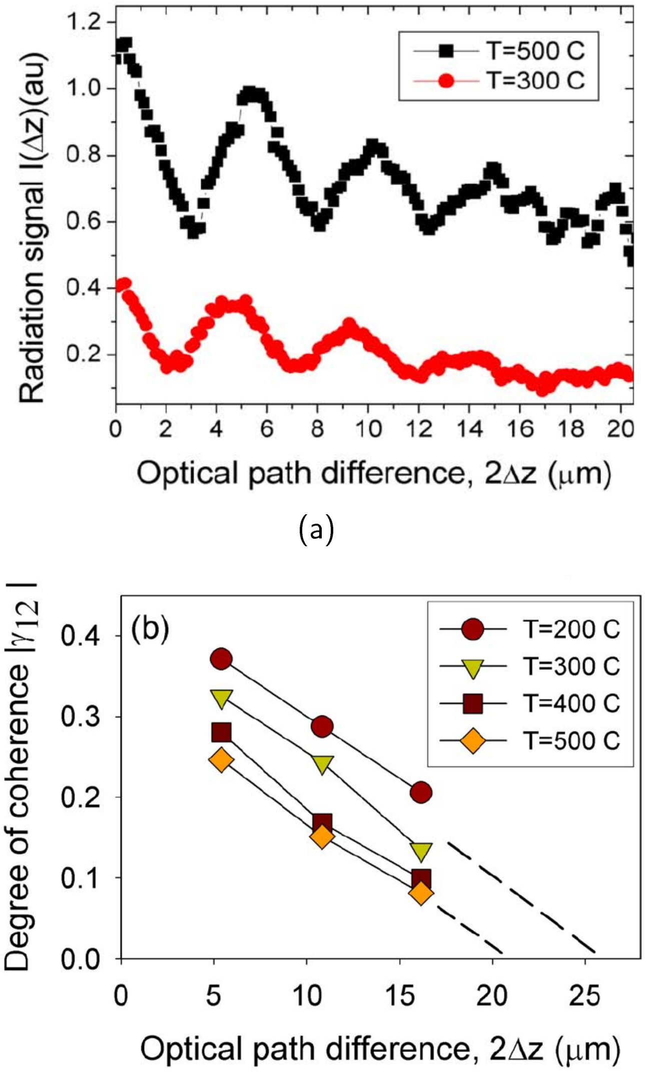

(a)

(b)

Figure 2.14: (a) Interference fringes for a $w = 125$ nm heater at 300°C and 500°C. (b) The fringe visibility as a function of the optical path difference for a $w = 125$ nm heater at different temperatures.

can be used with Equation 2.44 to calculate the coherence properties of blackbody radiation. In Figure 2.14(a) the interference fringes from a narrow $w = 125$ nm heater at 300°C and 500°C are shown. The peak-to-peak fringe distance corresponds to 5 μm average detection wavelength, in good agreement with what was expected from the wavelength form of Planck's law Equation 2.22. Calculating the fringe visibility using Equation 2.42 and plotting the result as a function of optical path difference $2\Delta z$ for different temperatures gives Figure 2.14(b). The coherence length can then be determined from the figure as the distance where the fringe visibility reaches 10% (Berkley & Wolga 1962). An increase in the coherence length from ~ 20 μm at 500°C to $\sim 26\ \mu$m at 300°C is observed. For comparison the classical blackbody radiator has a coherence length of $\sim 2\ \mu$m at 600°C and $\sim 5\ \mu$m at 300°C. A much longer coherence length is therefore observed, than what is expected from a blackbody, but it decreases with increased temperature as for a blackbody.

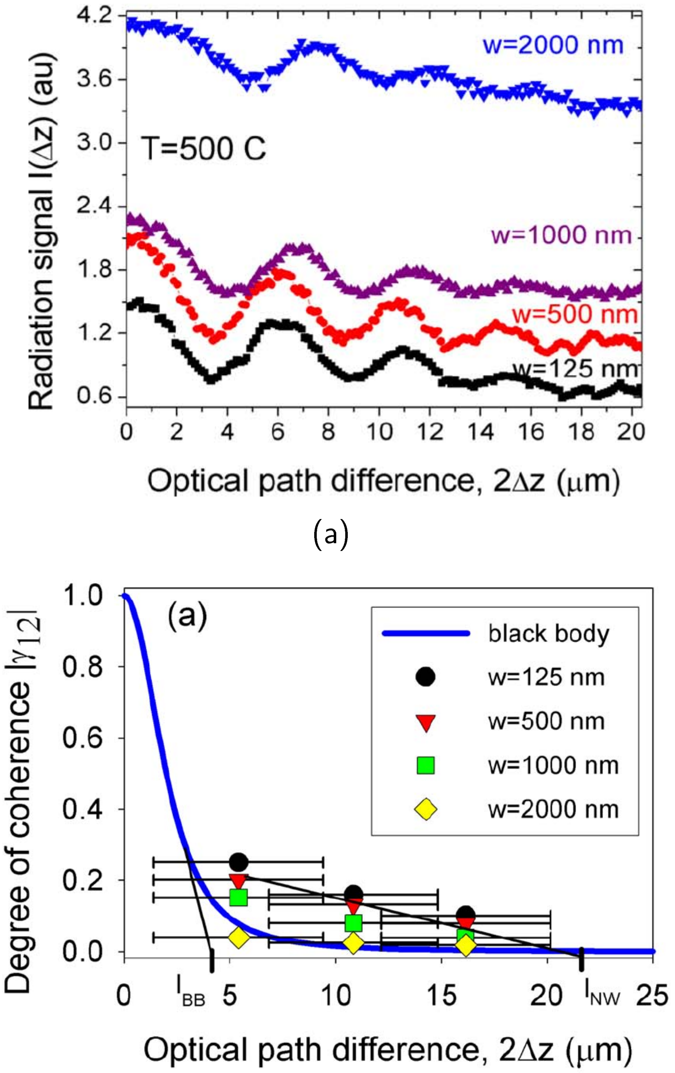

(a)

(b)

Figure 2.15: (a) Interference fringes for heaters of different sizes at 500°C. (b) Degree of coherence as a function of optical path difference for microheaters of variable width w compared to that of an ideal blackbody.

In Figure 2.15(a) we see the interference fringes from wires of different sizes, all at temperature $T = 500$°C. By comparing the degree of coherence for the four wire sizes to the theoretical degree of coherence for a perfect blackbody, Figure 2.15(b) is obtained. The coherence length for blackbody radiation is $\sim 4\ \mu$m while the 125 nm wide heater yields a five times larger coherence length of $\sim 20\ \mu$m. A general trend is observed, wider and larger heaters have shorter coherence lengths and as the width approaches $w = 2$ μm it becomes comparable with blackbody radiation.

2.7 Potential applications

We have seen in previous discussions that narrow wires show a high level of coherence, strong polarization and enhanced dipole like far-field pattern. The coherence enhancement in far-field radiation corresponds to a strong near-field due to less efficient cancellation of higher order multipole terms (Martin et al. 2001). All this indicates that the heaters can prove to be a good near-field source. A strong near-field is interesting for variety of applications.

Theoretically it has been predicted that strongly overlapping near-fields provide a better heat transfer mechanism than when the objects are in direct physical contact (Domingues et al. 2005). This might to be of importance in thermovoltaic (TPV) energy conversion applications (Laroche et al. 2006). There is also interest in confining the near-field to an extremely small region for applications such as thermally assisted magnetic recording (Koji Matsumoto et al. 2006) and near-field optical microscopy (Cvitkovic et al. 2006). Other potential applications would be e.g. solar energy utilization, space thermal management, high-efficiency light sources etc. (Ingvarsson et al. 2007).

In this section we will discuss two applications using the microheaters, where the physical concept has already been proven.

2.7.1 Thermally excited near-field source

Despite many impressive advances in near-field optics and microscopy it remains a challenge to create a reliable strong near-field source, which can be used to excite samples with a spatial resolution far beyond the diffraction limit. In near-field optical microscopy applications there are two conventional approaches to the near-field source. One is the aperture-based method using the field that “leaks” through upon illumination of a sub-wavelength aperture as seen in 2.16(a). This method provides excellent background rejection but typically produces weak near-fields. The second is the aperture-less method that uses external electromagnetic field to excite a sharp probe tip in order to generate a highly localized near-field as seen in figure 2.16(b). In contrast to the aperture-based method the apertureless method can give strong near-field, but it suffers from a strong background illumination (low near-field vs. far-field intensity ratio).

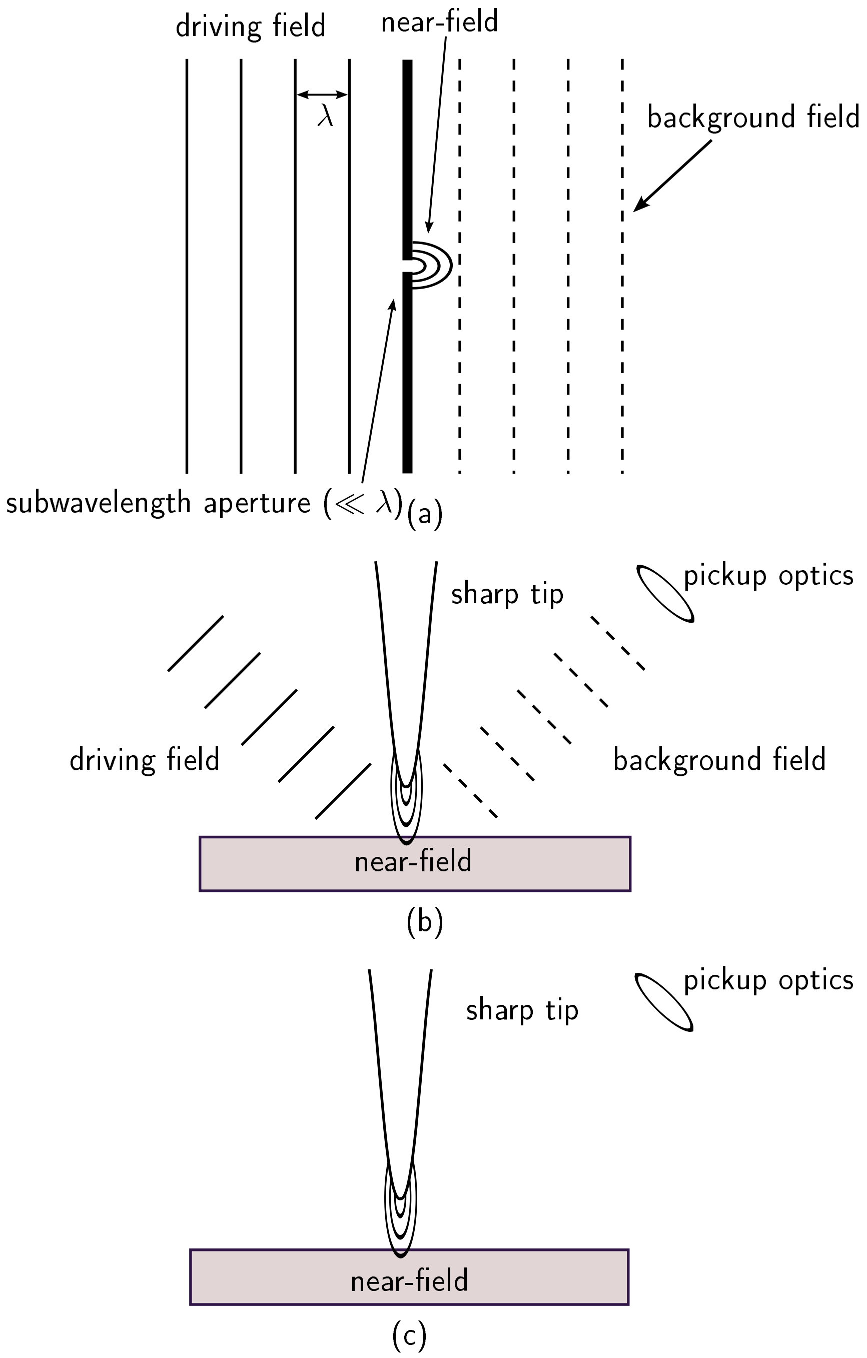
driving field
near-field
λ
background field
subwavelength aperture (≪ λ)
(a)
sharp tip
pickup optics
driving field
background field
near-field
(b)
sharp tip
pickup optics
near-field
(c)

Figure 2.16: The are two conventional approaches to the near field-source: (a) the aperture-based source and (b) the aperture-less source. (c) The thermally excited near-field source needs no external driving field.

Our idea is to place a microheater at a probe tip and use it as a electrically (thermally) driven near-field source, without the need for any external driving field, as seen in 2.16(c). An application for a U.S. patent has already been filed (still in progress), and the physical concept been proven (Hendrik F. Hamann et al. 2006*b*). A heated IR near-field source was approached by a pyroelectric detector (near-field receiver) and the transferred total power from the source to the detector measured as a function of the distance between the two. A very strong and short-ranged power flow was revealed within the near-field region validating the claim of generation of a significant near-field radiation from the thermally excited source. The decay length constant ($1/e$) was estimated $\sim$ 10 nm, which promises comparable lateral resolution to existing technology. The estimated power transfer from the tip to the pyroelectric detector is estimated to be in the μW range, which is sufficiently strong for many applications (Martin et al. 2001).

2.7.2 Phase-change storage

Phase-change memory is a type of non-volatile digital medium. One example of such material is $Ge_2Sb_2Te_5$ (GST), which is important in modern optical and electrical storage due to how rapidly it can be switched between amorphous and crystalline phases by applying appropriate heat pulses. GST is amorphized by pulsed heating above the melting temperature ($\sim$ 600°C) for $\sim$ 10 ns with subsequent rapid cooling. Recrystallization on the other hand is accomplished by a heat pulse below the melting temperature but above the glass-transition temperature ($\sim$ 200°C) for $\sim$ 100 ns.

In most commercial phase-change storage applications the heat pulses are achieved by a sharply focused laser diode, and the state of the recorded bits sensed with the same laser at a lower power. Although phase-change storage is already widely used in optical information technologies (e.g. DVD, CD-ROM) the storage density is limited by the diffraction limit of the laser ($\sim$ 15 Gb inch^{-2} with a blue laser diode), which will impede further direct improvements of the technology in the future.

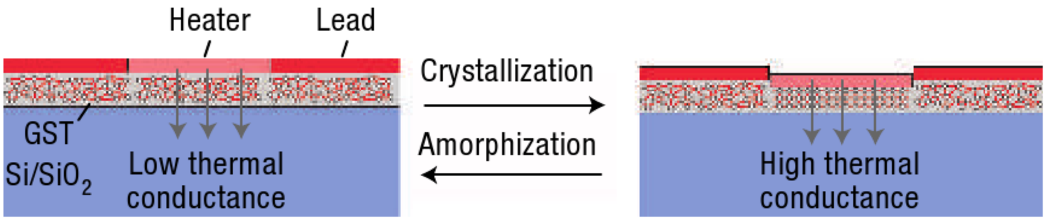

Figure 2.17: Illustration of an all-thermal-phase-change storage concept (Hendrik F. Hamann et al. 2006*a*)

Our collaborators at IBM have already demonstrated the use of microheaters to write, erase and read the phase of GST at competitive speeds (Hendrik F. Hamann et al.

2006*a*). A microheater of size 1×3 μm^2 was directly patterned on a phase-change film as shown in Figure 2.17. Amorphization was realized by a 10 ns 1.5 V pulse ($\sim$ 700°C) whereas 0.7 V for 100 ns ($\sim$ 500°C) was sufficient for crystallization. The recording speeds were governed by the amorphization and crystallization kinetics. The phase of the film can be read using low currents by sensing the thermal impedance of the heater which depends on the phase of the film beneath the heater.

3 FTIR spectrum measurements

As discussed in section 2.5 the radiation spectrum has been measured for wavenumbers $\tilde{\nu}$ from 1800 cm^{-1} up to 10000 cm^{-1}. The peak of the heater spectra is however expected in the unknown lower wavenumber region, somewhere in the $1000 - 1800$ cm^{-1} range. In this section an attempt the measure the spectra above 600 cm^{-1} using heater arrays will be discussed. A strong emission observed from the substrate will be addressed along with some ideas how to suppress its contribution.

3.1 Experimental setup

The experimental system used is shown in Figure 3.1, and is similar to that discussed in section 2.5. The numerical superscripts in the following text refer to elements in Figure 3.1.

The microheater sample^1 is mounted on a nanopositioning piezo stage^2, controlled by a piezo controller^3. A computer^5 controlled sourcemeter^4 is connected to the heater contact pads, and is used to measure and regulate the power dissipation in the heater. The emitted light is collected using an reflective objective^6, passed through a linear wire grid polarizer^7 and into a FTIR spectrometer^8.

After traversing through the FTIR spectrometer the light passes through an iris diaphragm^9 which is used to block other light than that from the heater. The light is then focused with a ZnSe plano-convex lens^{10} ($f = 50\,\mathrm{mm}$) into a light detector^{11}.

A few different detectors and preamplifiers^{12} are available in our lab. In the experiment discussed in section 2.5 an IS-1.0 (InSb) detector from Infrared Associates, sensitive in the $1800 - 10000$ cm^{-1} range was used. Here however a liquid N_2 cooled FTIR-16-0.1 MCT (mercury cadmium telluride) detector from Infrared Associates, sensitive in the $625-5000$ cm^{-1} range is used. The preamplifier is connected to the FTIR spectrometer, where the signal is transferred to the computer and the spectra extracted.

A Fourier-transform infrared (FTIR) spectrometer is basically an interferometer which the incoming IR light is guided through. By splitting the beam of light into two paths and varying one of the pathlengths continuously (by moving a mirror) a interference

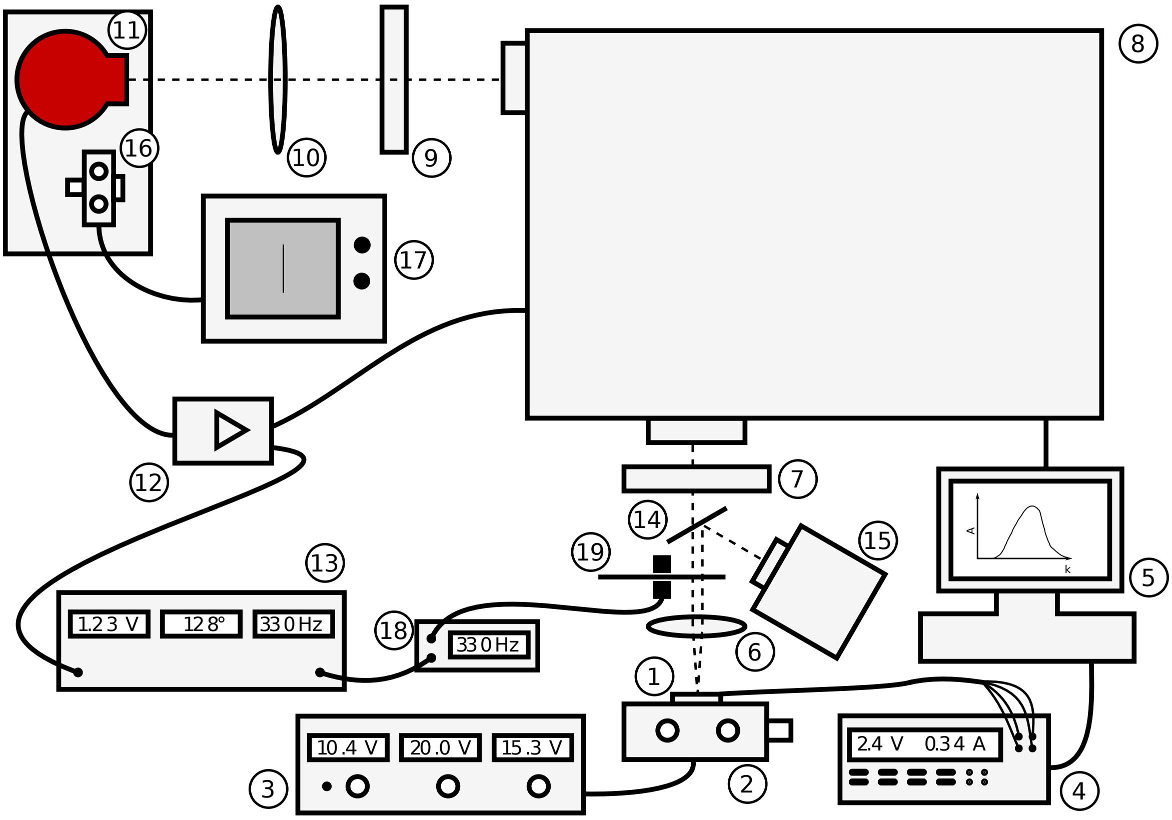

Figure 3.1: Schematic of the FTIR experimental setup used. Detailed explanation is found in main text.

pattern is produced. Performing a fast Fourier transform (FFT) on this signal then gives the emission spectra from the radiating samples.

For alignment a light from a halogen lamp[15] is reflected by an half-transparent mirror[14] onto the sample. The (visible) light is then reflected back from the heater surface and through the whole optical system. The detector and a CCD camera[16] are placed on a translational stage so that both can be moved easily into the optical path. A coarse alignment is first made by optimizing the position of the lenses and moving the heater into the field of view by recording its position with a CCD camera and monitoring it on a screen[17]. A finer alignment is then made by modulating the light with a chopper[19], while maximizing the observed signal in a lock-in amplifier with respect to the positions of the heater and lenses. The mirror is then removed and the halogen lamp turned off, and the same maximization process repeated with the IR light from the heater. Then the chopper is removed and the spectra can be measured.

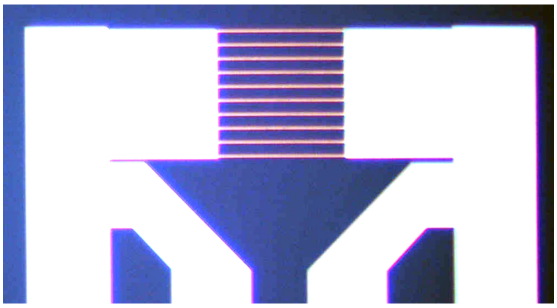

Figure 3.2: Microheater array with ten heaters if length $l = 50$ μm and width $w = 0.6$ μm.

3.2 Results

The *signal-to-noise ratio* (SNR) of the FTIR-16-0.1 MCT detector and amplifier turned out too be to low for measuring the emitted radiation from single microheaters. Thus platinum heater arrays with ten heaters of fixed length $l = 50$ μm and widths $w = 0.6$ μm as shown in Figure 3.2 were fabricated as discussed in section 2.2.

Their spectrum was measured for polarization directions both parallel and perpendicular to the heater. The result is shown in Figure 3.3. In the figure we also see the spectra measured from the substrate 50 μm from the actual heater structure, which is heated up due to the high power dissipation in the microheater array ($\sim$ 1.5 W). The exact temperature of the substrate is not known, therefore we cannot compare the

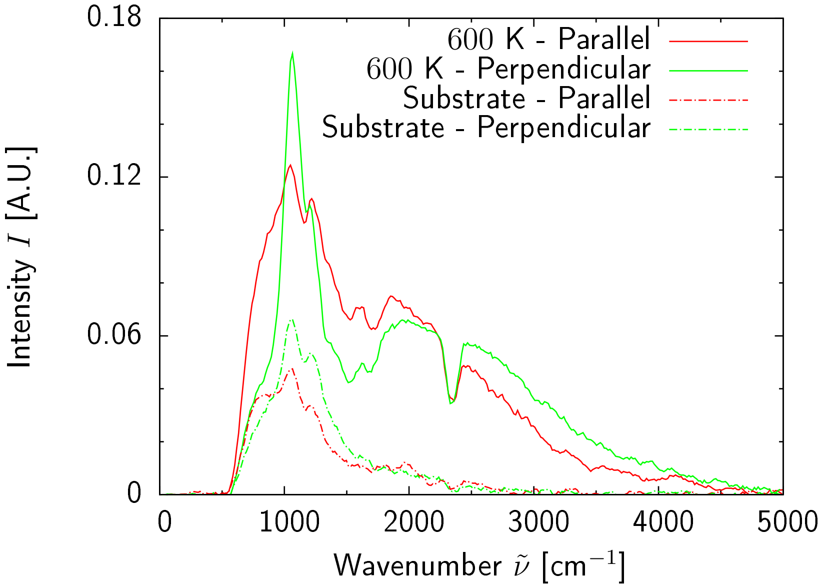

Figure 3.3: Thermal spectra from the heater array and the substrate for polarization directions both parallel and perpendicular the heaters.

amplitude of the heater and substrate spectra directly.

The spectra have not been corrected with respect to the system response curve, hence we see both water vapor ($\sim$ 1700 cm^{-1}) and CO_2 ($\sim$ 2400 cm^{-1}) absorption dips. The alignment of the system is not perfectly reproducible and it has been shown that the transmission is not the same for the two polarization directons, henceforth the amplitude can not be compared between measurements. However, by comparing the shape of the spectrum from the heater array and from the substrate we can speculate that from $\sim$ 600 cm^{-1} to $\sim$ 1700 cm^{-1} the radiation from the substrate dominates that of the heater array, and up to $\sim$ 3000 cm^{-1} some substrate contribution is expected. The peaks observed around $\sim$ 1100 cm^{-1} originate from the substrate, and are most likely due to an oxide interstitial (anti-symmetric stretching) defect in the silicon (Stavola 1999). However, the broad peak seen between $\sim$ 1600 cm^{-1} and $\sim$ 3500 cm^{-1} we believe stems from a surface plasmon perpendicular to the long axis of the heaters, as discussed in section 2.5. We would also expect to see a peak for the parallel polarization. However, in this case the peak position is expected to be at lower energy (see section 2.5) and the shape of the spectrum should also agree roughly with the classical blackbody spectrum. In this case it is merged with the substrate peak, and there is no simple way to separate the two of them to extract the heater contribution.

As discussed above heater arrays were used to enhance the radiation signal. The use of heater arrays however has a few drawbacks. When using single heaters the power regulation system will keep the power dissipation in the wire constant despite changes in the structural properties due to electromigration and annealing. However when arrays are used the breakdown mechanisms will not change the properties of all the heaters at the same rate, causing variation in the power dissipation and temperature of individual heaters. For the same reason the breakage of one heater will increase the power dissipation in the others, which can cause a chain reaction and eventually lead to a breakdown of the whole structure. By using a fixed voltage instead of fixed power it is however possible to increase the stability of the structure, but due to electromigration and annealing effects the resistivity of the heaters will increase and therefore slowly decrease the power dissipation and the temperature of the array. In both cases the heat transport is expected to be lower for the center heaters, causing higher temperature than in the outermost heaters. This difference and drift in temperature of individual heaters makes the array structure ill-suited for experiments and application where stable fixed temperature is needed. Furthermore the array geometry and the high power needed gives rise to substantial substrate radiation as we saw in the last section.

Although we do not expect as strong substrate radiation from single heaters as from heater arrays, we nevertheless see that the silicon/silicon dioxide substrate is not well suited for experiments and applications in the 600 cm^{-1}–2500 cm^{-1} region (wavelength: $5 - 16$ μm). Figure 3.4(a) shows the transmittance through a 10 mm thick sample of silicon, but high transmittance implies low absorption and emissivity according to Kirchhoff's law of thermal radiation (Sato 1967). For convenience the relation between

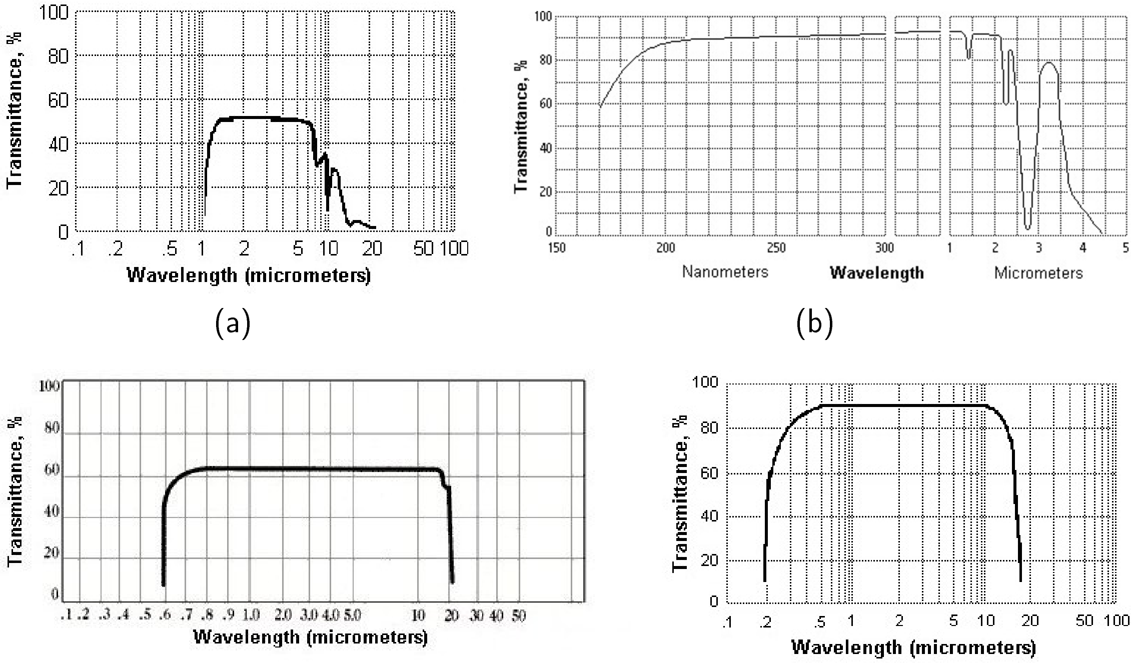

(a) (b)

(c) (d)

Figure 3.4: Transmittance through a 10 mm thick samples of (a) silicon (Si), (b) silicon dioxide (SiO_2), (c) zinc selenide (ZnSe) and (d) crystalline sodium chloride (NaCl) from ALKOR Technologies (2009).

the wavelength λ and the wavenumber $\tilde{\nu}$ is shown in Figure 3.5

It shows that silicon has high transmittance in the 1400 $\text{cm}^{-1} - 6000\ \text{cm}^{-1}$ ($1.5 - 7\ \mu$m) range, and therefore low emissivity. The emissivity is however high from 600 cm^{-1} to 1400 cm^{-1} ($7 - 16\ \mu$m). The transmittance through silicon dioxide shown in Figure 3.4(b) suggests that below 5000 cm^{-1} (above 2 μm) some emission contribution can be expected. This confirms that the silicon/silicon dioxide substrate is not well suited as a heater substrate when radiation below 1400 cm^{-1} ($> 7\ \mu$m) is of any importance.

To get rid of the emission from the substrate, other substrate materials with low emis-

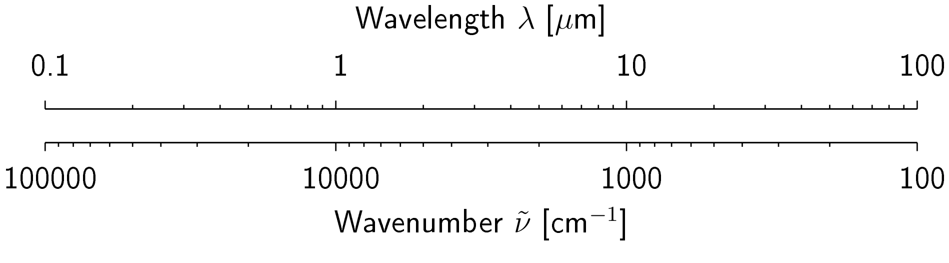
Wavelength λ [μm]
0.1
1
10
100
100000
10000
1000
100
Wavenumber $\tilde{\nu}$ [cm^{-1}]

Figure 3.5: The relation between the wavelength λ and the wavenumber $\tilde{\nu}$

sivity in this range could be used. The substrate also has to have low thermal and electrical conductivity, as discussed in chapter 4. One option is zinc selenide (ZnSe) which has fixed transmittance of $\sim 64\%$ from 600 cm^{-1} to 12500 cm^{-1} ($0.8 - 17$ μm), as shown in Figure 3.4(c). Cadmium selenide (CdSe) and cadmium telluride (CdTe) also have similar properties, i.e. a high fixed transmittance in the 600 cm^{-1} $-$ 5000 cm^{-1} ($2.0 - 17$ μm) range of 70% and 67% respectively. These substrates are however all rather expensive for day-to-day laboratory usage, but could be useful expedient for some applications.

A more inexpensive option is crystalline sodium chloride (NaCl) or potassium chloride (KCl). Both materials have high transmittance of more than 80% in the $600 -$ 30000 cm^{-1} ($0.3 - 16$ μm) range, as shown for NaCl in Figure 3.4(d). They are however both hygroscopic, which makes the sample more sensitive to moisture and could make the fabrication more difficult.

The heating of the substrate could also possibly be decreased by using suspended heaters without any direct contact to the substrate. This can be achieved by growing the heaters on top of silicon/silicon dioxide substrate and use chemical etching (i.e. hydrofluoric acid) to remove the silicon dioxide around and under the platinum film and if needed also part of the silicon layer (using KOH solution) as described in Zhang et al. (2005).

By using any of the suggested substrates or suspended heaters the dielectric surroundings of the heater changes. This might affect the forming of collective surface waves, and possibly change the optical properties of the heaters.

4 Finite element analysis

Nowadays computers are relatively inexpensive and powerful. Therefore the use of computer models as a design tool has grown tremendously in recent years. The most used method is probably the *finite element method* (FEM), but it can be used in variety of fields to reduce both design and production cost significantly. In this chapter the main objective will be FEM analysis of the microheater structure, where temperature distributions, temperature-power relations and other characteristics will be investigated.

4.1 The finite element method (FEM)

The finite element method is a numerical procedure that has been developed into a key technology in the modeling and simulations of various engineering systems. The method finds approximate solutions of partial differential equations (PDE) as well as of integral equations to solve problems involving stress analysis, heat transfer, electromagnetism, fluid flow and much more. The development of the method began in earnest in the mid 1950s, and was mostly formalized by civil engineers for structural analysis (Desai & Kundu 2001), but was soon extended to other fields as well. By the late 1950s, the method had developed into essentially in the form used today (Zienkiewicz et al. 2005), and in late 1960s NASA developed the first finite element software, NASTRAN. Even though a FEM software was already being used in late 1960s, the method was not provided with a rigorous mathematical foundation until in 1973 (Strang & Fix 1973). The method has gained popularity in the academia as well as in industry because of its versatility and how easily it can be applied to problems involving complex geometries and boundaries.

The basic idea, is to approximate a continuous system having infinite degrees of freedom with a computational model having finite degrees of freedom as follows: After the geometry of the structure has been modeled it is subdivided, or *discretized* into a suitable number of small pieces called *finite elements*. This process is generally called *meshing*, and is mostly done automatically by an *meshing algorithm*, although manual refinement might be necessary. The interfaces between the elements are called *nodal lines* or *nodal planes*, and the intersection of the nodal lines *nodal points*. Suitable choice of elements is highly dependent on the problem and characteristics of the body.

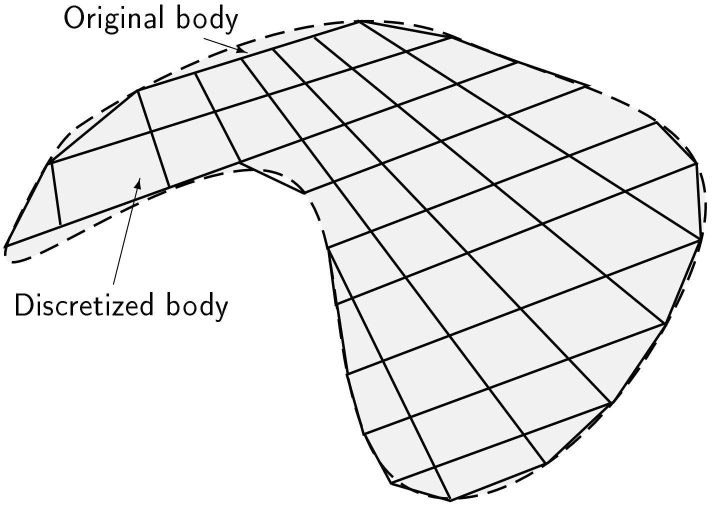

Figure 4.1: Discretization for an irregular boundary.

One dimensional bodies (e.g. beam) are most commonly subdivided in line elements, whereas for two-dimensional bodies, triangles and quadrilaterals are the natural choices. Three-dimensional bodies are usually partitioned by hexahedrons or tetrahedrons. If the boundary of the body is irregular it can still be approximated by straight lines as shown in Figure 4.1, but more advanced approximation to the boundary can also be applied (e.g. quadratic functions).

Within each of the elements, simple smooth functions (e.g. polynomials), so called *shape functions* are used to describe the distribution of the unknown quantity ϕ (e.g. temperature, electric field) over the domain of the element. We write ϕ as

$$\phi = N_1\phi_1 + N_2\phi_2 + N_3\phi_3 + \ldots + N_m\phi_m \tag{4.1}$$

where $\phi_1, \phi_2, \cdots, \phi_m$ are the values of the unknown quantity at the nodal points and $N_1, N_2, \cdots, N_m$ are the shape functions, or interpolation functions (Desai & Kundu 2001). The element type and the shape function should be chosen carefully to represent the physical system at hand as well as possible. By choosing the appropriate shape functions an exact solution can in some cases be obtained e.g. linear shape functions in case of a first-order linear PDE or quadratic shape functions in case of a second-order linear PDE. In general the solution obtained is not exact and it can be highly dependent on mesh density and element type. The computation time can increase substantially with the number of elements, therefore it is important to use a fine mesh only where the rate of change of the unknown quantity is great and a coarser mesh elsewhere.

A number of alternative methods are possible for derivation of element equations. The most important being the *variational method* and the *method of weighted residuals* (MWR). The variational method is based on minimization of a functional and is applicable when a variational principle corresponding to the problem at hand exists (e.g. Hamilton's principle). The method of weighted residuals however is applicable to problems for which the differential equations are known regardless of the existence of a variational principle. The MWR is based on minimization of the residual left after an approximate or trial solution is substituted into the differential equations governing a problem (Desai & Kundu 2001). A number of alternative schemes are available to achieve the minimization of the residues; the most popular being the *Galerkin method.*

Use of either of the two foregoing methods will lead to equations describing the behavior of an element, which are commonly expressed as

$$\mathbf{k}\vec{q} = \vec{Q} \tag{4.2}$$

where $\mathbf{k}$ is *element property matrix*, $\vec{q}$ is a *vector of unknowns* at the element nodes and $\vec{Q}$ is the *element nodal forcing vector.* These variables have different names depending on the fields e.g. in stress analysis $\mathbf{k}$ is called the stiffness matrix but in heat conduction the conductivity matrix. To obtain equations for the behavior of the entire body the element equations are assembled into a global equation. By modifying the global equation to take the boundary and initial conditions into account the final set of linear equations is obtained

$$\mathbf{K}\vec{r} = \vec{R} \tag{4.3}$$

where $\mathbf{K}$ is a *assemblage property matrix*, $\vec{q}$ is a *assemblage vector of unknowns* at the nodes and $\vec{R}$ is the *assemblage nodal forcing vector.* Equation 4.3 can be solved using any of the well known algorithms for solving a system of linear equations e.g. Gaussian elimination or some iterative method.

In case of nonlinear material properties (e.g. thermal conductivity that changes with temperature) or coupled fields (e.g. piezoelectricity or thermal electric coupling) more advanced solution schemes are necessary. The Newton-Raphson methods and the Modified Newton-Raphson methods are the most common methods to solve such finite element problems (Zienkiewicz et al. 2005). In the Newton-Raphson scheme the load (e.g. force or heat flux boundary condition) is divided into several load steps and each load step divided into several substeps. In each substep a new property matrix $\mathbf{K}$ is found with regard to $\vec{q}$ and $\vec{R}$ and the solution is found in an iterative way. The modified Newton-Raphson method is the same as the Newton-Raphson method, except the property matrix $\mathbf{K}$ remains unchanged throughout all substeps in each load step and is only reevaluated in the beginning of each load step (ANSYS Inc. 2007).

After solving for the primary quantity, very often additional or secondary quantities must be computed from the primary quantity (e.g. conductive heat flux in the simulation of heat transfer or electric field in electric simulations). This process is usually straightforward once the primary quantities are known, by using the physical relations between the primary and secondary quantities. One concrete example would be finding the electric field $\mathbf{E}$ (secondary quantity) from the voltage potential ϕ (primary quantity) by using some elementary numerical methods and the relation

$$\mathbf{E} = -\nabla\phi\,. \tag{4.4}$$

In recent years many finite element software products have become available, such as the commercial packages Abaqus, ANSYS, Comsol and the open-source software Elmer. We chose ANSYS for the thermal electric analysis of the heater structure, due to its robust meshing features, which are especially important because of the thin film structures, steep gradients and high element aspect ratios.

4.2 PDE's of thermal electric coupling

The heat generation in a microheater originates from resistive heating when electric current passes through the resistive material. This effect is called *Joule heating* and can be formulated by two nonlinear coupled partial differential equations, one describing the temperature field and other the voltage potential.

Heat transfer in continuous solid material can be described by *Fourier's law*

$$\mathbf{q} = -k\nabla T \tag{4.5}$$

where $\mathbf{q}$ is the *local heat flux*, k the material's *thermal conductivity* and T the temperature. The energy balance in an infinitesimal volume can be described by the heat continuity equation

$$\rho C_\mathrm{p}\frac{\partial T}{\partial t} + \nabla\mathbf{q} = P \tag{4.6}$$

where ρ is the material *density*, C_p its *specific heat capacity* and P the *heat generation* per unit volume. Then

$$\rho C_\mathrm{p}\frac{\partial T}{\partial t} + \nabla(-k\nabla T) = P \tag{4.7}$$

is obtained by combining Equation 4.5 and Equation 4.6.

Maxwell's equations tell us that in the absence of a time varying magnetic field

$$\nabla \times \mathbf{E} = 0\,, \tag{4.8}$$

where $\mathbf{E}$ is the electric field. Hence we can express the electric field by

$$\mathbf{E} = -\nabla\phi \tag{4.9}$$

where ϕ is the scalar *voltage potential.* Then we can write the electric current density $\mathbf{j}$ as

$$\mathbf{j} = \sigma\mathbf{E} = -\sigma\nabla\phi \tag{4.10}$$

where σ is the conductivity of the material. By combining the expression for charge conservation

$$\nabla \cdot \mathbf{j} = 0 \tag{4.11}$$

and Equation 4.10 one obtains

$$\nabla \cdot (\sigma \nabla \phi) = 0\,. \tag{4.12}$$

If ϕ were known one could use Equation 4.9 and Equation 4.10 to find $\mathbf{E}$ and $\mathbf{j}$ respectively, and then obtain the heat generation by

$$P = \mathbf{j} \cdot \mathbf{E} = \sigma E^2 = \sigma |\nabla \phi|^2\,. \tag{4.13}$$

Then by plugging Equation 4.13 into Equation 4.7 we get

$$\rho C_{\mathrm{p}} \frac{\partial T}{\partial t} + \nabla(-k \nabla T) = \sigma |\nabla \phi|^2\,. \tag{4.14}$$

So to solve for T and ϕ one has to solve Equation 4.12 and Equation 4.14 simultaneously for the given geometry and boundary conditions. It should be noted that the material properties σ, k and C_{p} are all explicit functions of temperature T and hence also implicit functions of position. This causes high nonlinearity of the system of equations, and an iterative method is needed to solve it.

At the boundary of each subdomain, ANSYS offers a choice between the following boundary conditions for the temperature field: fixed temperature, thermal insulation, fixed heat flux, convective flux and radiation flux. The fixed heat flux, convective flux and radiation flux conditions can all be used simultaneously to account for mixed boundary conditions involving heat transfer due to both convection and radiation:

$$\mathbf{n} \cdot (-k \nabla T) = \underbrace{q_0}_{\text{fixed outward flux}} + \underbrace{h(T - T_\infty)}_{\text{convective flux}} + \underbrace{\epsilon \sigma_{\mathrm{SB}} (T^4 - T_{\mathrm{amb}}^4)}_{\text{radiation flux}} \tag{4.15}$$

where $\mathbf{n}$ is a normal vector to the boundary, q_0 represents the fixed outward heat flux normal to the boundary (e.g. due to external source or drain), h is the *convective heat-transfer coefficient*, T_∞ the external bulk temperature, ϵ and σ_{SB} the emissivity and Stefan–Boltzmann constant respectively, and T_{amb} the ambient temperature. The bulk temperature T_∞ and the ambient temperature T_{amb} do not necessarily have to be the same. T_∞ is the temperature of the fluid surrounding the object of interest while T_{amb} is the temperature of the enclosure (e.g. room walls or the sky).

The thermal insulation boundary condition is a special case of the fixed heat flux condition where $q_0 = 0$ and no convective or radiation flux is present:

$$\mathbf{n} \cdot (-k \nabla T) = 0 \tag{4.16}$$

giving no heat transfer across that boundary.

Fixed temperature boundary condition, as the name suggests, is simply fixed temperature of a boundary ∂S at a given temperature T_{B}

$$T\big|_{\partial S} = T_{\mathrm{B}}\,. \tag{4.17}$$

For the voltage field, no boundary conditions corresponding to the convection flux and the radiation flux for the temperature field exist. Fixed electric field (or current) flux and fixed voltage boundary conditions however exists, and as for the temperature field the special case of zero flux is called insulation boundary condition.

4.3 Structure and boundary conditions

Many different implementations of the microheaters have been fabricated and used at the University of Iceland and by our collaborators at IBM; three typical examples are shown in Figures 2.1, 2.9a and 4.2. For the FEM simulations, a structure like the one shown in Figure 4.2 was used. It was selected because of its quadrilateral symmetry and overall simplicity. Although it has only two contact lines, the physical properties are expected to be essentially unaltered. The four wire configuration shown in Figures 2.1 and 2.9a is only necessary in practice to measure the current and voltage drop over the microheater, to find the power dissipation. This information can be extracted by other means from the simulation results. Most of the microheaters used recently have been made from platinum on a 100 nm thick silicon dioxide layer on top of a 0.5 mm thick silicon wafer. The same thicknesses were used for most of the simulations.

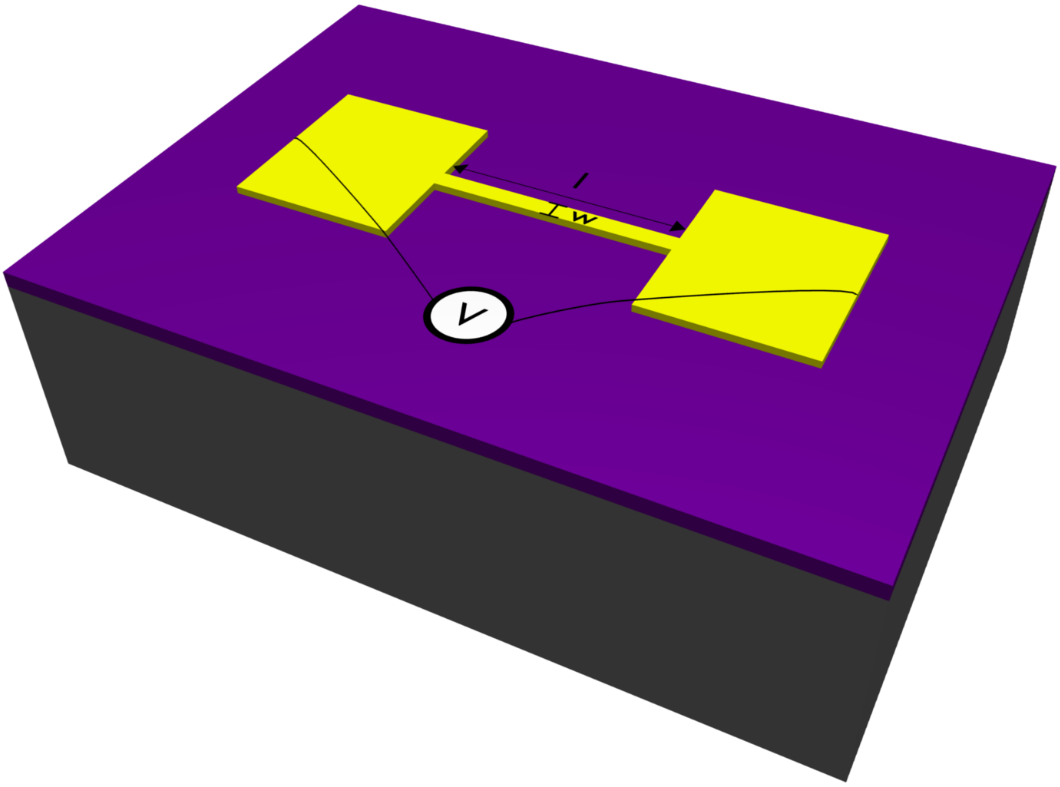

Figure 4.2: A simplified wire structure.

Compared to the heater size the Si/SiO_2 wafer is practically infinite in the lateral directions ($\sim$ 5 cm). Semi-infinite volumes can not be modeled directly in ordinary FEM software, thus we must ensure that the side lengths are long enough not to affect the solution at the area of interest (usually 100 μm - 1 mm, depending on heater size). If the side lengths are chosen long enough the vertical sides can safely be assumed to be at room temperature $T_0 = 300$ K. The finite silicon thickness of 0.5 mm can be modeled directly, and since the backside is usually in good contact with a metallic microstage it can be assumed to be fixed at room temperature. In the simulations the ends of both the right and the left connection pads were held fixed at $V/2$ and $-V/2$, respectively as shown in Figure 4.2.

The energy loss due to radiation can be estimated by the Stefan-Boltzmann law, from Equation 2.15. If we assume that we have a platinum heater ($\epsilon_{\mathrm{Pt}} \approx 0.10$) of length $l = 8$ μm and width $w = 1$ μm at temperature $T = 700$ K, a rough estimate of its radiation energy loss gives

$$\begin{aligned} P_{\mathrm{r}} &\sim A\epsilon_{\mathrm{Pt}}\sigma_{\mathrm{SB}}T^4 && (4.18)\\ &= 1.0\ \mu\mathrm{m} \times 8.0\ \mu\mathrm{m} \times 0.1 \times 5.670 \times 10^{-8}\ \mathrm{J\,s^{-1}m^{-2}K^{-4}} \times (700\ \mathrm{K})^4 && (4.19)\\ &\approx 10\ \mathrm{nW} && (4.20)\end{aligned}$$

which can safely be neglected when compared to the total energy loss of the order of $\sim$ 10 mW, as known from experiments. The convective heat transfer coefficient h_{conv} for a macroscopic plate in air is of the order of $h_{\mathrm{conv}} \sim 10$ W/m^{2}K (Holman 1986), and the external bulk temperature $T_\infty \approx 300$ K. The convective loss can therefore be estimated

$$\begin{aligned} P_{\mathrm{conv}} &\sim Ah_{\mathrm{conv}}(T - T_\infty) = 1.0\ \mu\mathrm{m} \times 8.0\ \mu\mathrm{m} \times 10\ \mathrm{W/m^2K} \times (700 - 300)\ \mathrm{K} && (4.21)\\ &\approx 30\ \mathrm{nW} && (4.22)\end{aligned}$$

also negligible compared to the conductive energy loss, even if h_{conv} would be enhanced substantially due to microscopic effects.

Air is very good thermal insulator with thermal conductivity around one-fiftieth of that of silicon dioxide. By simulations it can be shown that the conductive heat transfer to the atmospheric air is at most of the order of few hundred nW, which can safely be neglected. This leaves the conductive heat transfer through the substrate into the microstage as the dominating heat transfer channel.

By straight forward inspection one can see that the temperature field has to be symmetric about both the long-axis of the heater and the axis perpendicular to the long axis (in the plane of the wafer). The electric potential on the other hand is symmetric about the long-axis and antisymmetric about the axis perpendicular to the long axis. This quadrilateral symmetry allows us to analyze the system by modeling only one-fourth of it, which reduces the analysis run time significantly as well as demands on computer resources. Minimizing the total number of nodes and elements becomes

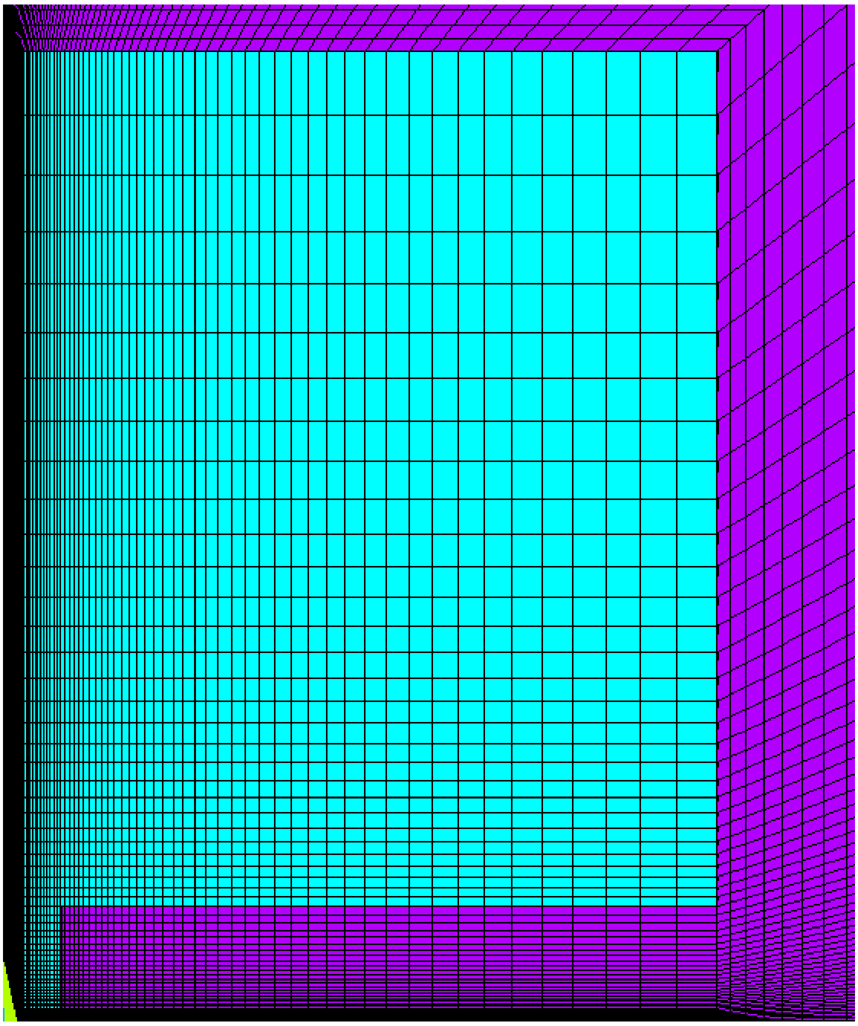

Figure 4.3: An example of the meshing of a simple wire structure. As discussed in the text it is only necessary to model one-fourth of the heater structure due to symmetries.

especially important when modeling three dimensional structures, considering how fast the number of nodes grows and how many elements are needed for detailed studies. For the same reason it is very important to use a high element density close to the heater where the rate of change of the fields is great and low element density farther away. An example of meshing is shown if Figure 4.3, but in real simulations much higher element density is used.

4.4 Material properties

As discussed in section 4.2, the thermal electric analysis requires the knowledge of certain material parameters, such as the thermal conductivity k and electric resistivity ϱ. For accurate simulations the temperature dependence of these parameters must be taken into account. Measurements have demonstrated that both thermal and electric conductivities are altered substantially in thin films compared to their corresponding bulk materials (Yamane et al. 1997, Zhang et al. 2005). This discrepancy between the thin films and the bulk materials is considered to be caused by structural defects, surface scattering and grain boundary scattering, and is usually increased as the film thickness decreases (Zhang et al. 2005).

In ANSYS the temperature dependent material properties may be specified either as polynomial expressions or as tables with discrete values at given temperatures. ANSYS then uses linear interpolation to evaluate the temperature dependent parameters at temperatures not given explicitly in the table. In this section material properties and related assumptions used in the FEM model will be discussed.

4.4.1 Silicon

Silicon is the principal component of most semiconductor devices, and is the most used material in the semiconductor industry. The reason for its extensive use is that it remains a semiconductor at higher temperatures than most other semiconductors, a native oxide is easily grown in a furnace and it is relatively inexpensive. The microheaters are grown on low doped silicon wafers of density $\rho_{\text{Si}} = 2330\ \text{kg/m}^3$ and electric resistivity ϱ_{Si} $10-20\ \Omega\text{cm}$, as given by manufacturer. Due to the high electric resistivity of the insulating silicon dioxide layer ($\varrho_{\text{SiO}_2} = 1.0 \times 10^{14}\ \Omega\text{cm}$) a negligible proportion of the electric field applied to heaters penetrates into the silicon layer. Hence the exact value of the electrical resistivity of the silicon is of little significance, and an average value of $\varrho_{\text{Si}} = 15\ \Omega\text{cm}$ was used.

As discussed in section 4.3 the silicon substrate serves mainly as a heat sink, and hence its thermal conductivity k_{Si} is of great importance. The thermal conductivity has been shown to be practically independent of doping level for $T > 100$ K (Thompson & Younglove 1961), therefore the well known thermal conductivity of intrinsic silicon was used (Efunda 2009). The specific heat at constant pressure C_{Si} is also negligibly affected at low doping level (Zakirov et al. 2003), thus the specific heat of intrinsic silicon was used (COMSOL AB 2007).

All relevant properties of silicon are summarized in Table 4.1, where modified SI units with base length 1 μm are used for convenience.

Table 4.1: Bulk silicon properties.

Property	**Symbol**	**Value**	**Units**	**Reference**
Density	ρ_{Si}	2330×10^{-18}	$\mathrm{kg}/(\mu\mathrm{m})^3$	Shackelford & Alexander (2001)
Electrical resistivity	ϱ_{Si}	1.5×10^{-7}	$\mathrm{T}\Omega\mu\mathrm{m}$	
Thermal conductivity	k_{Si}			Efunda (2009)
- at 300 K		148×10^{6}	$\mathrm{pW}/(\mu\mathrm{m} \times \mathrm{K})$	
- at 350 K		119×10^{6}	$\mathrm{pW}/(\mu\mathrm{m} \times \mathrm{K})$	
- at 400 K		98.9×10^{6}	$\mathrm{pW}/(\mu\mathrm{m} \times \mathrm{K})$	
- at 500 K		76.2×10^{6}	$\mathrm{pW}/(\mu\mathrm{m} \times \mathrm{K})$	
- at 600 K		61.9×10^{6}	$\mathrm{pW}/(\mu\mathrm{m} \times \mathrm{K})$	
- at 800 K		42.2×10^{6}	$\mathrm{pW}/(\mu\mathrm{m} \times \mathrm{K})$	
- at 1000 K		31.2×10^{6}	$\mathrm{pW}/(\mu\mathrm{m} \times \mathrm{K})$	
Specific heat	C_{Si}			COMSOL AB (2007)
- at 300 K		714.1×10^{12}	$\mathrm{pJ}/(\mathrm{kg} \times \mathrm{K})$	
- at 400 K		791.5×10^{12}	$\mathrm{pJ}/(\mathrm{kg} \times \mathrm{K})$	
- at 500 K		835.7×10^{12}	$\mathrm{pJ}/(\mathrm{kg} \times \mathrm{K})$	
- at 600 K		861.8×10^{12}	$\mathrm{pJ}/(\mathrm{kg} \times \mathrm{K})$	
- at 700 K		880.0×10^{12}	$\mathrm{pJ}/(\mathrm{kg} \times \mathrm{K})$	
- at 800 K		896.4×10^{12}	$\mathrm{pJ}/(\mathrm{kg} \times \mathrm{K})$	
- at 900 K		912.1×10^{12}	$\mathrm{pJ}/(\mathrm{kg} \times \mathrm{K})$	

4.4.2 Silicon dioxide

The thin layer of silicon dioxide serves as a thermal and electric insulator. Many of its properties are strongly dependent on fabrication methods, and its density can vary from $2000 - 2300\ \mathrm{kg/m^3}$ (Shackelford & Alexander 2001). However, essentially all deposited and thermally grown oxides in semiconductor processing are amorphous, hence density of $\rho_{\mathrm{O}} = 2200\ \mathrm{kg/m^3}$ (Petersen 1978) and specific heat C_{O} for the amorphous phase (COMSOL AB 2007) was used. Its electrical resistivity ϱ_{O} also varies widely, but in all cases it is many orders of magnitude larger than that of silicon or the metal film. Thus its exact numerical value is of little significance and we chose $\varrho_{\mathrm{O}} = 1.0 \times 10^{16}\ \Omega\mathrm{m}$.

The thermal conductivity of the silicon dioxide layer is probably the single most important parameter in the model presented. Measurements have shown that the normal-to-plane thermal conductivity $k_{\mathrm{O}\perp}$ of amorphous silicon dioxide decreases with decreasing film thickness, and the effect can be significant for films under $\sim 1\ \mu\mathrm{m}$ thickness (Kato & Hatta 2005). However, no satisfying measurements have been done on the in-plane thermal conductivity $k_{\mathrm{O}\parallel}$ of thin films, hence the bulk thermal conductivies shown in Table 4.2 were used for $k_{\mathrm{O}\parallel}$. Plenty of measurements have been done on the normal-

Table 4.2: Amorphous bulk silicon dioxide properties.

Property	Symbol	Value	Units	Reference
Density	ρ_{O}	2200×10^{-18}	$\mathrm{kg}/(\mu\mathrm{m})^3$	Petersen (1978)
Electrical resistivity	ϱ_{O}	1.0×10^{10}	$\mathrm{T}\Omega \times \mu\mathrm{m}$	Shackelford & Alexander (2001)
Thermal conductivity	k_{O}			Shackelford & Alexander (2001)
- at 300 K		1.36×10^6	$\mathrm{pW}/(\mu\mathrm{m} \times \mathrm{K})$	
- at 350 K		1.43×10^6	$\mathrm{pW}/(\mu\mathrm{m} \times \mathrm{K})$	
- at 400 K		1.50×10^6	$\mathrm{pW}/(\mu\mathrm{m} \times \mathrm{K})$	
- at 500 K		1.62×10^6	$\mathrm{pW}/(\mu\mathrm{m} \times \mathrm{K})$	
- at 600 K		1.72×10^6	$\mathrm{pW}/(\mu\mathrm{m} \times \mathrm{K})$	
- at 700 K		1.80×10^6	$\mathrm{pW}/(\mu\mathrm{m} \times \mathrm{K})$	
- at 1000 K		1.85×10^6	$\mathrm{pW}/(\mu\mathrm{m} \times \mathrm{K})$	
Specific heat	C_{O}			COMSOL AB (2007)
- at 300 K		716.3×10^{12}	$\mathrm{pJ}/(\mathrm{kg} \times \mathrm{K})$	
- at 400 K		864.9×10^{12}	$\mathrm{pJ}/(\mathrm{kg} \times \mathrm{K})$	
- at 500 K		965.4×10^{12}	$\mathrm{pJ}/(\mathrm{kg} \times \mathrm{K})$	
- at 600 K		1031.9×10^{12}	$\mathrm{pJ}/(\mathrm{kg} \times \mathrm{K})$	
- at 700 K		1081.3×10^{12}	$\mathrm{pJ}/(\mathrm{kg} \times \mathrm{K})$	
- at 800 K		1124.4×10^{12}	$\mathrm{pJ}/(\mathrm{kg} \times \mathrm{K})$	
- at 900 K		1158.4×10^{12}	$\mathrm{pJ}/(\mathrm{kg} \times \mathrm{K})$	

to-plane thermal conductivity $k_{\mathrm{O}\perp}$ at room temperature (Kato & Hatta 2005) and its behavior is well known as a function of film thickness as shown in Table 4.3. Its temperature dependence on the other hand is not well known when the film thickness decreases, and to the best of our knowledge no satisfactory measurements exist. We simply assume $k_{\mathrm{O}\perp}$ has the same temperature dependence as its bulk counterpart, and scale the bulk thermal conductivity linearly by comparing its value at room temperature in Table 4.3 to that of bulk in Table 4.2 (e.g. for 100 nm film we multiply the bulk thermal conductivity with 1.10/1.36 for all temperatures). To estimate $k_{\mathrm{O}\perp}$ for film thicknesses not explicitly stated in Table 4.3 a linear interpolation is used.

4.4.3 Platinum

As discussed in section 4.3 most of the microheaters are made of platinum, thus its properties are of central importance. We use the density $\rho_{\mathrm{Pt}} = 2144$ kg/m^3 of bulk platinum, and due to lack of data for the specific heat C_{Pt} of thin films we chose to use

Table 4.3: The dependence of the silicon dioxide normal-to-plane thermal conductivity $k_{\mathrm{O}\perp}$ on film thickness (Kato & Hatta 2005).

Thickness	**Thermal conductivity $k_{\mathrm{O}\perp}$**
500 nm	1.18×10^6 pW/(μm × K)
200 nm	1.14×10^6 pW/(μm × K)
100 nm	1.10×10^6 pW/(μm × K)
50 nm	1.03×10^6 pW/(μm × K)

that of bulk platinum, shown in Table 4.4.

The resistivity of platinum depends strongly on fabrication methods and film thickness. The resistivity of a 50 nm thick sputter deposited platinum film has been measured both at the University of Iceland and by our collaborators at IBM to be

$$\varrho_{\mathrm{Pt@300\ K}} = (3.0 \pm 1.0) \times 10^{-7}\ \Omega\mathrm{m} \tag{4.23}$$

compared to 1.0×10^{-7} Ωm for bulk platinum; so the resistivity is tripled for such a thin film. Further the thermal coefficient of resistance α_{Pt} of the thin film was measured

$$\alpha_{\mathrm{Pt}} = (0.0020 \pm 0.0001)\ \mathrm{K}^{-1}\,, \tag{4.24}$$

or half that of bulk platinum $\alpha_{\mathrm{Pt,bulk}} = 0.0039\ \mathrm{K}^{-1}$ (Serway 1998). In all the simulations a platinum thickness of 50 nm is used, hence the above values of $\varrho_{\mathrm{Pt@300\ K}}$ and α_{Pt} are used with Equation 2.4 to find the resistivity ϱ_{Pt} as a function of temperature. The result is shown in Table 4.5.

Table 4.4: Platinum bulk properties.

Property	**Symbol**	**Value**	**Units**	**Reference**
Density	ρ_{Pt}	2144×10^{-18}	kg/(μm)^3	Shackelford & Alexander (2001)
Specific heat	C_{Pt}			Platinum metals review (2007)
- at 300 K		132.2×10^{12}	pJ/(kg × K)	
- at 400 K		135.1×10^{12}	pJ/(kg × K)	
- at 500 K		138.0×10^{12}	pJ/(kg × K)	
- at 600 K		140.9×10^{12}	pJ/(kg × K)	
- at 700 K		143.8×10^{12}	pJ/(kg × K)	
- at 800 K		146.7×10^{12}	pJ/(kg × K)	
- at 900 K		149.6×10^{12}	pJ/(kg × K)	

The *Wiedemann–Franz law* states that for metals at not too low temperatures ($T \gtrsim \Theta$; where Θ is the Debye temperature) the ratio of the thermal conductivity k to the electrical conductivity $\sigma = 1/\varrho$ is directly proportional to the temperature

$$\frac{k}{\sigma} = k \times \varrho = \mathcal{L} \times T \tag{4.25}$$

Table 4.5: Platinum electrical resistivity and thermal conductivity.

Property	Symbol	Value	Units	Reference
Electrical resistivity	ϱ_{Pt}			
- at 300 K		3.0×10^{-13}	$\mathrm{T\Omega} \times \mu\mathrm{m}$	
- at 400 K		3.6×10^{-13}	$\mathrm{T\Omega} \times \mu\mathrm{m}$	
- at 500 K		4.2×10^{-13}	$\mathrm{T\Omega} \times \mu\mathrm{m}$	
- at 600 K		4.8×10^{-13}	$\mathrm{T\Omega} \times \mu\mathrm{m}$	
- at 700 K		5.4×10^{-13}	$\mathrm{T\Omega} \times \mu\mathrm{m}$	
- at 800 K		6.0×10^{-13}	$\mathrm{T\Omega} \times \mu\mathrm{m}$	
- at 900 K		6.6×10^{-13}	$\mathrm{T\Omega} \times \mu\mathrm{m}$	
- at 1000 K		7.2×10^{-13}	$\mathrm{T\Omega} \times \mu\mathrm{m}$	
Thermal conductivity	k_{Pt}			
- at 300 K		50.0×10^{6}	$\mathrm{pW}/(\mu\mathrm{m} \times \mathrm{K})$	
- at 400 K		55.6×10^{6}	$\mathrm{pW}/(\mu\mathrm{m} \times \mathrm{K})$	
- at 500 K		59.5×10^{6}	$\mathrm{pW}/(\mu\mathrm{m} \times \mathrm{K})$	
- at 600 K		62.5×10^{6}	$\mathrm{pW}/(\mu\mathrm{m} \times \mathrm{K})$	
- at 700 K		64.8×10^{6}	$\mathrm{pW}/(\mu\mathrm{m} \times \mathrm{K})$	
- at 800 K		66.6×10^{6}	$\mathrm{pW}/(\mu\mathrm{m} \times \mathrm{K})$	
- at 900 K		68.2×10^{6}	$\mathrm{pW}/(\mu\mathrm{m} \times \mathrm{K})$	
- at 1000 K		69.4×10^{6}	$\mathrm{pW}/(\mu\mathrm{m} \times \mathrm{K})$	

where the proportionality constant $\mathcal{L}$ is called the Lorenz number. It has been demonstrated that the Wiedemann–Franz law holds for thin metal films, albeit the Lorentz number $\mathcal{L}$ is altered compared to the bulk value (Choi et al. 2006). The Lorentz number has been measured

$$\mathcal{L} \approx 5.0 \times 10^{-8}\ \mathrm{W\Omega/K^2} \tag{4.26}$$

for a 50 nm thick platinum film (Zhang et al. 2004, 2005), compared to $\mathcal{L}_{\mathrm{bulk}} \approx 2.6 \times 10^{-8}\ \mathrm{W\Omega/K^2}$ for bulk material. The Lorentz number $\mathcal{L}$ and the film resistivity ϱ_{Pt} were used to predict the temperature behavior of the thermal conductivity using Equation 4.25, the result is given in Table 4.5.

4.5 Temperature-power relation

By solving Equation 4.12 and Equation 4.14 simultaneously using the material properties for silicon, silicon dioxide and platinum discussed in subsections 4.4.1, 4.4.2 and 4.4.3 respectively, one can solve for both spatial and temporal thermal electric behaviour of the system. The steady-state solutions are found using the *static analysis* type in ANSYS, and the time-dependent properties using the *transient analysis* type.

The thermal electric properties were found for microheaters grown on top of $d_{\mathrm{O}} =$

100 nm thick oxide layer and of fixed length $l = 8$ μm and thickness $d = 50$ nm, but varying width w from 200 nm to 8 μm. The wire geometries in the numerical models correspond to the heaters studied experimentally in Yat-Yin Au et al. (2008) discussed in section 2.5.

By solving the system of equations for each geometry using different voltage boundary conditions one can find the voltage drop over the heater V_h, the current that passes through it I_h and the temperature in the microheater center T. This is done for few different voltage boundary conditions and then the *piecewise cubic hermite interpolating polynomial* (PCHIP) interpolation algorithm is used to interpolate for the intermediate values.

Plotting the voltage drop V_h as a function of the current I_h for each heater width w gives the result in Figure 4.4. The points shown in the figure are the values from the simulations, and the continuous lines are obtained by interpolation between the points. The general I_h-V_h behavior, a near-constant slope at low I_h which increases when I_h increases (and hence T increases), resembles the behavior shown in experiments, although direct comparison is difficult due to varying measured resistivity of platinum ϱ_Pt as discussed in subsection 4.4.3.

In the same simulations the temperature T in the microheater center is recorded, and by computing the power dissipated in the heater using Equation 2.1 and plotting the temperature T as a function of the dissipated power P_h results in Figure 4.5. We see that a essentially linear P_h-T relation is observed for each heater width w. This result supports the assumption that ΔT is linearly related to the power dissipation P_h as discussed in section 2.1.

The slopes of the curves in Figure 4.5 give the inverse of the thermal impedance Z_th

$$\frac{1}{Z_\mathrm{th}} = \frac{dP_\mathrm{h}}{dT} \tag{4.27}$$

discussed in section 2.1. Figure 4.6 shows inverse thermal impedance $1/Z_\mathrm{th}$ plotted as a function of heater width for the fixed heater length $l = 8$ μm. As expected $1/Z_\mathrm{th}$ increases as the heater width increases, although the slope reduces with heater width. This decrease in the slope is probably due to propertionally lower heat flow in the lateral direction in the silicon dioxide layer.

If the same process is performed for heaters of fixed width $w = 300$ nm but varying length l from 0.4 μm to 15 μm Figure 4.7 is obtained. For heaters of length l above ~ 5 μm the inverse thermal impedance $1/Z_\mathrm{th}$ increases linearly with heater length l as shown by the blue linear fitting curve. However, as the heater length l decreases the relative “heat leakage” into the well thermally conducting contact pads increases , hence the slope of the curve decreases.

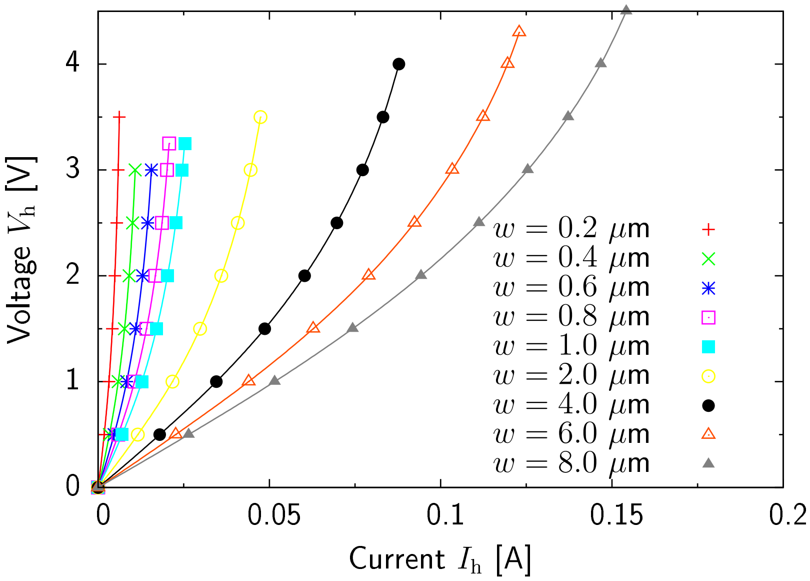

Figure 4.4: Voltage V_h as a function of the current I_h for heaters of length $l = 8\ \mu$m and width w from 200 nm to 8 μm.

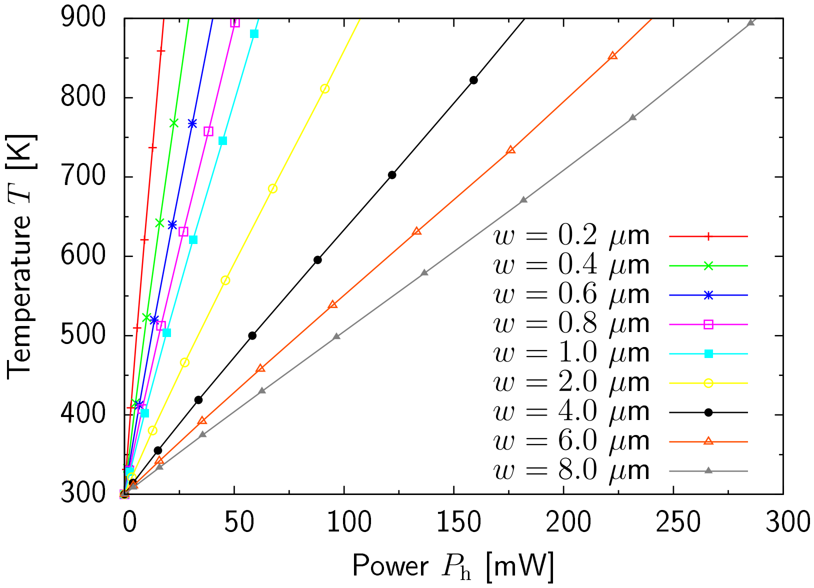

Figure 4.5: Temperature of the microheater center T as a function of power dissipated P_h for heaters of length $l = 8\ \mu$m and varying width w from 200 nm to 8 μm.

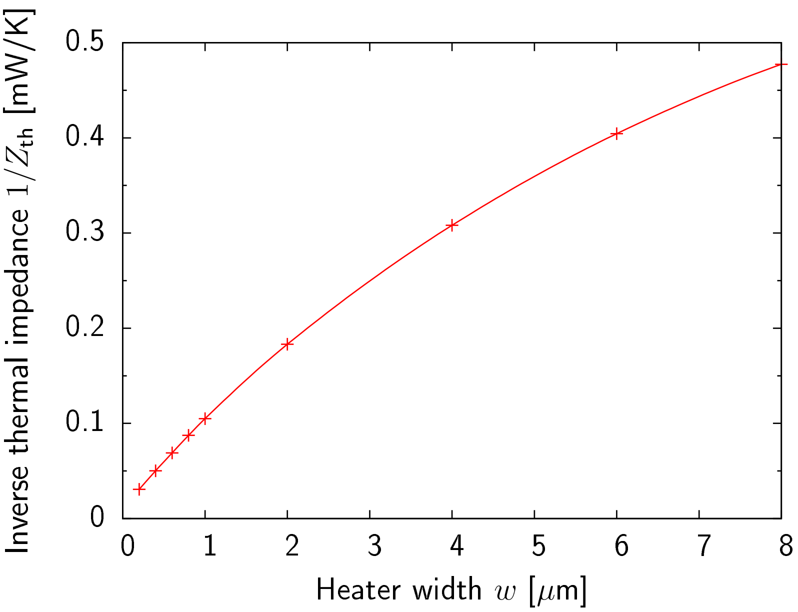

Figure 4.6: Inverse thermal impedance $1/Z_{\text{th}}$ as a function of heater width w for heaters of fixed length $l = 8\ \mu$m and width w from 200 nm to $8\ \mu$m.

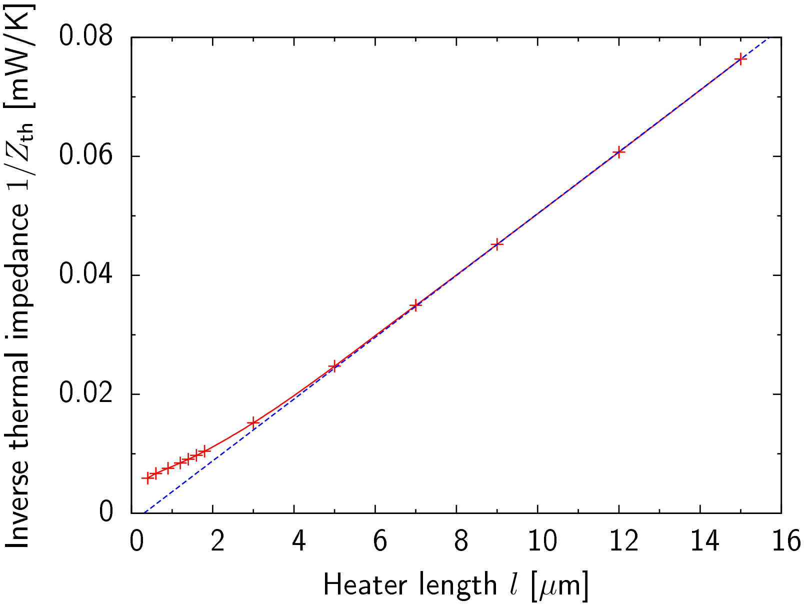

Figure 4.7: Inverse thermal impedance $1/Z_{\text{th}}$ as a function of heater length l for heaters of fixed width $w = 300$ nm and length l from $0.4\ \mu$m to $15\ \mu$m.

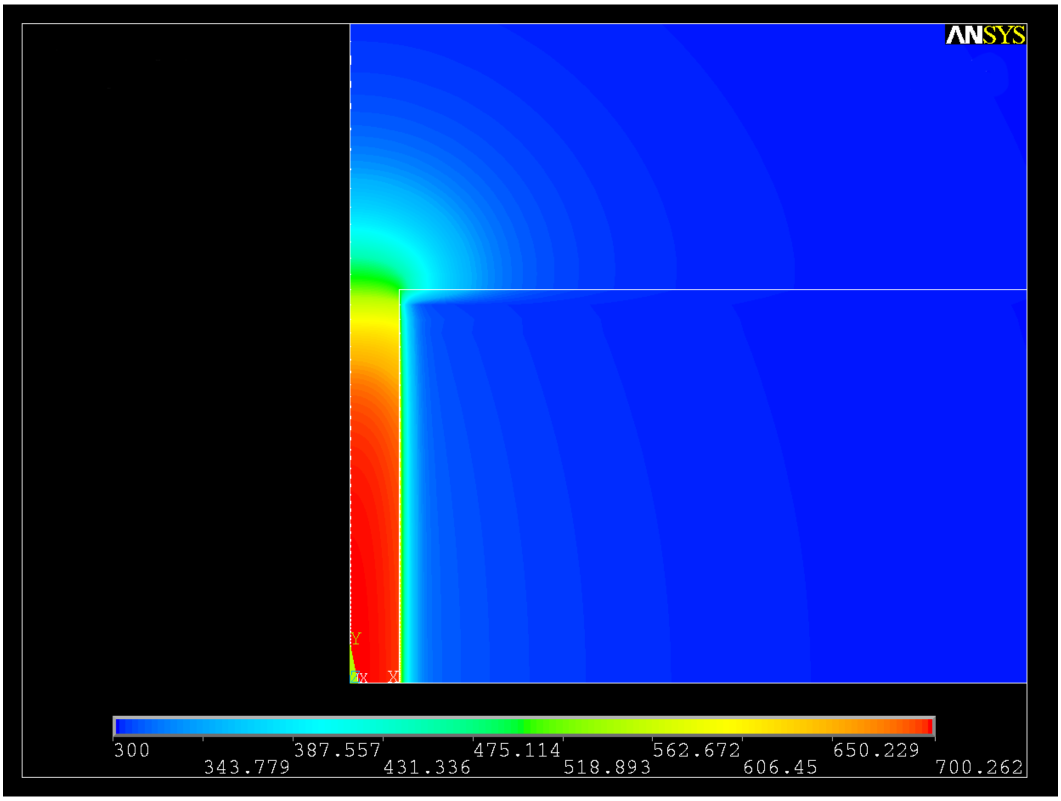

Figure 4.8: The temperature distribution of a heater of length $l = 8$ μm and width $w = 1$ μm

4.6 Temperature distributions

Using the voltage-temperature relation obtained in the simulations discussed above one can interpolate (using PCHIP) and find the voltage boundary condition that gives 700 K microheater center temperature T. Repeating the calculations using the interpolated voltage boundary condition gives us the temperature distributions around wires fixed at $T = 700.0$ K (within 0.1%).

By plotting the temperature in the plane of the substrate along the axis perpendicular to heater long axis Figure 4.9 is obtained. The solid lines show the temperature along the (Pt/Air)-silicon dioxide interface and the dashed lines the temperature along the silicon dioxide-silicon interface.

The steep temperature gradients indicate that the temperature distributions are very localized around the heaters. For the narrow wires $w \lesssim 2$ μm the temperature of the substrate does not exceed 350 K, however as the heater width increases the surface temperature increases and for the wider heaters $w \gtrsim 6$ μm the surface temperature exceeds 400 K.

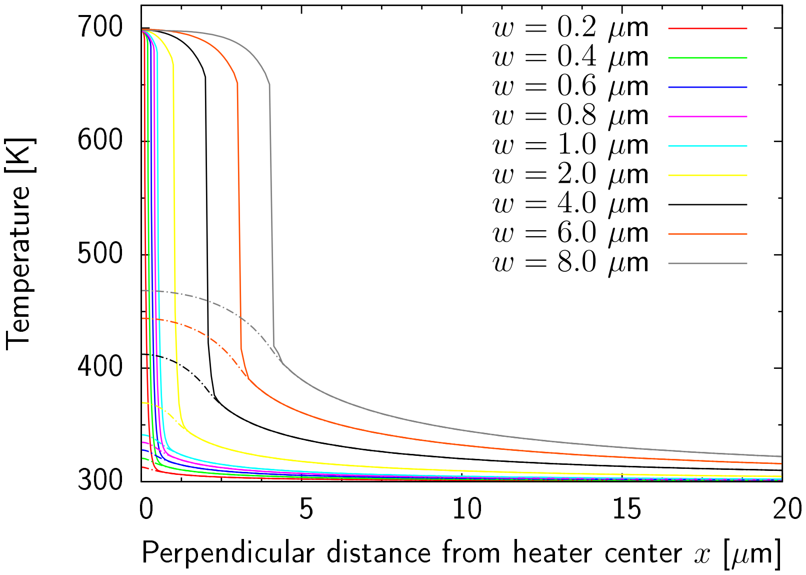

Figure 4.9: Temperature along the axis perpendicular to the long axis for heaters of fixed length $l = 8$ μm and varying width w held at fixed temperature $T = 700$ K.

Using the temperature distributions obtained one can estimate the proportional radiation contribution of the silicon substrate when the heater radiation is measured in our FTIR system. The optical system can be focused on the heater so that the field of view gets a circular shape of diameter $\sim l$ with the heater in the middle. With respect to Figure 4.9 we see that the silicon close to the heater is at ~ 380 K is radiating as of platinum at 700 K for the widest heater of $w = 8.0$ μm. We scale the contribution with respect to the visible surface areas A_{Pt} and A_{Si} and assume that the substrate underneath the heater is shielded and is therefore neglected. We use that the emission constant of platinum is around $\epsilon_{\mathrm{Pt}} \approx 0.1$ (Deemyad & Silvera 2008) and that of silicon around $\epsilon_{\mathrm{Si}} \approx 0.05$ (for 300 K $< T <$ 500 K) in the 1800 cm^{-1} – 6000 cm^{-1} region. By applying Stefan-Boltzmanns law in Equation 2.15 one gets

$$\varsigma_{1800+} \equiv \frac{I_{\mathrm{Si}}}{I_{\mathrm{Pt}}} \times \frac{A_{\mathrm{Si}}}{A_{\mathrm{Pt}}} \approx \frac{0.05 \times 380^4}{0.1 \times 700^4} \times 0.57 \approx 0.03 \tag{4.28}$$

where I_{Si} and I_{Pt} are the radiation intensities for silicon and platinum respectively. This gives $\sim 3\%$ contribution from the substrate in the 1800 cm^{-1} – 6000 cm^{-1} region.

In the 600 cm^{-1} – 1800 cm^{-1} region however the emission of silicon increases up to $\epsilon_{\mathrm{Si}} \approx 0.35$ while the platinum emission is nearly unchanged $\epsilon_{\mathrm{Pt}} \approx 0.1$. An estimate with the same assumptions then gives

$$\varsigma_{1800-} \equiv \frac{I_{\mathrm{Si}}}{I_{\mathrm{Pt}}} \times \frac{A_{\mathrm{Si}}}{A_{\mathrm{Pt}}} \approx \frac{0.35 \times 380^4}{0.1 \times 700^4} \times 0.57 \approx 0.17 \tag{4.29}$$

suggests a stronger substrate radiation of $\sim 17\%$ in the 600 cm^{-1} – 1800 cm^{-1} region.

These ratios are increased even further for more narrow heaters where more substrate is radiating at lower temperatures. For $w = 1.0$ μm ratios of $\varsigma_{1800+} \approx 0.1$ and $\varsigma_{1800-} \approx 0.7$ were obtained, and for $w = 0.2$ μm ratios of $\varsigma_{1800+} \approx 0.6$ and $\varsigma_{1800-} \approx 4$ were obtained. This is yet another manifestation of the dominating substrate radiation in the 600 $\text{cm}^{-1} - 1800$ cm^{-1} range encountered for the arrays discussed in chapter 3, and as address there this suggests that the silicon/silicon dioxide substrate is not well suited for optical heater applications in this wavenumber range. In the 1800 $\text{cm}^{-1} - 6000$ cm^{-1} range however the silicon/silicon dioxide substrate is acceptable for most purposes.

Outside the heater area the temperature is practically identical above and below the silicon dioxide layer. Below the heater however, a large temperature drop is observed through the silicon dioxide layer. The temperature drop decreases with the heater width, such that more of the silicon substrate is heated. This is seen more clearly in Figure 4.10, where the temperature is plotted along the line through the heater and into the silicon/silicon dioxide substrate. We see the temperature in the silicon substrate in the main figure, and in the inset a zoom in of the platinum layer ($-0.05 - 0.00$ μm) and the silicon dioxide layer ($0.00 - 0.10$ μm). Due to the large contrast between the thermal conductance of the platinum and silicon dioxide layers, $k_{\text{Pt}} \gg k_{\text{O}}$, practically uniform temperature $T = 700$ K is observed through the platinum layer. For the narrower heaters $w \lesssim 2$ μm almost all the temperature drop takes place through the silicon dioxide layer, but as the heater width increases, more and more of the temperature drop occurs in the silicon substrate. Even though the temperature drop in the silicon layer is significant, it drops below 301.0 K at around 100 μm for even the widest heater $w = 8$ μm, indicating that the fixed temperature boundary condition at the bottom of the silicon substrate (thickness 0.5 mm = 500 μm) is far enough away, not to affect the solution at the area of interest.

In Figure 4.11 the temperature is plotted along the heater long axis at the platinum-silicon dioxide interface. The solution should however also apply to the platinum top surface, but as we saw in Figure 4.10 the temperature is more or less the same at each side of the platinum layer. We see that the heating of the contact pads is significant, both because of heat leakage from the heater constriction into the pads and because of heating due to higher current density in the pad close to the connection. The heating increases with the width of the heater, and for the wider ones, $w \gtrsim 6$ μm, the contact pads are heated up by more than 100 K close to the connection (within ~ 10 μm). The heating of the contact pads, as shown in Figure 4.8 could result in a substantial unpolarized thermal radiation contribution from the contact pads, especially if the experimental system is not highly focused on the heater area.

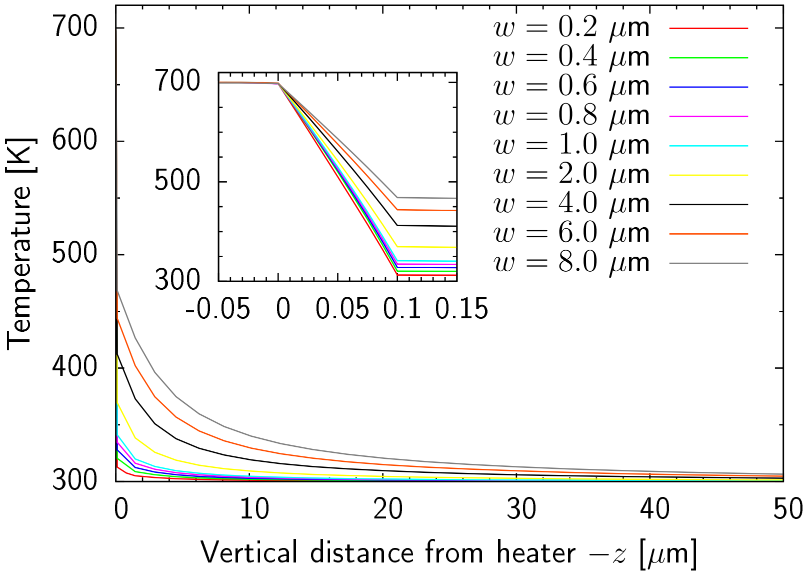

Figure 4.10: Temperature through the center and into the substrate for heaters of fixed length $l = 8$ μm and varying width w held at fixed temperature $T = 700$ K.

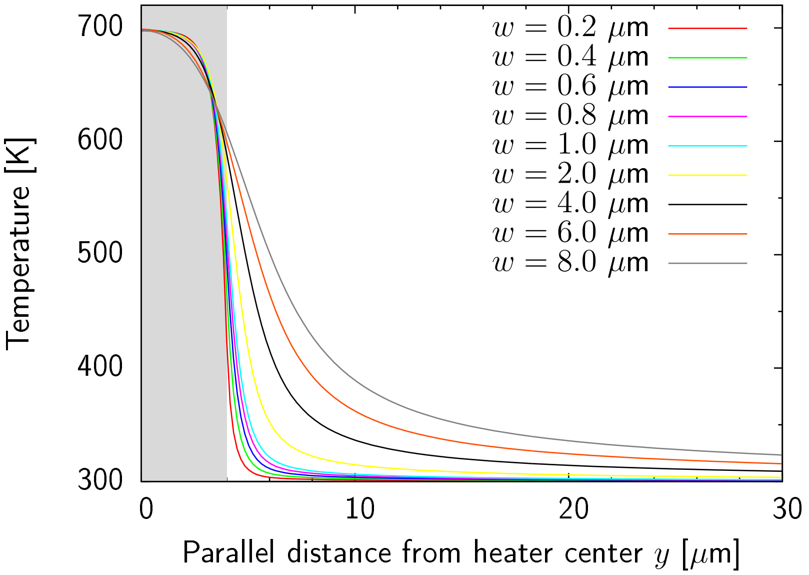

Figure 4.11: Temperature along the long axis of heaters of fixed length $l = 8$ μm and varying width w held at fixed temperature $T = 700$ K. The shaded area represents the extent of the heaters, starting from their center.

4.7 Effect of the metallic layer properties

As discussed in section 2.1 it has been shown that for most metals the resistivity increases linearly with temperature T as described by

$$\varrho = \varrho_0(1 + \alpha \Delta T) \tag{4.30}$$

where ϱ_0 is the resistivity at room temperature T_0, α is the thermal coefficient of resistance (TCR) and $\Delta T = T - T_0$ (Young & Freedman 2007).

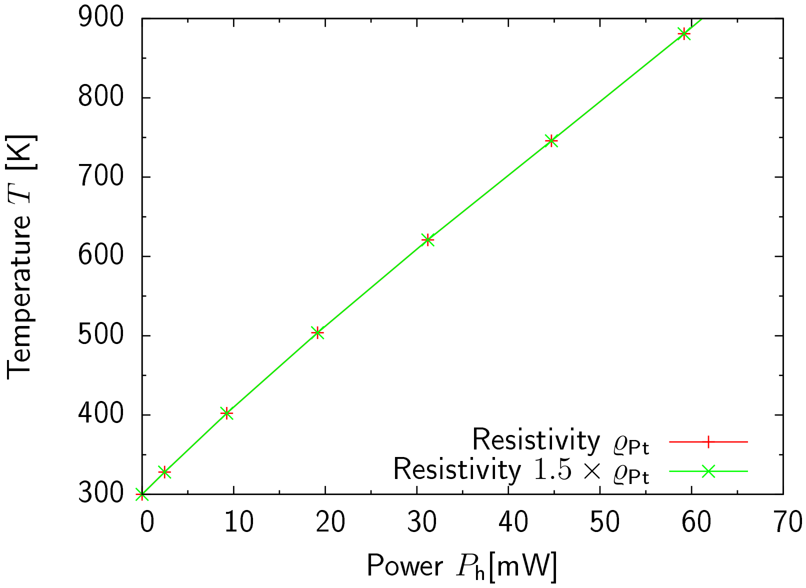

Figure 4.12: Temperature of the microheater center T as a function of power dissipation P_h for normal platinum resistivity ϱ_Pt and increased by 50% $1.5 \times \varrho_\mathrm{Pt}$.

By linearly increasing the platinum resistivity ϱ_Pt by 50%, that is multiplying the resistivity by 1.5 independently of temperature T, and carrying out the simulations, Figure 4.12 is obtained. It shows, as expected, that linear scaling of the resistivity does not change the temperature-power relation, and the two lines overlap almost completely. This is reasonable since linear scaling of the resistivity will not alter the Joule heating density, only the current-voltage relation (increasing ϱ decreases the current I_h and increases V_h such that $P_\mathrm{h} = I_\mathrm{h} \times V_\mathrm{h}$ will be unchanged).

However by scaling the thermal coefficient of resistance α_Pt by 50% and keeping ϱ_0 unchanged the Joule heating density will be altered. Proportionally more energy will be produced where the temperature is high compared to the unscaled case, that is in the center of the heater. Nevertheless the temperature-power relation is barely altered as shown in Figure 4.13. Only a small decrease of less than 0.5% in the temperature T is observed at $P_\mathrm{h} \sim 50$ mW ($T \sim 900$ K).

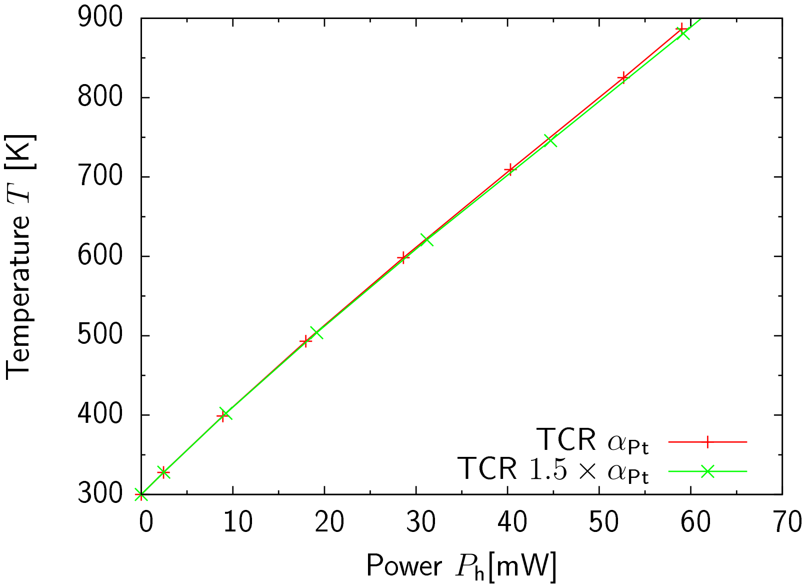

Figure 4.13: Temperature of the microheater center T as a function of power dissipation P_h for normal platinum TCR α_Pt and increased by 50% $1.5 \times \alpha_\mathrm{Pt}$.

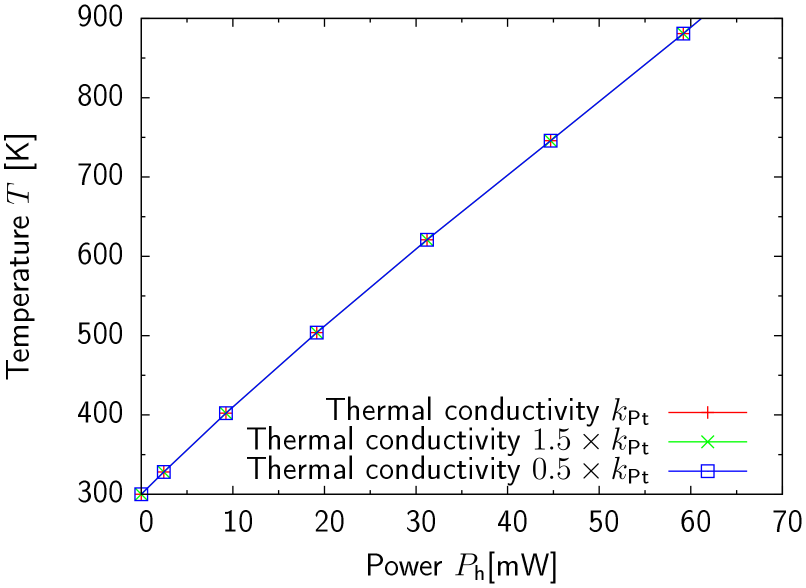

Figure 4.14: Temperature of the microheater center T as a function of power dissipation P_h for normal platinum thermal conductivity k_Pt and scaled by $\pm 50\%$.

Figure 4.14 also shows that scaling the platinum thermal conductivity k_{Pt} by ±50% also reproduces the same temperature-power relation as for the unscaled case, as shown in Figure 4.14. This suggests that majority of the heat produced in the heater is transported directly into the substrate through the silicon dioxide layer without spreading much around in the platinum layer. If this was not the case increasing the platinum thermal conductivity k_{Pt} would increase the heat flow into the contact pads and consequently lower the heater temperature for a given power P_{h}.

We have seen from figures 4.12 and 4.13 that the magnitude and temperature dependence of the heater resistivity is unimportant for the temperature-power relation, and Figure 4.14 shows the same for the thermal conductivity. The suggest that the temperature regulation mechanism discussed in section 2.1 is reliable despite changes in the structural properties of the metal due to annealing and electromigration.

From this we also deduce that these simulations are roughly valid for any type of metal used in the heater as long as the thermal conductivity of the heater is much higher than that of the oxide ($k_{\mathrm{heater}} \gg k_{\mathrm{O}}$) which is valid for most metals.

4.8 Effect of the silicon dioxide layer thickness

In section 4.6 we saw that most of the temperature drop occurs over the thin silicon dioxide layer, and in section 4.7 that the properties of the metal have no great impact on the thermal properties of the structure. This makes the silicon dioxide layer the single most important layer of the structure. As discussed in subsection 4.4.2 the normal-to-plane thermal conductivity $k_{\mathrm{O}\perp}$ depends on the layer thickness. By using the values given in Table 4.3 and interpolate for the intermediate values, one can investigate with the FEM model how the thermal properties of the heater change with the silicon dioxide layer thickness d_{O}.

In Figure 4.15 we see the temperature of the microheater center, T, as a function of dissipated power P_{h}, for heater of length $l = 8\ \mu\mathrm{m}$ and width $w = 1\ \mu\mathrm{m}$ but varying silicon dioxide thickness d_{O} from 50 nm to 500 nm. A linear relationship is observed as before, and apparently much lower power dissipation is needed when a thick ($d_{\mathrm{O}} \sim 500$ nm) silicon dioxide layer is used. This is seen more clearly in Figure 4.16 where the inverse thermal impedance (Equation 4.27) is plotted as a function of d_{O}. By assuming that the radiation power P_{r} from a heater at a given temperature is independent of silicon dioxide thickness we see that the *radiation efficiency*

$$\xi_{\mathrm{r}} \equiv \frac{P_{\mathrm{r}}}{P_{\mathrm{h}}} \tag{4.31}$$

of the device can be increased by a factor of ~ 3 by using $d_{\mathrm{O}} = 500$ nm instead of $d_{\mathrm{O}} = 100$ nm.

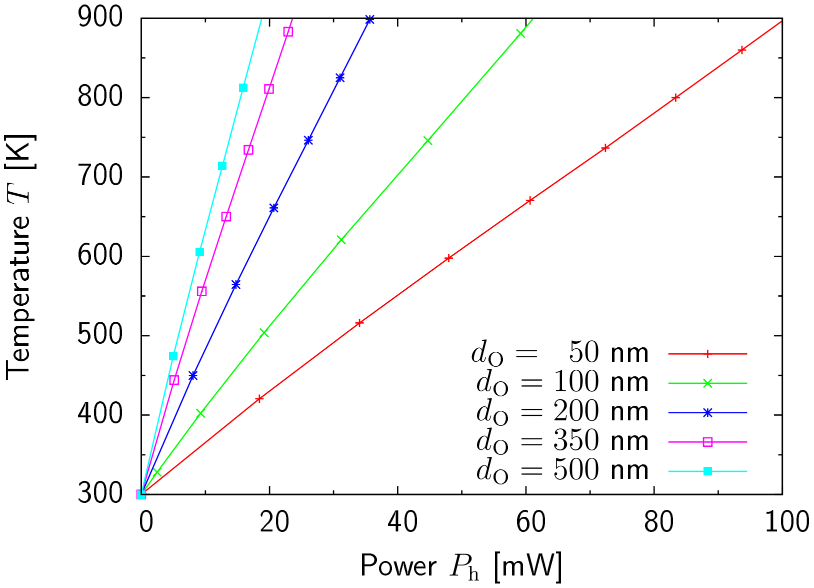

Figure 4.15: The temperature of the microheater center T as a function of power dissipation P_h for varying silicon dioxide layer thickness d_O ($l = 8$ μm and $w = 8$ μm).

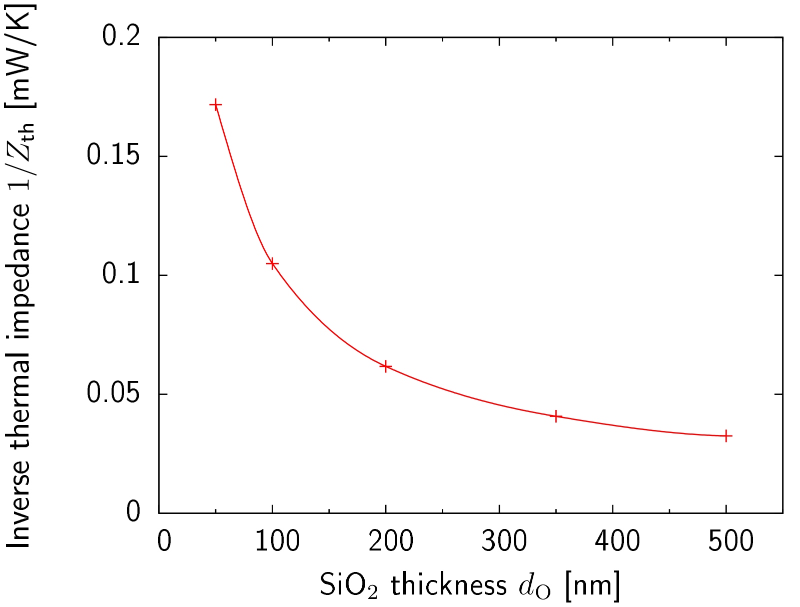

Figure 4.16: Inverse thermal impedance $1/Z_{th}$ as a function of silicon dioxide thickness d_O.

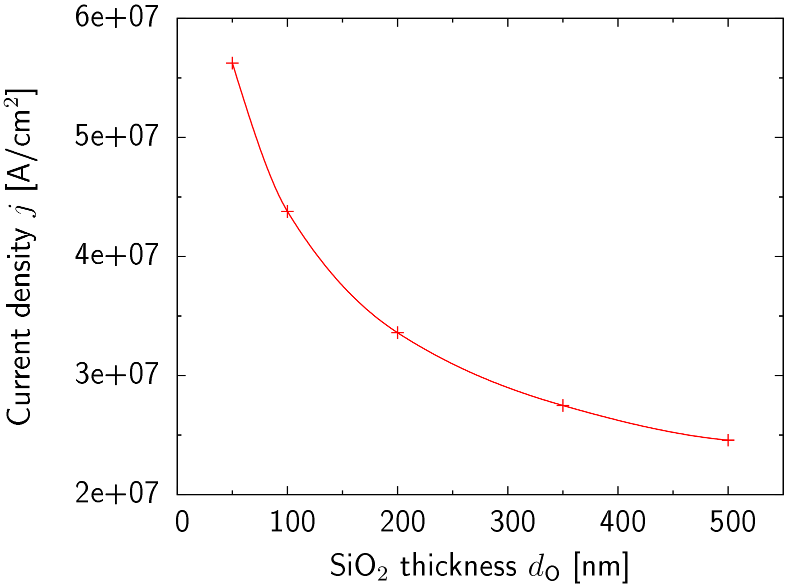

Figure 4.17: Current density j at temperature $T = 700$ K as a function of silicon dioxide thickness d_O.

This increased radiation efficiency however comes at a price; increasing the silicon dioxide thickness will bring interference with the light reflected at the silicon-silicon dioxide interface closer to our measurement regime. To estimate the position $\tilde{\nu}_\mathrm{if}$ of the first interference peak we can use the well known relation

$$\tilde{\nu}_\mathrm{if} = \frac{1}{4d_\mathrm{O}} \tag{4.32}$$

for interference in thin films (Young & Freedman 2007). The results for the different oxide thicknesses are shown in Table 4.6. These values imply that we can safely use oxide thickness up to 350 nm without getting significant interference in the 600 cm^{-1} – 5000 cm^{-1} wavenumber region. However for $d_\mathrm{O} = 500$ nm we expect the first interference peak to overlap with our measurement regime.

In Figure 4.17 the current density j in a heater of length $l = 8$ μm and width $w = 1$ μm held at $T = 700$ K is plotted as a function of silicon dioxide thickness d_O. A current

Table 4.6: The position of the first interference peak $\tilde{\nu}_\mathrm{if}$ for few oxide thicknesses d_O.

Oxide thickness d_O	Interference peak position $\tilde{\nu}_\mathrm{if}$
50 nm	50000 cm^{-1}
100 nm	25000 cm^{-1}
200 nm	12500 cm^{-1}
350 nm	7150 cm^{-1}
500 nm	5000 cm^{-1}

density j of more than 1×10^7 A/cm^2 is observed, indicating that even though platinum is relatively resistant to electromigration (high melting temperature), the significance of electromigration is substantial (becomes significant at $10^5 - 10^7$ A/cm^2 for most metals as discussed in section 2.1). The *mean time to failure* of a metallic wire due to electromigration can be estimated by an empirical model developed by J.R. Black at the end of the 1960s:

$$\tau_{\mathrm{failure}} = \frac{\mathcal{A}}{j^2} e^{\frac{E_{\mathrm{a}}}{k_{\mathrm{B}} T}} \tag{4.33}$$

where $\mathcal{A}$ is a constant depending on the cross-sectional area and E_{a} is the activation energy (Black 1969). We see from Figure 4.17 that by using silicon dioxide thickness $d_{\mathrm{O}} = 500$ nm instead of $d_{\mathrm{O}} = 100$ nm, we can decrease the current density needed to obtain the same temperature T by factor ~ 2, resulting in lifetime increase of factor ~ 4 according to Equation 4.33.

The lifetime of Joule heated microwires will probably always be limited by electromigration, due to the high current density. There are however a few conceivable ways to reduce the effect of the electromigration, and consequently increase the lifetime of the device. Firstly, a thicker silicon dioxide layer could be used as discussed above. Since the power temperature relation is essentially independent of the type of metal used a more electrically resistive one with high IR emissivity, such as some nichrome ($\mathrm{Ni}_x\mathrm{Cr}_y$) alloy could be used to decrease the current needed ($P_{\mathrm{h}} \propto j^2 \varrho$), the effect on the optical properties is however not clear. A thicker metallic layer could be used to distribute the power dissipation over larger volume (not very efficient since $P_{\mathrm{h}} \propto j^2$). Last but not least it has been shown that using bidirectional current stress (e.g. square wave voltage) can increase the lifetime of devices encountering electromigration substantially. A power regulation system using bidirectional current was designed, and is discussed in details in chapter 5.

The temperature distribution is also affected by the thickness of the silicon dioxide d_{O} as shown in Figures 4.18, 4.19 and 4.20. In Figure 4.18 we see that the temperature distribution perpendicular to the long axis of heaters becomes more and more smeared out as d_{O} increases. As expected a larger temperature drop over the silicon dioxide layer is observed as its thickness d_{O} increases, as seen more clearly in Figure 4.19. Due to the increased temperature drop over the silicon dioxide layer, not as much of the silicon substrate is heated up, probably resulting in shorter response time (see section 4.9). In Figure 4.20 we see that the temperature along the long axis of heaters drops slightly more close to the contact pads for the thicker silicon dioxide layers, but the heating of the contact pads is essentially unaltered.

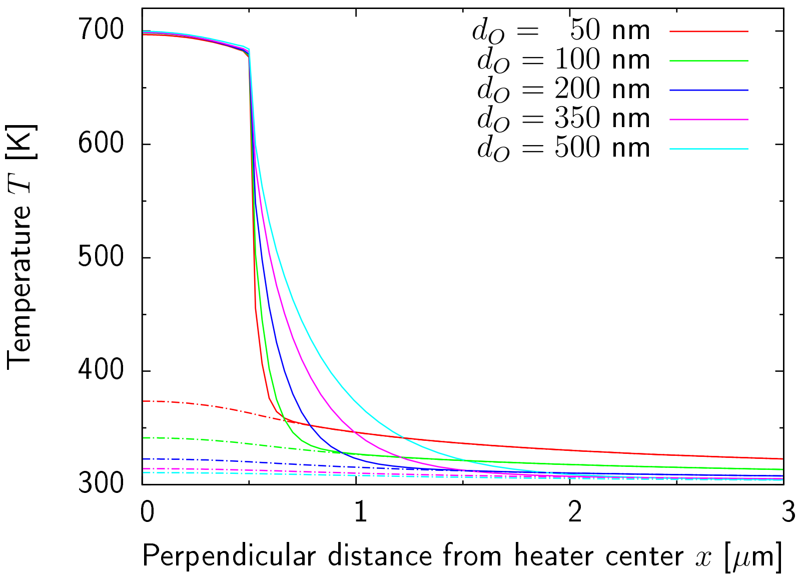

Figure 4.18: Temperature along the axis perpendicular to the long axis of heaters at $T = 700$ K on varying silicon dioxide thickness d_O ($l = 8$ μm, $w = 1$ μm).

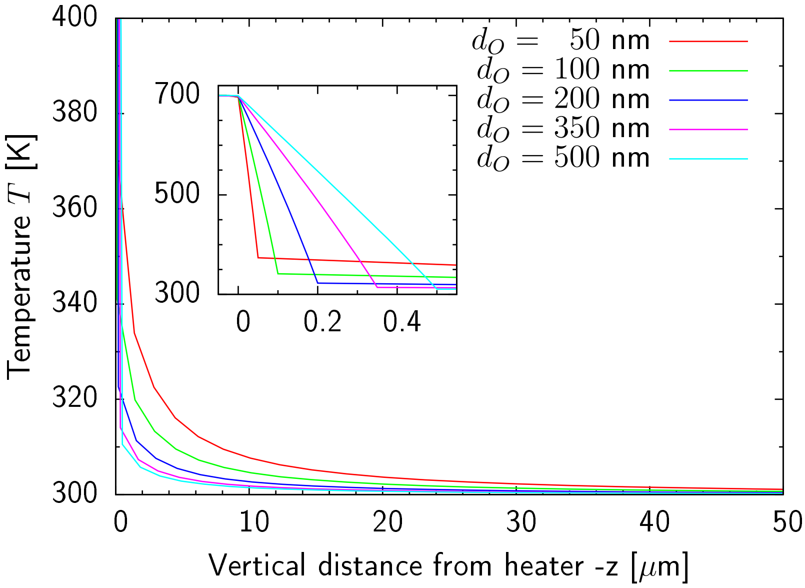

Figure 4.19: Temperature through the center and into the substrate of heaters at $T = 700$ K on varying silicon dioxide thickness d_O ($l = 8$ μm, $w = 1$ μm).

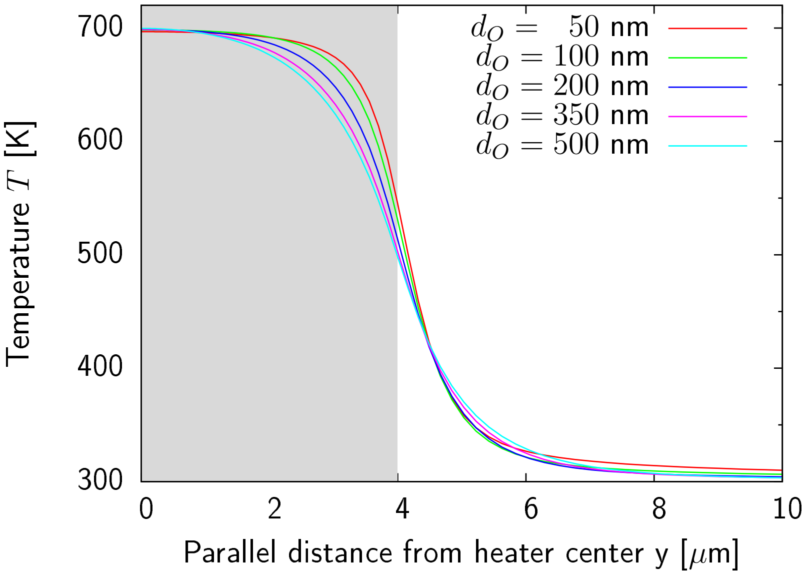

Figure 4.20: Temperature along the long axis of heaters at $T = 700$ K on varying silicon dioxide thickness ($l = 8$ μm, $w = 1$ μm). The shaded area presents the extent of the heaters.

4.9 Thermal response time

Equations 4.12 and 4.14 can be solved in time with appropriate material properties and boundary conditions using the transient analysis type in ANSYS. By applying a bias voltage V at time $t = 0.0$ ns that results in a steady-state temperature of $T_\infty = 700$ K at room temperature $T_0 = 300.0$ K the heat up process can be investigated. Heaters of fixed length $l = 8$ μm and varying width w from 200 nm to 8 μm, all grown on a $d_\mathrm{O} = 100$ nm thick silicon dioxide were simulated. The result is shown in Figure 4.21, where the center temperature T is plotted as function of time t. We notice that the time it takes the heater to reach $T = 650$ K increases with the heater width w, due to more substrate heating.

By defining the thermal response time $\tau_{\tilde{T}}$ as the time it takes the heater to reach a given temperature $\tilde{T}$ when starting at $T = 300$ K we can plot $\tau_{600\ \mathrm{K}}$ and $\tau_{650\ \mathrm{K}}$ as a function of heater width w, resulting in Figure 4.22. A short response time $\tau_{650\ \mathrm{K}}$ between 10 ns and 20 ns is observed for the narrower heaters $w \lesssim 2$ μm, however for the wider heaters $w \gtrsim 2$ μm it blows up and for $w = 8$ μm a response time of $\tau_{650\ \mathrm{K}} = 250$ ns is observed. This is in accordance to Figure 4.10 where we saw that for $w \gtrsim 2$ μm the substrate heating starts to increase rapidly.

This short response time for the narrower wires indicates that they could be useful for electro-optical applications where short light pulses are needed, but as discussed in

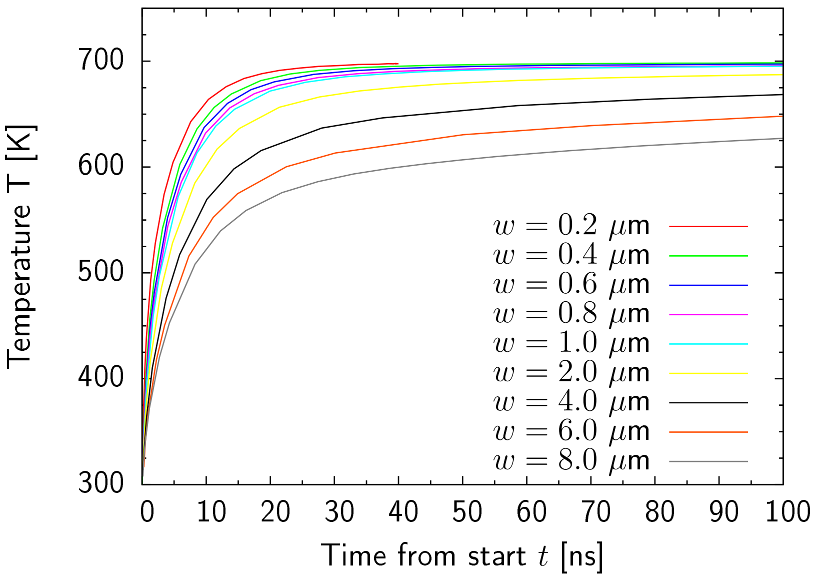

Figure 4.21: Temperature in the heater center T as a function of time t for heaters of fixed length $l = 8$ μm and varying width w from 200 nm to 8 μm.

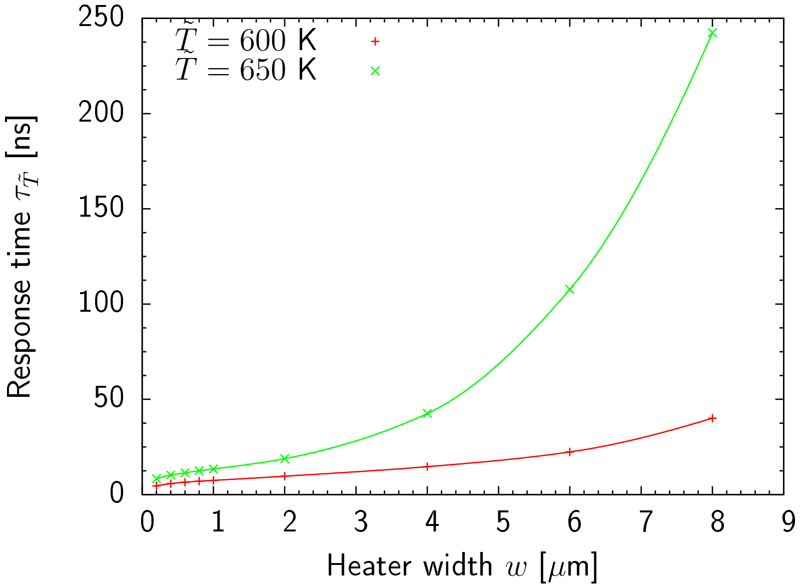

Figure 4.22: Thermal response times $\tau_{600\ \mathrm{K}}$ and $\tau_{650\ \mathrm{K}}$ as a function of heater width w for fixed heater length $l = 8$ μm.

section 4.8 the lifetime of the heaters is seriously limited by electromigration, rendering them unsuitable as a continuous light sources. Pulsed infrared light sources however have variety of applications, such as in digital media writing/reading, fluorescence spectroscopy and biochemical analysis.

4.10 Single layer cadmium selenide substrate

One of the materials suggested as a substrate material in chapter 3 was cadmium selenide (CdSe), which has low transmissivity in the 600 cm^{-1}–5000 cm^{-1} (2.0–17 μm) range. Its thermal conductivity k_{CdSe} has been shown to follow the relation

$$k_{\mathrm{CdSe}}(T) = 13.5613 - 0.02680393 \times T + 1.86478 \times 10^{-5} \times T^2 \qquad (4.34)$$

in the 300 – 700 K range (Capper 1994), shown in Figure 4.23. Its electrical resistivity can go as low as $\varrho_{\mathrm{CdSe}} \approx 1.0$ Ωm, although it is highly dependent on dopant concentration.

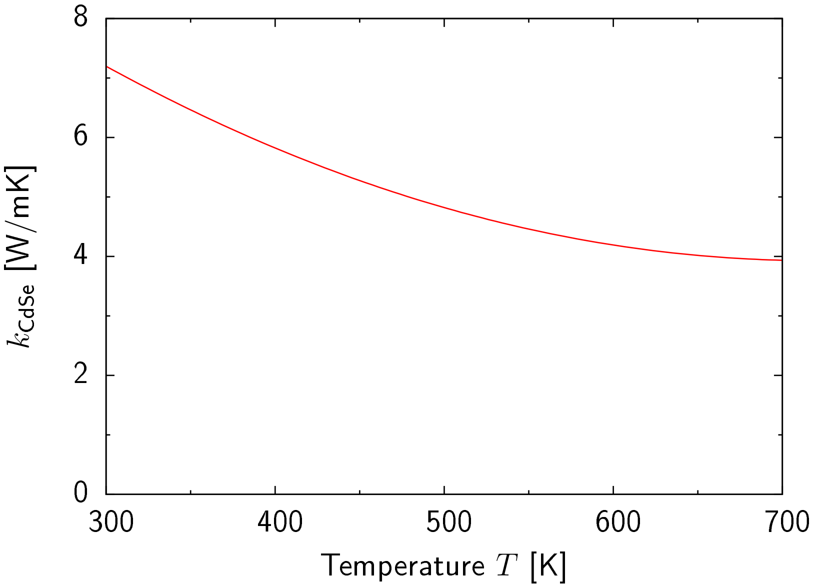

Figure 4.23: Thermal conductivity k_{CdSe} of cadmium selenide as a function of temperature T.

By using a single layer cadmium selenide substrate instead of the double layer silion-silicon dioxide the temperature-power relation for a platinum heater of width $w = 1.0$ μm and length $l = 8.0$ μm in Figure 4.24 was obtained. For comparison the temperature-power curves for the silicon-silicon dioxide substrate is shown for two different oxide thicknesses, $d_{\mathrm{O}} = 200$ nm and $d_{\mathrm{O}} = 350$ nm. It shows that using a single layer cadmium selenide gives a nonlinear temperature-power relation and relatively high

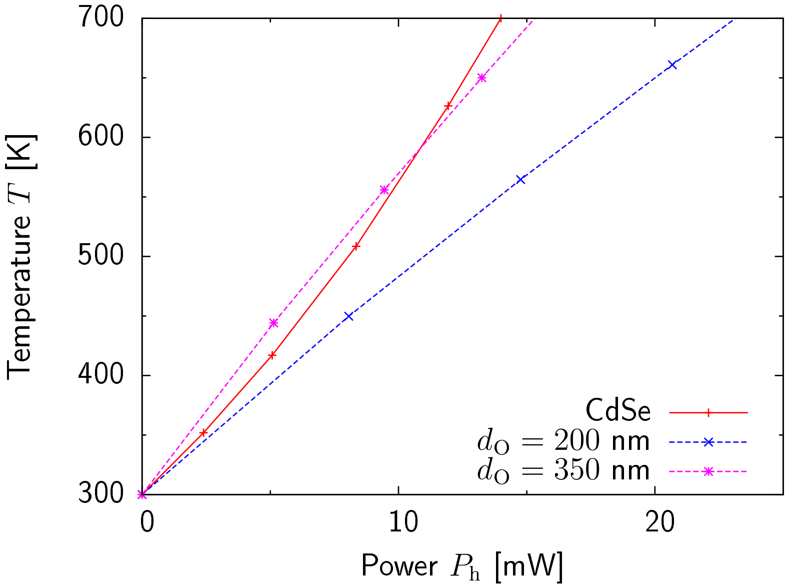

Figure 4.24: The temperature of the microheater center T as a function of power dissipation P_h for two silicon dioxide layer thicknesses and a cadmium selenide substrate.

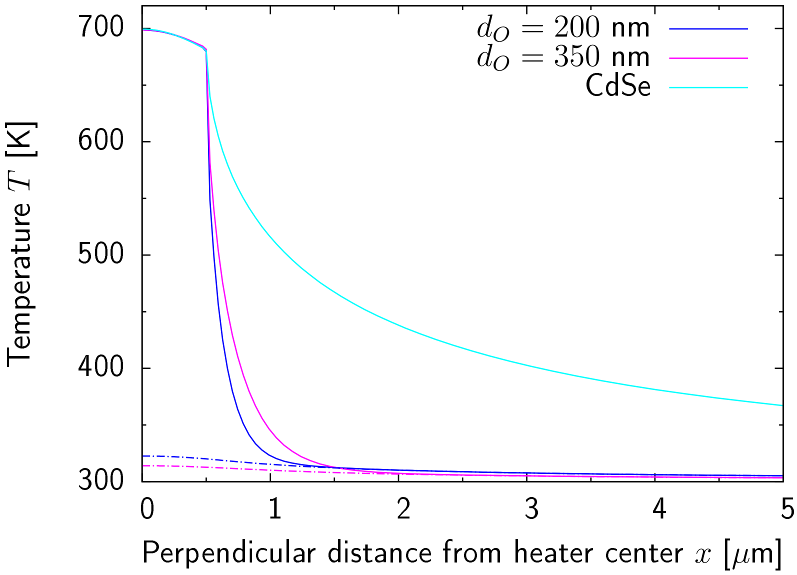

Figure 4.25: Temperature along the axis perpendicular to the long axis of heaters at $T = 700$ K for two silicon dioxide layer thicknesses and a cadmium selenide substrate.

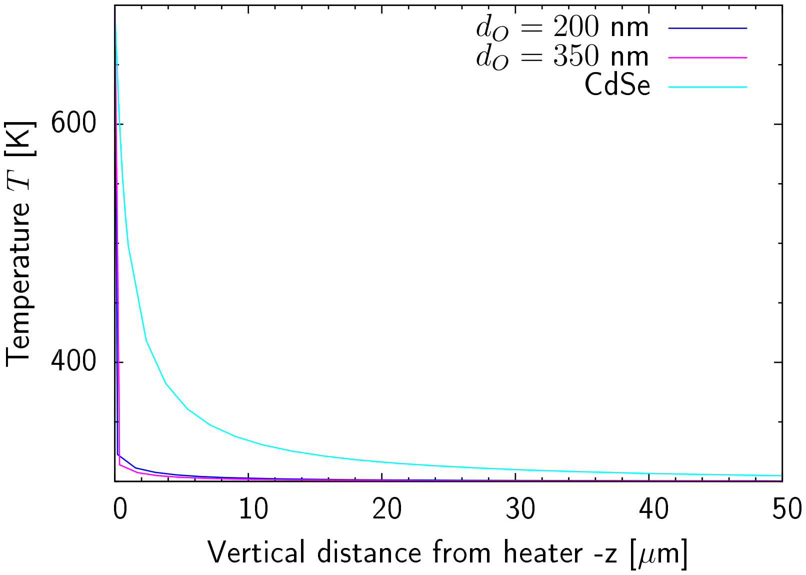

Figure 4.26: Temperature through the center and into the substrate of heaters at $T = 700$ K for two silicon dioxide layer thicknesses and a cadmium selenide substrate.

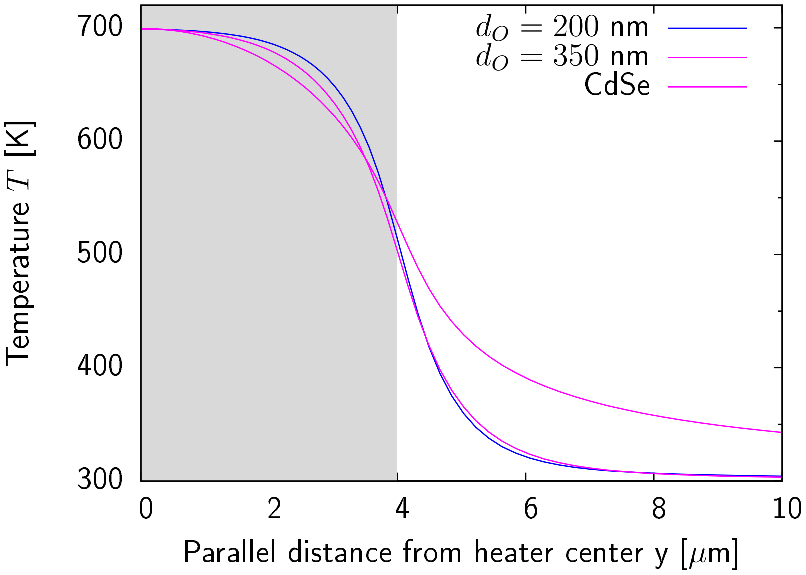

Figure 4.27: Temperature along the long axis of heaters at $T = 700$ K for two silicon dioxide layer thicknesses and a cadmium selenide substrate. The shaded area presents the extent of the heaters.

temperature for a given power. However by looking at the temperature distribution shown in Figures 4.25, 4.26 and 4.27 we see that the it is very smeared out in all directions. This will lead to increased unpolarized radiation from the contact pads and a longer thermal response time. Crystaline sodium chloride (NaCl) has a similar thermal conductivity as the CdSe and will therefore show similar behavior. However, due to the low emissivity of these material they might still be useful as heater substrates, especially in the 600 cm^{-1} – 5000 cm^{-1} (2.0 – 17 μm) range where the silicon-silicon dioxide substrate is disadvantageous, as discussed in chapter 3.

From this we deduce that to be able to get a localized temperature distribution without getting a strong substrate radiation a double layer structure must be used. A substrate material with high thermal conductivity and a thin thermally and electrically insulating film on top must be used, preferably both with low emissivity in the wavenumber range of interest.

5 Power Regulator

In the last decades the importance of electromigration has increased drastically as the size of electronic devices has scaled down deeper into the submicron region. At the same time its effect on reliability of electronic devices has been studied extensively both by the industry and academia. The lifetime τ_{failure} has been shown to decrease as the current density j and temperature T increase, as described by Black's Equation 4.33 (Black 1969). Further it has been shown experimentally that the lifetime τ_{failure} can be increased by using bidirectional current stress (e.g. square wave), and is shown to increase with its frequency f (Liew et al. 1990, Tao et al. 1993). The lifetime increase by using a bidirectional current can be significant, e.g. Al-2% Si interconnects under current density of 1.5×10^7 A/cm^2 at room temperature were found to last for $\sim$ 1 minute under DC current load compared to $\sim$ 100 hours under AC current load at frequency $f = 1.0$ kHz (Tao et al. 1995). This *healing effect* is caused by a reversed mass transport as the polarity is changed.

The heating in the microheaters should be independent of current direction, and should therefore be unaltered by using AC square-wave current instead of DC. Since no satisfying commercial AC power regulation system was found to exist, we designed our own to extend the lifetime of the platinum heaters. In Figure 5.1 an electronic circuit that controls the voltage V_{h} applied over a microheater of resistance R_{h} and measures the current I_{h} is shown.

The circuit is a combination of two *push-pull transistor amplifiers* (using C557B PNP and C547B NPN transistors), both connected to an external power source giving $V_+ = 15$ V and $V_- = -15$ V. The resistances $R_{\mathrm{P}} = 1.0$ kΩ at the gates of the transistors are simply to protect the transistors from static currents and transients. The output current from the amplifiers is controlled by two operational amplifiers (TL071CP) that are also connected to the same external power source. The principle of a four-wire measurement is exploited by connecting the inverting inputs (-) to the sensing pads of the heater, and the current pads to the output of the amplifiers. This way the effect of the contact resistances R_{C1}, R_{C2}, R_{C3} and R_{C4} will be eliminated due to negligible current passing through the inverting inputs. This gives a voltage drop

$$V_{\mathrm{h}} = V_{\mathrm{in}} \tag{5.1}$$

over the heater. A known current sensing resistance R_{S} is placed between the heater and the lower amplifier and the voltage drop V_{S} over it measured. From the measured

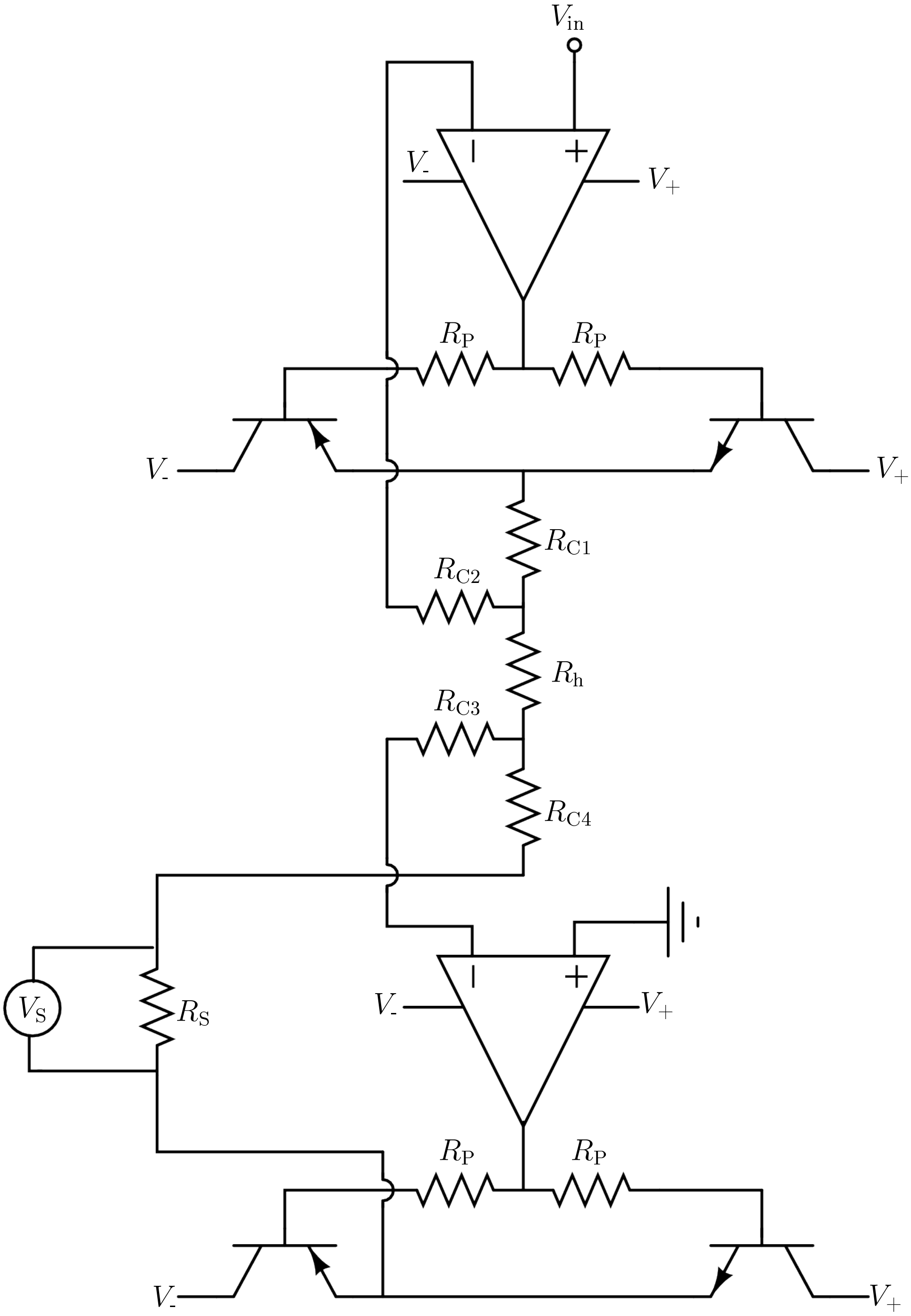
V_{in}
V_-
V_+
R_{P}
R_{P}
V_-
V_+
R_{C1}
R_{C2}
R_{h}
R_{C3}
R_{C4}
V_{S}
R_{S}
V_-
V_+
R_{P}
R_{P}
V_-
V_+

Figure 5.1: An electronic circuit that controls the voltage V_{h} applied over a microheater of resistance R_{h} while measuring the current I_{h}.

voltage V_S one can calculate the current passing through the heater

$$I_\mathrm{h} = \frac{V_\mathrm{S}}{R_\mathrm{S}} \tag{5.2}$$

The voltage drop over the sensing resistance can be no larger than $\sim$ 14.3 V due to the base-emitter voltage drop over the transistors. The sensing resistance R_S must be selected with this in mind, such that $|V_S| < 14.3$ V but large enough for V_S to be measured accurately. Preferably a power resistance is used to minimize changes in R_S as a function of current I_h.

This kind of a circuit was able to follow an input voltage square wave of frequency up to $f = 20$ kHz. It may easily be optimized for higher frequencies by selecting electronic components designed especially for higher frequencies.

By using a computer controlled DAQ-board to control V_in and measure V_s one can calculate and control the power dissipation in the microheater ($P_\mathrm{h} = V_\mathrm{in} \times I_\mathrm{h}$) at a frequency f_r while changing the polarity at a much higher frequency $f \gg f_\mathrm{r}$. This way the polarity of the heater can be changed at a high frequency despite relatively low power regulation frequency $f_\mathrm{r} \sim 10 - 100$ Hz.

The use of the presented power regulation system has not yet been proven to extend the lifetime of the platinum heaters. However, based on the effect of high frequency bi-directional current stress on the lifetime of various other metalization systems in the literature we expect to see an increase in their lifetime, which could increase the practical significance of the heaters substantially.

6 Summary and conclusion

In chapter 3 the thermal radiation from platinum microheater arrays was investigated. It was observed that from a platinum heater array with ten heaters ($l = 50$ μm and $w = 0.6$ μm) the contribution from the silicon/silicon dioxide substrate was significant. From ~ 500 cm^{-1} to ~ 1700 cm^{-1} it dominated the contribution from the heater array, and up to ~ 3000 cm^{-1} non-negligible substrate contribution is expected. Two different ways to decrease the substrate radiation were suggested. Firstly other substrate materials with desirable thermal and optical properties can be used e.g. cadmium selenide (CdSe) or crystalline sodium chloride (NaCl). Secondly suspended heaters without any direct contact to the substrate could be fabricated to reduce the heating of the substrate.

To investigate among other things the heating of the substrate for single heaters, a thermal electric analysis was performed using the finite element technique. The heater temperature T was found to be practically linearly related to the electrical power dissipation P_{h}. Further it was found that changing the electrical resistivity ϱ or thermal conductivity k of the metal film barely alters the temperature-power relation. This suggests that the assumption used for the experiments that ΔT is linearly related to the power dissipation P_{h} is valid despite the effect of annealing and electromigration on the properties of the metal film.

The temperature distribution in plane of the heaters was found to be very localized, especially for the narrow heaters $w \lesssim 2$ μm where the substrate temperature at each side did not exceed 350 K when the heaters were kept at $T = 700$ K. For the wider heaters $w \gtrsim 6$ μm the surface temperature however exceeds 400 K. From the obtained temperature distributions a rough estimate of the radiation contribution of the silicon-silicon dioxide substrate was performed. It implies that its contribution can not be neglected, especially not for wavenumbers $\tilde{\nu}$ under 1800 cm^{-1}, where it dominates the heater radiation for narrower heaters $w \lesssim 1$ μm.

The temperature was found to be uniform throughout the metal film, and most of the temperature drop happened through the silicon dioxide layer. For the narrow heaters $w \lesssim 2$ μm the heating of the contact pads was negligible, but for the wider heaters $w \gtrsim 6$ μm the contact pads are heated up by more than 100 K close to the connection (within ~ 10 μm) which could result in a substantial unpolarized thermal radiation contribution from the contact pads.

For a heater of length $l = 8$ μm and width $w = 1$ μm it was shown that by using an oxide thickness $d_\mathrm{O} = 500$ nm instead of $d_\mathrm{O} = 100$ nm the ratio between the radiation power and the electric power could be increased by a factor of ~ 3. It would also lower the required current density by a factor of ~ 2 resulting in a lifetime increase of factor ~ 4 according to Black's equation. The temperature distribution however gets somewhat more smeared out when thicker silicon dioxide layer is used, possibly causing more substrate radiation contribution. Using thicker silicon dioxide will also bring interference with the light reflected at the silicon-silicon dioxide interface closer to our measurement regime, which could overlap with our typical measurement regime for $d_\mathrm{O} > 350$ nm.

Another method discussed to increase the heater lifetime is to use high frequency bidirectional current to decrease the effect of electromigration. It has been shown for various interconnects to increase the lifetime by orders of magnitude. A power regulation system that exploits this effects and is able to run at a frequency up to $f \sim 20$ kHz was designed as discussed in chapter 5.

The lifetime of the heaters, if driven by a DC current will probably always be limited by electromigration, due to the high current density needed $j \gtrsim 1 \times 10^7$ A/cm^2. This renders them unsuitable as continuous light sources, but they could still be practical for pulsed optical applications where short light pulses are needed. Time dependent finite element analysis gave a thermal response time of the order of tens of nanoseconds for the narrower heaters. This suggests that they could be useful where short infrared pulses at frequency lower than ~ 10 MHz are needed.

Analysis of a heater structure with a single layer cadmium selenide substrate shows that the temperature distribution gets very smeared out, resulting in an increased unpolarized radiation from the contact pads and a longer thermal response time. Crystalline sodium chloride (NaCl) has a similar thermal conductivity as the CdSe therefore we expect it to behave similarly. However, due to the low emissivity of these materials they might still be useful as heater substrates, especially in the 600 cm^{-1} – 5000 cm^{-1} (2.0 – 17 μm) range. From this we deduce that to be able to get a localized temperature distribution without getting a strong substrate radiation a double layer structure with a strong thermal conductivity contrast must be used.

Bibliography

Alda, J., Rico-García, J. M., López-Alonso, J. M. & Boreman, G. (2005), 'Optical antennas for nano-photonic applications', *Nanotechnology* **16**, 230–+.

ALKOR Technologies (2009), 'UV and infrared optical materials for optical components.'. [Online; accessed 10-August-2009], `http://alkor.net/Materials.html`.

ANSYS Inc. (2007), 'Release 11.0 documentation for ansys'.

Berkley, D. A. & Wolga, G. J. (1962), 'Coherence studies of emission from a pulsed ruby laser', *Phys. Rev. Lett.* **9**(12), 479–482.

Black, J. (1969), 'Electromigration—A brief survey and some recent results', *Electron Devices, IEEE Transactions on Electron Devices* **16**, 338 – 347.

Capper, P. (1994), *Properties of Narrow Gap Cadmium-Based Compounds*, The Institution of Engineering and Technology, Southampton, UK.

Carminati, R. & Greffet, J.-J. (1999), 'Near-field effects in spatial coherence of thermal sources', *Phys. Rev. Lett.* **82**(8), 1660–1663.

Choi, S. R., Kim, D. & Choa, S.-H. (2006), 'Thermal Diffusivity of Metallic Thin Films: Au, Sn, Mo, and Al/Ti Alloy', *International Journal of Thermophysics* **27**, 1551–1563.

COMSOL AB (2007), 'Comsol material library'.

Cubukcu, E., Kort, E. A., Crozier, K. B. & Capasso, F. (2006), 'Plasmonic laser antenna', *Applied Physics Letters* **89**(9), 093120.

Cvitkovic, A., Ocelic, N., Aizpurua, J., Guckenberger, R. & Hillenbrand, R. (2006), 'Infrared imaging of single nanoparticles via strong field enhancement in a scanning nanogap', *Physical Review Letters* **97**(6), 060801.

Deemyad, S. & Silvera, I. F. (2008), 'Temperature dependence of the emissivity of platinum in the ir', *Review of Scientific Instruments* **79**(8), 086105.

Desai, C. S. & Kundu, T. (2001), *Introductory finite element method*, 1st edn, CRC Press, New York, USA.

Domingues, G., Volz, S., Joulain, K. & Greffet, J.-J. (2005), 'Heat transfer between two nanoparticles through near field interaction', *Phys. Rev. Lett.* **94**(8), 085901.

Efunda (2009), 'Efunda engineering fundamentals'. [Online; accessed 10-July-2009], `http://www.efunda.com/materials/elements/TC_Table.cfm?Element_ID=Si`.

Greffet, J.-J., Carminati, R., Joulain, K., Mulet, J.-P., Mainguy, S. & Chen, Y. (2002), 'Coherent emission of light by thermal sources', *Nature* **416**, 61–64.

Hamann, H. F., Gallagher, A. & Nesbitt, D. J. (2000), 'Near-field fluorescence imaging by localized field enhancement near a sharp probe tip', *Applied Physics Letters* **76**(14), 1953–1955.

Hecht, E. (1998), *Optics (3th Edition)*, 3rd edn, Addison Wesley, New York, USA.

Hendrik F. Hamann, Martin O' Boyle, Yves C. Martin, Michael Rooks & H. Kumar Wickramasinghe (2006*a*), 'Ultra-high-density phase-change storage and memory', *Nature Materials* **5**, 383–387.

Hendrik F. Hamann, Snorri Ingvarsson & James A. Lacey (2006*b*), 'Thermally excited near-field source'.

Ho, P. S. & Kwok, T. (1989), 'REVIEW ARTICLE: Electromigration in metals', *Reports on Progress in Physics* **52**, 301–348.

Holman, J. (1986), *Heat transfer*, 6th edn, McGraw-Hill Inc., New York, USA.

Ingvarsson, S., Klein, L. J., Au, Y.-Y., Lacey, J. A. & Hamann, H. F. (2007), 'Enhanced thermal emission from individual antenna-like nanoheaters', *Optics Express* **15**, 11249–+.

Jackson, J. D. (1998), *Classical Electrodynamics*, 3rd edn, Wiley, New York, USA.

Kato, R. & Hatta, I. (2005), 'Thermal Conductivity Measurement of Thermally-Oxidized SiO_2 Films on a Silicon Wafer Using a Thermo-Reflectance Technique', *International Journal of Thermophysics* **26**, 179–190.

Koji Matsumoto, Akihiro Inomata & Shin-ya Hasegawa (2006), 'Thermally Assisted Magnetic Recording', *Fujitsu Science and Technology Journal* **42**, 158–167.

Laroche, M., Arnold, C., Marquier, F., Carminati, R., Greffet, J.-J., Collin, S., Bardou, N. & Pelouard, J.-L. (2005), 'Highly directional radiation generated by a tungsten thermal source', *Opt. Lett.* **30**(19), 2623–2625.

Laroche, M., Carminati, R. & Greffet, J.-J. (2006), 'Near-field thermophotovoltaic energy conversion', *Journal of Applied Physics* **100**(6), 063704.

Levente J. Klein, Hendrik F. Hamann, Yat-Yin Au & Snorri Ingvarsson (2008), 'Coherence properties of infrared thermal emission from heated metallic nanowires', *Applied Physics Letters* **92**(21), 213102–+.

Liew, B.-K., Cheung, N. & Hu, C. (1990), 'Projecting interconnect electromigration lifetime for arbitrary current waveforms', *Electron Devices, IEEE Transactions on* **37**(5), 1343–1351.

Martin, Y. C., Hamann, H. F. & Wickramasinghe, H. K. (2001), 'Strength of the electric field in apertureless near-field optical microscopy', *Journal of Applied Physics* **89**(10), 5774–5778.

Newport (2009), 'Metals/non-metals - emissivity'. [Online; accessed 21-June-2009], http://www.newportus.com/Products/Techncal/MetlEmty.htm.

Petersen, K. E. (1978), 'Dynamic micromechanics on silicon: Techniques and devices', *IEEE transactions on electron devices* **25**(10), 1249.

Platinum metals review (2007), 'Specific heat v temperature graph for platinum'. [Online; accessed 10-July-2009], `http://www.platinummetalsreview.com/jmpgm/data/displayFunctionalGraph.do;jsessionid=0BD2E3FD638B0008742B62D3C2B8242D?attribute=168&database=cesdatabase&record=1219`.

Rybicki, G. B. & Lightman, A. P. (1979), *Radiative Processes in Astrophysics*, John Wiley & Sons, New York, USA.

Rytov, S., Kravtsov, Y. & Tatarski, V. (1987), *Principles of Statistical Radiophysics*, Springer, Berlin, Germany.

Sato, T. (1967), 'Emissivity of silicon as a function of temperature and wavelength', *Japanese Journal of Applied Physics* pp. 339–347.

Serway, R. A. (1998), *Principles of Physics*, 2nd edn, Saunders college publishing, London,UK.

Shackelford, J. & Alexander, W. (2001), *CRC Material science and engineering handbook*, 3rd edn, CRC Press, New York, USA.

Stavola, M. (1999), *Identification of Defects in Semiconductors*, Academic Press, San Diego, USA.

Strang, G. & Fix, G. J. (1973), *An Analysis of the Finite Element Method*, Prentice Hall.

Tao, J., Cheung, N. & Hu, C. (1993), 'Metal electromigration damage healing under bidirectional current stress', *Electron Device Letters, IEEE* **14**(12), 554–556.

Tao, J., Cheung, N. & Hu, C. (1995), 'Modeling electromigration lifetime under bidirectional current stress', *Electron Device Letters, IEEE* **16**(11), 476–478.

Thompson, J. & Younglove, B. (1961), 'Thermal conductivity of silicon at low temperatures', *Journal of Physics and Chemistry of Solids* **20**(1-2), 146 – 149.

Tsai, M.-W., Chuang, T.-H., Meng, C.-Y., Chang, Y.-T. & Lee, S.-C. (2006), 'High performance midinfrared narrow-band plasmonic thermal emitter', *Applied Physics Letters* **89**(17), 173116.

Wikipedia (2009*a*), 'Annealing (metallurgy) — wikipedia, the free encyclopedia'. [Online; accessed 23-June-2009], `http://en.wikipedia.org/w/index.php?title=Annealing_(metallurgy)&oldid=298195780`.

Wikipedia (2009*b*), 'Electromigration — wikipedia, the free encyclopedia'. [Online; accessed 2-May-2009], `http://en.wikipedia.org/w/index.php?title=Electromigration&oldid=287535797`.

Wikipedia (2009*c*), 'Electron beam lithography — wikipedia, the free encyclopedia'. [Online; accessed 2-June-2009], `http://en.wikipedia.org/w/index.php?title=Electron_beam_lithography&oldid=293905704`.

Wikipedia (2009*d*), 'Lambert's cosine law — wikipedia, the free encyclopedia'. [Online; accessed 9-January-2009], `http://en.wikipedia.org/w/index.php?title=Lambert%27s_cosine_law&oldid=263045468`.

Wikipedia (2009*e*), 'Photolithography — wikipedia, the free encyclopedia'. [Online; accessed 16-June-2009], `http://en.wikipedia.org/w/index.php?title=Photolithography&oldid=296747000`.

Wikipedia (2009*f*), 'Photoresist — wikipedia, the free encyclopedia'. [Online; accessed 17-June-2009], `http://en.wikipedia.org/w/index.php?title=Photoresist&oldid=297029729`.

Yamane, T., Mori, Y., ichiro Katayama, S. & Todoki, M. (1997), 'Measurement of thermal diffusivities of thin metallic films using the ac calorimetric method', *Journal of Applied Physics* **82**(3), 1153–1156.

Yat-Yin Au, Helgi Skuli Skulason, Snorri Ingvarsson, Levente J. Klein & Hendrik F. Hamann (2008), 'Thermal radiation spectra of individual subwavelength microheaters', *Physical Review B* **78**(8), 085402–+.

Young, H. & Freedman, R. A. (2007), *University Physics with Modern Physics*, 12th edn, Addison Wesley, New York, USA.

Zakirov, A. S., Igamberdiev, K. T., Mamadalimov, A. T., Musaeva, L. F. & Saidov, A. A. (2003), 'Transformation of the Defects of Gold in Silicon: Structural Phase Transition', *Journal of Engineering Physics and Thermophysics* **76**, 1084–1088.

Zhang, X., Xie, H., Fujii, M., Ago, H., Takahashi, K., Abe, H. & Shimizu, T. (2004), 'Measurements of In-Plane Thermal Conductivity and Electrical Conductivity of Susbended Platinum Thin Film', *Thermophys Prop* **25**, 249–251.

Zhang, X., Xie, H., Fujii, M., Ago, H., Takahashi, K., Ikuta, T., Abe, H. & Shimizu, T. (2005), 'Thermal and electrical conductivity of a suspended platinum nanofilm', *Applied Physics Letters* **86**(17), 171912.

Zienkiewicz, O. C., Taylor, R. & Zhu, J. (2005), *The finite element method: Its basis and fundamentals*, 6th edn, Elsevier, Oxford, UK.